

**UNDERSTANDING THE BIOLOGICAL ROLE OF
SIALIDASE NEU3 IN TAY-SACHS DISEASE
MOUSE MODEL**

**A Thesis Submitted to
the Graduate School of Engineering and Sciences of
İzmir Institute of Technology
in Partial Fulfillment of the Requirements for the Degree of**

DOCTOR OF PHILOSOPHY

in Molecular Biology and Genetics

**by
Seçil AKYILDIZ DEMİR**

**December 2019
İZMİR**

We approve the thesis of **Seçil AKYILDIZ DEMİR**

Examining Committee Members:

Prof. Dr. Bünyamin AKGÜL

Department of Molecular Biology and Genetics, izmir Institute of Technology

Assist. Prof. Dr. Şükrü GÜLEC

Department of Food Engineering, İzmir Institute of Technology

Prof. Dr. Michelle M. ADAMS

Department of Psychology, Bilkent University

Prof. Dr. Petek BALLAR KIRMIZIBAYRAK

Department of Basic Pharmaceutical Science, Ege University

Prof. Dr. Volkan SEYRANTEPE

Department of Molecular Biology and Genetics, İzmir Institute of Technology

20 December 2019

Prof. Dr. Volkan SEYRANTEPE

Supervisor, Department of Molecular Biology and Genetics
Izmir Institute of Technology

Prof. Dr. Bünyamin AKGÜL

Head of the Department of Molecular
Biology and Genetics

Prof. Dr. Mehtap EANES

Dean of the Graduate School of
Engineering and Science

ACKNOWLEDGMENTS

I would like to thank all the people who contributed in one way during my thesis. First of all, I would like to express my deepest regards and gratefulness to my supervisor Prof. Dr. Volkan SEYRANTEPE for his patience, understanding, motivation, enthusiasm. During my thesis, he directed me with intellectual freedom to search for new ideas in my work. His guidance helped me all the time in my research.

My special thanks are to the thesis monitoring and examining committee members Prof. Dr. Bünyamin AKGÜL and Assist. Prof. Dr. Şükrü GÜLEÇ, for their attention, recommendations and contributions during this period. I would like to thank Prof. Dr. Petek BALLAR KIRMIZIBAYRAK and Prof. Dr. Michelle M. ADAMS, the thesis examining committee members, for attention and recommendations.

I would like to thank Prof. Dr. Roger SANDHOFF for the mass spectrometry analysis of brain ganglioside, which was performed in the laboratory located German Cancer Research Center, Heidelberg, Germany. I am also thankful to Prof. Dr. Esra ERDEMLI for transmission electron microscopy analysis of mice brain, the experiment was performed in the laboratory found in Departments of Histology and Embryology, Ankara University, Ankara, Turkey. Finally, I would like to thank Prof. Dr. Emin ÖZTAS from Departments of Histology and Embryology, GATA Medical School, Ankara, Turkey for Transmission electron microscopy analysis of cerebellar and cerebral cortex neurons, testis, and kidney tissues.

Major parts of this study were supported by an EMBO 2010 Installation Grant to Prof Dr. Volkan SEYRANTEPE. I would like to thank also Marie Skłodowska-Curie Actions (FP7-PEOPLE-2010-RG) and The Scientific and Technological Research Council of Turkey (215Z083) for financial support of some part of the data.

I am grateful to my supportive friend, Zehra KEVSER TİMUR, Edanur ATEŞ, and Osman Yipkin ÇALHAN for their support and assistance at the beginning of the thesis project. I would like to thank Nurselin ATEŞ for their helping with the colony management and genotyping of the mice. I am also thankful to the other Seyrantepe Laboratory members for a friendly working environment and their sincere help and kindness.

I would like to thank my parents Nazlı AKYILDIZ and Sabahattin AKYILDIZ for their infinite believe and love to me, and supports in my decisions.

I would like to express my special thanks to my husband İsmail DEMİR for his endless love, motivation, encouragement and infinite support throughout my doctoral years and baby care.

I thank my daughter Ekin DEMİR for a baby smile, scent, infinite love, smile, curiosity, endless questions and a sleepless night.

ABSTRACT

UNDERSTANDING THE BIOLOGICAL ROLE OF SIALIDASE NEU3 IN TAY-SACHS DISEASE MOUSE MODEL

Tay-Sachs disease is a severe lysosomal storage disorder characterized by mutations in the lysosomal β -Hexosaminidase A (HEXA) enzyme which converts GM2 to GM3 ganglioside. The GM2 ganglioside accumulation is observed predominantly in the neurons. The infants appear normal in their inborn time, but the progressive accumulation of undegraded GM2 results with death. Hexa^{-/-} mice were created. However, they have a normal lifespan with no obvious neurological impairment until one year. It was thought that stored GM2 catabolized to GA2 using sialidase(s), which is further processed by HEXB. To determine the contribution of sialidase NEU3 to degradation of GM2, a mouse with combined deficiencies of Hexa and Neu3 genes was generated. The Hexa^{-/-}Neu3^{-/-} mice were healthy at birth, but they died between 1.5 and 5 months of age. Thin-layer chromatography and mass spectrometric analysis of the brains of Hexa^{-/-}Neu3^{-/-} mice revealed the abnormal accumulation of GM2. The progressive GM2 accumulation was also verified on testes, liver, and kidney of Hexa^{-/-}Neu3^{-/-} mice. GM2 accumulation in the brain leads to increased lysosomes with membranous cytoplasmic bodies, Purkinje cell depletion, cytoplasmic vacuolization, astrogliosis, and age-dependent lessening in neurons and oligodendrocytes. These mice have prominent disorders such as growth impairment, skeletal bones abnormalities, slow movement, tremors, anxiety and age-dependent loss in both memory and muscle strength. Consequently, the Hexa^{-/-}Neu3^{-/-} mice mimic the pathological, biochemical and clinical abnormalities of the Tay-Sachs patients, and useful model for the future understanding of cellular pathologies that drive the progression of the disease. They are a suitable model for the future pre-clinical testing of possible treatments

ÖZET

SİALİDAZ NEU3'ÜN TAY-SACHS HASTALIĞI FARE MODELİNDEKİ BİYOLOJİK ROLÜNÜN ANLAŞILMASI

Tay-Sachs hastalığı, GM2'yi GM3 gangliosidine dönüştüren lizozomal β -Heksosaminidaz A (HEXA) enzimindeki mutasyonlarla karakterize edilen şiddetli lizozomal depo hastalığıdır. GM2 gangliosit birikimi ağırlıklı olarak nöronlarda gözlenir. Hastalar doğduklarında normal görünür, ancak ilerlemeyen parçalanmamış GM2 birikimi ölümle sonuçlanır. Hexa-/- fareler oluşturuldu. Ancak, bu fareler bir yıla kadar gözle görünür bir nörolojik bozulma olmadan normal yaşam sürdürdüler. GM2'nin, sialidaz(lar) kullanılarak GA2'ye yıkıldığı HEXB tarafından daha fazla işlendiği düşünülmüştür. Sialidaz NEU3'ün GM2'nin bozulmasına katkısını belirlemek için, Hexa ve Neu3 genlerinin birleşik eksikliklerine sahip bir fare üretildi. Hexa-/-Neu3-/- fareleri doğumda sağlıklıydı, ancak 1.5 ile 5 ay arasında öldüler. İnce tabaka kromatografisi ve kütle spektrometrik analizi Hexa-/-Neu3-/- farelerinin beyinlerinde GM2'nin anormal birikimini ortaya koydu. Artan GM2 birikimi ayrıca Hexa-/-Neu3-/- farelerinin testis, karaciğer ve böbreklerinde de doğrulandı. Beyindeki GM2 birikimi, membranöz sitoplazmik cisimler içeren artan lizozom, Purkinje hücre bozulması, sitoplazmik vakuolizasyon, astrogliaz ve nöron ve oligodendrositlerde yaşa bağlı azalmaya yol açar. Bu fareler, hastalara benzer şekilde büyüme bozukluğu, iskelet kemiklerinde anormalliklere, harekette yavaşlama, titreme, anksiyete ve yaşa bağlı hem hafıza hem de kas gücünde kayıp gibi belirgin bozukluklara sahiptir. Bu sonuçlar göstermektedir ki, Hexa-/-Neu3-/- fareler, erken başlangıçlı Tay-Sachs hastalık fare modeli olarak kullanılabilir ve gelecekteki olası tedavilerin klinik öncesi testleri için uygun bir model sunar.

To My Endless Love and My Daughter

TABLE OF CONTENTS

LIST OF FIGURES	xi
LIST OF TABLES	xiv
CHAPTER 1. INTRODUCTION	1
1.1. Gangliosides	1
1.2. Lysosomal Storage Diseases	3
1.2.1. GM2 Gangliosidoses	4
1.2.2. Tay-Sachs Disease	5
1.2.3. Tay-Sachs Disease Mouse Model	7
1.3. Sialidases	8
1.3.1. Sialidases and Ganglioside Metabolism	9
1.4. Effect of Lysosomal Storage to Central Nervous System	11
1.4.1. Astrocytes	12
1.4.2. Neurons	14
1.4.3. Oligodendrocytes	15
1.5. The Mouse Brain	15
1.6. Behavioral Analysis	16
1.6.1. Rotarod Analysis	17
1.6.2. Footprint Analysis	17
1.6.3. Grip Strength Analysis	18
1.6.4. Passive Avoidance Analysis	18
1.6.5. Morris Water Maze Analysis	18
1.6.6. Open Field Analysis	19
1.7. Aim of the Study	19
CHAPTER 2. MATERIALS AND METHODS	20
2.1. Animals	20

2.2. Genotyping of Mice	21
2.2.1. Genomic DNA Isolation	22
2.2.2. PCR Reaction	22
2.3. Body Weight Measurement	23
2.4. Gross Appearance and X-Ray Analysis of Mice	23
2.5. Thin-Layer Chromatography Analysis	24
2.5.1. Lipid Isolation	24
2.5.2. Thin-Layer Chromatography	25
2.5.3. DEAE Sephadex A25 Ion Exchange Column Preparation	26
2.5.4. Staining with Orcinol and Visualization	26
2.6. Mass Spectrometer Analysis	27
2.7. Anti GM2/Lamp1 Staining	27
2.8. Transmission Electron Microscopy	28
2.9. May-Grunwald Giemsa Staining	29
2.10. Enzyme Activity Assay	29
2.11. Effects of GM2 Accumulation to CNS	33
2.11.1. Sample Preparation	33
2.11.2. Hematoxylin–Eosin Staining	33
2.11.3. TUNEL Staining	34
2.11.4. Anti-NeuN Staining	34
2.11.5. Anti-GFAP Staining	35
2.11.6. Anti-CNPase Staining	35
2.12. Behavioral Analysis	36
2.12.1. Rotarod Test	36
2.12.2. Footprint Test	36
2.12.3. Grip Strength Measurement Test	37
2.12.4. Passive Avoidance Test	37
2.12.5. Morris Water Maze Test	38
2.12.6. Open Field Test	38
2.13. Statistical Analysis	39
CHAPTER 3. RESULTS	40
3.1. Genotyping of Knockout Mice	40

3.2. Body Weight Measurement	41
3.3. Thin-Layer Chromatography Analysis	43
3.4. Mass Spectrometer Analysis	49
3.5. GM2 and Lysosome Staining	51
3.6. Transmission Electron Microscopy	57
3.7. May-Grunwald Giemsa Staining	60
3.8. Enzyme Activity Assay	61
3.9. Effects of GM2 Accumulation to CNS	63
3.9.1. Hematoxylin and Eosin Staining	63
3.9.2. Neuronal Death	65
3.9.3. Astrocyte Analysis	70
3.9.4. Oligodendrocyte Analysis	70
3.10. Behavioral Analysis	75
3.10.1. Rotarod Test	75
3.10.2. Footprint Test	75
3.10.3. Grip Strength Test	77
3.10.4. Passive Avoidance Test	78
3.10.5. Morris Water Maze Test	80
3.10.6. Open Field Test	82
 CHAPTER 4. DISCUSSION	 84
 CHAPTER 5. CONCLUSION	 89
 REFERENCES	 92

LIST OF FIGURES

<u>Figure</u>	<u>Page</u>
Figure 1.1. Lysosomal ganglioside degradation pathway for as 0-, a-, b-, and c-series gangliosides	2
Figure 1.2. Hex isozymes with their associated substrates for GM2 gangliosidosis diseases	5
Figure 1.3. Tay-Sachs disease pathology.....	6
Figure 1.4. Alternative pathways for the catabolism of GM2 in Tay-Sachs patients and Hexa ^{-/-} mice	8
Figure 1.5. The neuroinflammatory process	13
Figure 3.1. Gel images of Hexa and Neu3 PCR products	40
Figure 3.2. Weight measurements, gross appearance and X-ray images of WT, Hexa ^{-/-} , Neu3 ^{-/-} and Hexa ^{-/-} Neu3 ^{-/-} mice	42
Figure 3.3. Survival graph of Hexa ^{-/-} and Hexa ^{-/-} Neu3 ^{-/-} mice	43
Figure 3.4. TLC images of orcinol-stained acidic and neutral glycosphingolipids from the brain of 2.5-and 4.5-month-old WT, Hexa ^{-/-} , Neu3 ^{-/-} and Hexa ^{-/-} Neu3 ^{-/-} mice	45
Figure 3.5. TLC images of orcinol-stained acidic and neutral glycosphingolipids from testes of 2.5-and 4.5-month-old WT, Hexa ^{-/-} , Neu3 ^{-/-} and Hexa ^{-/-} Neu3 ^{-/-} mice	46
Figure 3.6. TLC images of orcinol-stained acidic and neutral glycosphingolipids from the liver of the 2.5-and 4.5-month-old WT, Hexa ^{-/-} , Neu3 ^{-/-} and Hexa ^{-/-} Neu3 ^{-/-} mice	47
Figure 3.7. TLC images of orcinol-stained acidic and neutral glycosphingolipids from the kidney of 2.5-and 4.5-month-old WT, Hexa ^{-/-} , Neu3 ^{-/-} and Hexa ^{-/-} Neu3 ^{-/-} mice	48
Figure 3.8. Mass spectrometric analysis of GM2, GA2, LacCer, GM3, GM2, GM1, and GA1 in the brain of 4.5-month-old WT, Hexa ^{-/-} , Neu3 ^{-/-} and Hexa ^{-/-} Neu3 ^{-/-} mice	50

Figure 3.9. Immunohistochemistry to detect the lysosomal storage of GM2 ganglioside in the hippocampus of 4.5-month-old WT, Hexa ^{-/-} , Neu3 ^{-/-} and Hexa ^{-/-} Neu3 ^{-/-} mice	52
Figure 3.10. Immunohistochemistry to detect the lysosomal storage of GM2 ganglioside in the cortex of 4.5-month-old WT, Hexa ^{-/-} , Neu3 ^{-/-} and Hexa ^{-/-} Neu3 ^{-/-} mice	53
Figure 3.11. Immunohistochemistry to detect the lysosomal storage of GM2 ganglioside in the thalamus of 4.5-month-old WT, Hexa ^{-/-} , Neu3 ^{-/-} and Hexa ^{-/-} Neu3 ^{-/-} mice	54
Figure 3.12. Immunohistochemistry to detect the lysosomal storage of GM2 ganglioside in the cerebellum of 4.5-month-old WT, Hexa ^{-/-} , Neu3 ^{-/-} and Hexa ^{-/-} Neu3 ^{-/-} mice	55
Figure 3.13. Immunohistochemistry to detect the lysosomal storage of GM2 ganglioside in the pons of 4.5-month-old WT, Hexa ^{-/-} , Neu3 ^{-/-} and Hexa ^{-/-} Neu3 ^{-/-} mice	56
Figure 3.14. Transmission electron micrograph of membranous cytoplasmic bodies in the cortex of WT, Hexa ^{-/-} , Neu3 ^{-/-} and Hexa ^{-/-} Neu3 ^{-/-} mice	58
Figure 3.15. Transmission electron micrographs of lysosomal inclusions in cerebellar and cerebral cortex neurons, testis, and kidney tissues from 4.5-month-old Hexa ^{-/-} Neu3 ^{-/-} mice	59
Figure 3.16. Blood smear analysis of 4.5-month-old mice to detect lysosomal accumulation on monocytes	60
Figure 3.17. The levels of β -Galactosidase, β -Glucosidase, β -Hexosaminidase B, Neuraminidase 1 and Iduronidase in the brain of 2.5 and 4.5-month-old WT, Hexa ^{-/-} , Neu3 ^{-/-} and Hexa ^{-/-} Neu3 ^{-/-} mice	62
Figure 3.18. Neuropathology in the cortex of 4.5-month-old Hexa ^{-/-} Neu3 ^{-/-} mice compared with WT, Hexa ^{-/-} and Neu3 ^{-/-} mice with Hematoxylin–Eosin staining	64
Figure 3.19. Neuropathology in the cerebellum of 4.5-month-old Hexa ^{-/-} Neu3 ^{-/-} mice compared with WT, Hexa ^{-/-} and Neu3 ^{-/-} mice with Hematoxylin–Eosin staining	65
Figure 3.20. The TUNEL assay for 4.5-month-old mice	67

Figure 3.21. The neuron number of 2.5-month-old mice	68
Figure 3.22. The neuron number of 4.5-month-old mice	69
Figure 3.23. Detection of astrocytes in 2.5-month-old mice	71
Figure 3.24. Detection of astrocytes in 4.5-month-old mice	72
Figure 3.25. Detection of oligodendrocytes number in 2.5-month-old mice	73
Figure 3.26. Detection of oligodendrocytes number in 4.5-month-old mice	74
Figure 3.27. Rotarod test of 2.5-, 3.5- and 4.5-month-old mice	76
Figure 3.28. Footprints analysis of 4.5-month-old mice	77
Figure 3.29. Forelimb grip strength of 2.5- and 4.5-month-old mice	78
Figure 3.30. Passive avoidance test of 2.5- and 4.5-month-old mice	79
Figure 3.31. Morris water maze of 2.5- and 4.5-month-old mice	81
Figure 3.32. Open field test of 2.5- and 4.5-month-old mice	83

LIST OF TABLES

<u>Table</u>	<u>Page</u>
Table 2.1. The crossing of Hexa ^{-/-} and Neu3 ^{-/-} mice	21
Table 2.2. Sequences of used primers in genotyping	23
Table 2.3. The isolated and sprayed amount of neutral and acidic glycosphingolipid for TLC analysis of brain, liver, kidney, testis	25
Table 2.4. Substrates used for enzyme activity assay	30
Table 2.5. Sialidase enzyme activity assays	31
Table 2.6. β -Galactosidase enzyme activity assays	31
Table 2.7. β -Glucosidase enzyme activity assays	31
Table 2.8. α -L-Iduronidase enzyme activity assays	32
Table 2.9. β -Hexosaminidase enzyme activity assay	32
Table 5.1. Clinical symptoms in Tay-Sachs patients, Hexa ^{-/-} mouse Hexa ^{-/-} Neu3 ^{-/-} mouse	90

CHAPTER 1

INTRODUCTION

1.1. Gangliosides

Ceramide forms the backbone of more complex sphingolipids. Attachment of saccharides to the hydroxyl group of ceramide produces glycosphingolipids (GSLs) in the Golgi apparatus. Ceramide and glycosphingolipids content in brain changes throughout life, during aging, and neurodegenerative diseases. Mammals are rich in glycosphingolipids in their nervous system. Gangliosides are sialic acid-containing glycosphingolipids. They are major components of neural membranes which are up to 10–12% of the total lipid content (Posse de Chaves and Sipione 2010).

Gangliosides are located at the outer surface of most cell membranes. Their function in neuritic growth, cell recognition, and neural transmission were detected. They are catabolized in the lysosome. Glycohydrolases are responsible for the degradation of them by sequential removal of terminal sugars to a ceramide core. Deficiency in the hydrolytic enzymes causes lysosomal storage diseases by the accumulation of glycolipid intermediates in the lysosome (Phaneuf et al. 1996).

Ceramide is formed in the endoplasmic reticulum (ER). It is glycosylated at the Golgi and trans-Golgi network (TGN). Glucosylceramide (GlcCer) is formed at the cytosolic surface of Golgi membranes. GlcCer flips to the luminal surface of Golgi membranes where it is converted to lactosylceramide (LacCer). LacCer is sialylated to form small precursor gangliosides (GM3, GD3, and GT3). Then, they are converted to complex ganglioside structures by membrane-bound glycosyltransferases. The vesicular transport of the secretory pathway helps the complex gangliosides to transport cellular surfaces (Sandhoff and Harzer 2013). There are different ganglioside series such as 0-, a-, b-, and c-series. The 0-series gangliosides carry no sialic acids, the a-series gangliosides

carry one, the b-series gangliosides carry two, and the c-series gangliosides carry three sialic acid residues on the galactose in position II (Figure 1.1) (Kolter 2012).

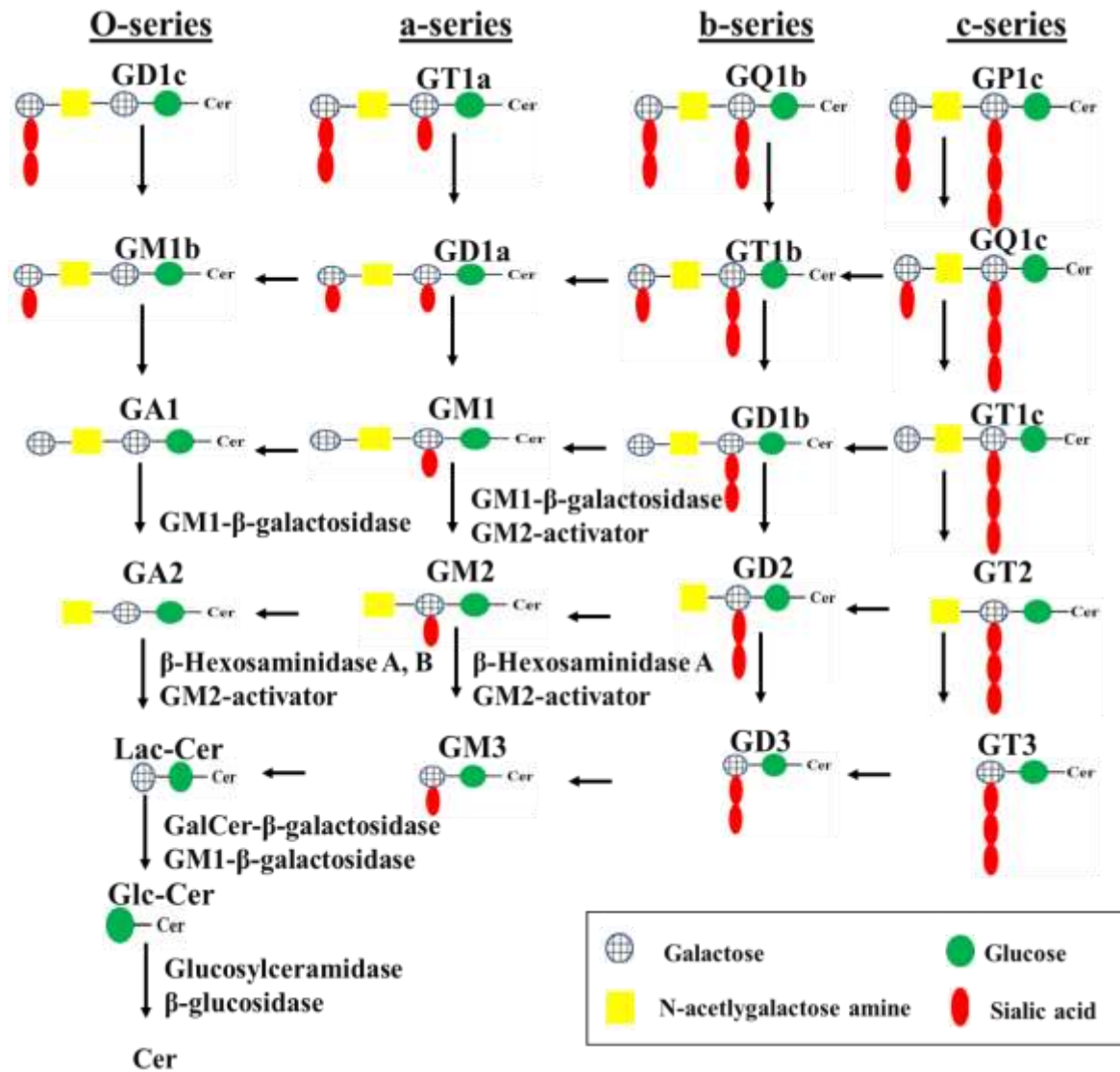


Figure 1.1. Lysosomal ganglioside degradation pathway for as 0-, a-, b-, and c-series gangliosides

The degradation of gangliosides takes place in endosomes and lysosomes. After the endocytosis of the plasma membrane, lysosomal ganglioside degradation takes place at intra-endosomal and intra-lysosomal membranes. Glycosidases (GSL

hydrolases) are soluble enzymes in the lumen of endosomes and lysosomes. Ganglioside degradation begins when glycosidases cleave off monosaccharide units from the non-reducing end of the ganglioside glycan chains. This removal happens sequentially. When the cleavage sites are close to the intra-lysosomal membrane surface, the activity of glycosidases is not sufficient. In addition to glycosidases, activator proteins and appropriate membrane-lipid composition of the ganglioside-containing membrane are required for degradation. For example, saposins (A-B-C-D), small, water-soluble lysosomal lipid-binding and -transfer proteins, helps the degradation of GSLs (Kolter 2012). The detailed ganglioside degradation pathway is shown in Figure 1. Individual defects in glycosidase cause excessive accumulation of specific GSLs in lysosomes leading to the different lysosomal storage diseases (LSDs) (Xu et al. 2010).

1.2. Lysosomal Storage Diseases

Lysosomes, membrane-enclosed cytoplasmic organelles, include different kinds of active hydrolytic enzymes such as glycosidases, sulfatases, phosphatases, lipases, phospholipases, proteases, and nucleases in an acidic pH. Genetic deficiency in the activity of the lysosomal enzyme leads to the accumulation of undegraded material. This is known as lysosomal storage diseases (LSDs) (Ferreira and Gahl 2017).

The storage material is glycogen in the Pompe disease, glycosaminoglycans in the mucopolysaccharidoses, glycoproteins in the oligosaccharides, and sphingolipids in the Tay-Sachs disease, Sandhoff disease, GM1 gangliosidosis, Niemann-Pick disease types A and B, Gaucher disease, Fabry disease, and Krabbe disease. The deficiency of an activator protein also leads to lysosomal storage as in the AB variant of GM2 gangliosidosis (Sun 2018).

1.2.1. GM2 Gangliosidoses

The GM2 gangliosidoses are a group of lysosomal storage disorders resulted from are resulted from impaired degradation of GM2 ganglioside and related substances by the mutations in any of three different genes: HEXA, HEXB, and GM2AP. Mutation in the HEXA, HEXB, and GM2AP genes resulted in Tay-Sachs diseases, Sandhoff diseases, and GM2AP variants, respectively (Yamanaka et al. 1994; Sango et al. 1995). The HEXA encodes the α -subunit and HEXB encodes the β -subunits of the β -hexosaminidase A (HEXA) enzyme. This enzyme forms a Michaelis–Menten complex with GM2AP to hydrolyze GM2 and GA2 ganglioside by removing N-acetylgalactosamine (Sandhoff and Harzer 2013; Lawson and Martin 2016). β -Hexosaminidase B (HEXB) includes a homodimer of two β subunits. There is also a minor form of the enzyme (Hexosaminidase S) which has two α subunits (Yamanaka et al. 1994; Sango et al. 1995).

Tay–Sachs disease patients have a loss of HEXA (α,β) and S (α,α) activities. Alternatively, Sandhoff disease patients have the loss of HEXA (α,β) and HEXB (β,β) activities (Sandhoff and Harzer 2013; Lawson and Martin 2016). Tay-Sachs disease, Sandhoff disease, and GM2A deficiency are clinically similar (Solovyeva et al. 2018).

The GM2 gangliosidoses disease types and their related genes, proteins, isoenzyme subunits, and accumulated substrates are described in Figure 1.2.

GM2 ganglioside is one of the glycosphingolipids which is located as an intermediate compound in biosynthesis and degradation of complex brain ganglioside (mainly GM1a, GD1a, GD1b, and GT1b) (Sandhoff and Kolter 1998) Complex brain gangliosides are most abundant in the cell membranes of neurons. They have a role in brain development and function by affecting neurotransmission, neurogenesis, synaptogenesis, modulating synaptic transmission, cell proliferation, and neuronal differentiation. Selective knock-out of ganglioside synthase and degradation genes lead to a range of structural and functional defects such as altered neural development, neuronal degeneration, loss of sensory and motor functions, demyelination, axonal deterioration, behavioral abnormalities and learning and memory loss (Palmano et al. 2015). Therefore, the central nervous system is the most affected tissue in GM2 gangliosidosis patients (Sandhoff 2016).

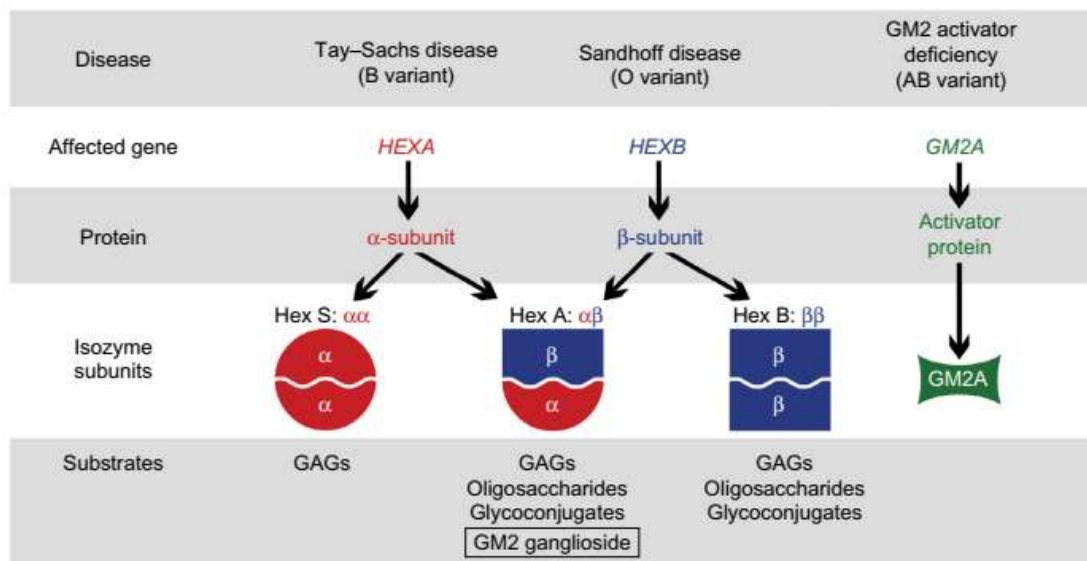


Figure 1.2. Hex isozymes with their associated substrates for GM2 gangliosidosis diseases (Source: Lawson and Martin 2016)

1.2.2. Tay-Sachs Disease

Tay-Sachs disease, a fatal neurodegenerative disorder, is inherited in an autosomal recessive mode of inheritance. (Yamanaka et al. 1994). It is resulted by mutations in the *HEXA* gene causing the absence of the lysosomal enzyme β -Hexosaminidase A. The disease frequency is one in 100,000 live births. Tay-Sachs disease, Sandhoff disease, and GM2A deficiency are clinically similar. More than 130 different mutations in the *HEXA* gene are described. These mutations are partial deletion, splicing mutations, nonsense mutations, missense mutations. Mutations disrupt transcription, translation, folding, dimerization of monomers and catalytic dysfunction of *HEXA* protein (Figure 1.3) (Solovyeva et al. 2018).

In the absence of β -Hexosaminidase A, GM2 ganglioside accumulates in neurons at the beginning of fetal life. GM2 ganglioside is stored in membranous cytoplasmic bodies (MCBs), appear as concentric ring-like structures. At the terminal stage of Tay-Sachs disease, patients have balloon-shaped MCBs filling their cytoplasm in most

neurons. This lead to distortion in the cellular architecture (Yamanaka et al. 1994). 10–15% of HEXA activity is enough to prevent the accumulation of GM2 ganglioside (Solovyeva et al. 2018).

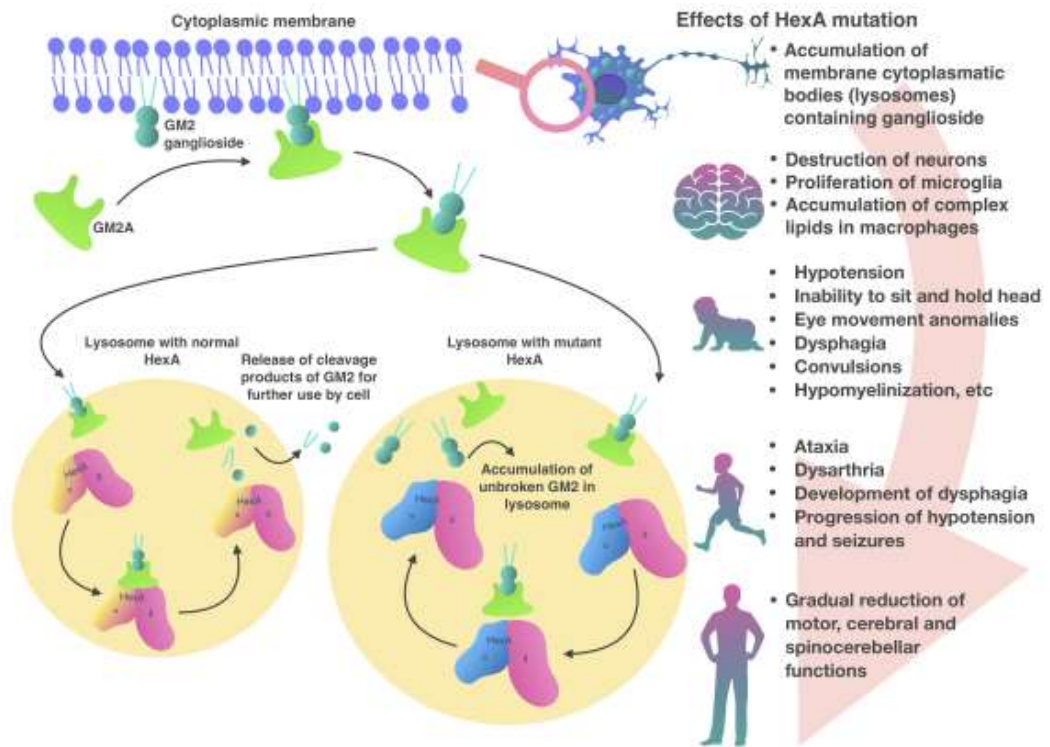


Figure 1.3. Tay-Sachs disease pathology (Source: Solovyeva et al. 2018)

There are three forms of Tay-Sachs disease; infantile, juvenile and later-onset form. The infantile form is the most severe one with mental and motor developmental delay. It is observed by onset around 6 months of age with very low HEXA activity levels (<0.5%). Infants are unable to sit or hold their head without the support and has eye movement abnormalities, dysphagia, spasms, hypomyelination. Finally, it results in death a maximum of 4 years of age. In the juvenile form, the symptoms appear at the age of 3-10 years as ataxia, dysarthria, dysphagia development, hypotension, and spasm progression. Most of the patients are dead maximum the 15 years of age. Late-onset form is the rarest one which is observed in adulthood or 20–30 years old. It is characterized by small mutations and higher residual HEXA activity as 5–20%. All in all, Tay-Sachs

patients have muscle weakness, ataxia, speech, and mental disorders (Solovyeva et al. 2018).

1.2.3. Tay-Sachs Disease Mouse Model

Hexa^{-/-} mouse was created by three different research groups. All of these mice had a complete absence in the activity of β -Hexosaminidase A. (Yamanaka et al. 1994; Cohen-Tannoudji et al. 1995; Phaneuf et al. 1996). However, unlike Tay-Sachs disease patients, there was limited ganglioside storage in certain regions of the nervous system in the Hexa^{-/-} mice. No neuronal storage was detected in the cerebellum, the anterior horn of the spinal cord, or the spinal ganglia. Only minor storage was observed in the posterior horn of the spinal cord. It was thought that there can be differences in the metabolic pathway of GM2 ganglioside in humans and mice (Yamanaka et al. 1994). Electron microscopic examinations of the ballooned neurons showed membranous cytoplasmic bodies in an age-dependent manner. It was thought that in contrast to the human, murine HEXB is functional to hydrolyze GM2-ganglioside (Cohen-Tannoudji et al. 1995).

Two different GM2 gangliosidosis mouse models; Hexa^{-/-} mice lacking HEXA activity and Hexb^{-/-} mice lacking both HEXA and HEXB activity were analyzed at the same time. Unlike the human disease situation, Hexa^{-/-} mice have no behavioral phenotype, while Hexb^{-/-} mice express a rapidly progressive, fatal neurodegenerative disease (Phaneuf et al. 1996).

Two different alternative pathways were hypothesized for the catabolism of GM2 in Hexa^{-/-} mice (Figure 1.4). Model 1 was the hydrolysis of N-acetylgalactose amine from GM2 by functional HEXB to yield GM3. Model 2 was for the hydrolysis of sialic acid from GM2 by sialidase to yield GA2, which is followed by hydrolysis of the N-acetylgalactose amine by HEXB to yield LacCer (Phaneuf et al. 1996).

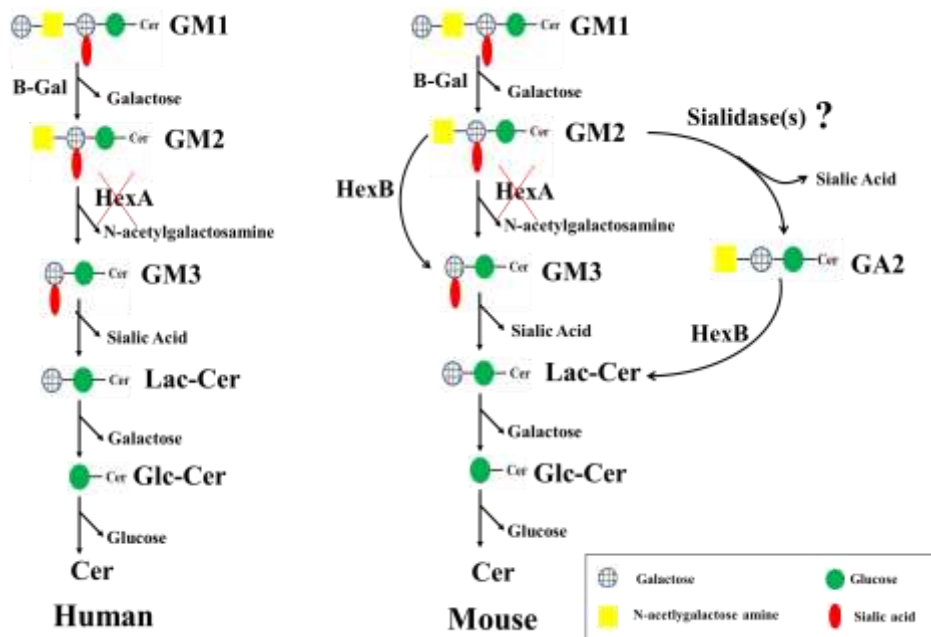


Figure 1.4. Alternative pathways for the catabolism of GM2 in Tay-Sachs patients and Hexa^{-/-} mice (Adapted from: Phaneuf et al. 1996)

1.3. Sialidases

Sialidases (Neuraminidases), belongs to a family of exoglycosidases, are responsible for catalyzation of hydrolytic cleavage of nonreducing sialic acid residues from glycoconjugates such as glycoproteins and glycolipids (Monti et al. 2002; Fanzani et al. 2004). These enzymes cleave terminal $\alpha 2 \rightarrow 3$, $\alpha 2 \rightarrow 6$ and $\alpha 2 \rightarrow 8$ sialyl linkages (Fanzani et al. 2004). They are widely distributed in nature from viruses and microorganisms to avian and mammalian species (Monti et al. 2002).

In mammals, four different sialidases have been purified, cloned and characterized so far. They all classified based on their subcellular localization; lysosomal sialidase (NEU1), cytoplasmic sialidase (NEU2), membrane-bound sialidase (NEU3), lysosomal/-mitochondrial/-intracellular membranes sialidase (NEU4). Their expression level in different cell and tissue, substrate specificities and optimum pH levels are also different. Optimum pH level for NEU1, NEU2, NEU3, and NEU4 is 4.4-4.6, 6.0-6.5, 4.6-4.8 and

3.2-4.8, respectively. These enzymes have involved in different cellular events such as gangliosides and glycoproteins metabolism, cell proliferation, differentiation, clearance of plasma proteins, cell adhesion control, receptor modification, immunocyte function, and modeling of myelin (Monti et al. 2010). The involvement of sialidase in these biological networks could be either direct or secondary to the desialylation of the various substrate(s) (Monti et al. 2002).

1.3.1. Sialidases and Ganglioside Metabolism

Sialidase enzyme removes sialic acid from GM2 ganglioside and converts to GA2 which is further degraded to LacCer by HEXB in the mouse neurons (Phaneuf et al. 1996). Later, it was found that Neuraminidase 4 (NEU4) may function on the ganglioside metabolism in Hexa^{-/-} mice (Seyrantepe et al. 2008). Cloning of NEU4 showed that NEU4 is active against all types of sialylated glycoconjugates such as oligosaccharides, glycoproteins, and gangliosides (Seyrantepe et al. 2004). It was shown that the Neu4^{-/-} mouse model had lysosomal storage bodies in macrophages of the lung, macrophages, and lymphocytes of the spleen. Moreover, there are increased levels of gangliosides, ceramide, cholesterol and fatty acids in the brain, liver, lungs, and spleen of Neu4^{-/-} mice. When neuroglia cells of a Tay-Sachs patient were transfected with a Neu4 expressing plasmid, it was restored normal morphological phenotype of the cells and corrected the impaired metabolism of GM2 ganglioside by glycolipid GA2. NEU4 is active in the desialylation of GM2 ganglioside in the presence of detergents or lysosomal activator proteins (Seyrantepe et al. 2008).

Double deficient mouse model of Neu4 and Hexa was generated by Seyrantepe et al. in 2010. Neu4^{-/-}Hexa^{-/-} mice had severe disease phenotype compared to Neu4^{-/-} mice and Hexa^{-/-} mice. Neu4^{-/-}Hexa^{-/-} mice were healthy at birth but 40% of them developed seizure-like epileptic events after 3 months of age. Neu4^{-/-} mice and Hexa^{-/-} mice had no seizures until at least one year of age. Immunochemical analysis of Neu4^{-/-}Hexa^{-/-} mice brain tissues using anti-GM2 antibodies showed that there was accumulation in GM2 mostly in the ventral cortex and hippocampus of the adult brain. Double-knockout mice with epileptic seizures had an increased number of GM2-positive cells. Moreover, the

affected neurons were analyzed with electron microscopy and observed that there were large irregular lysosomes with characteristic membranous whorls similar to the histopathological findings in human Tay-Sachs patients (Seyrantepe, Lema, et al. 2010).

It was understood that NEU4 was not the only sialidase contributing to the bypass of the HEXA defect in Hexa^{-/-} mice because it was not matching the severe disease phenotype of Hexb^{-/-} mice (Seyrantepe, Lema, et al. 2010). Hexb^{-/-} mice lack not only HEXA enzyme and HEXB enzyme so both arms of the GM2 degradation pathway are blocked. In these mice tremors, muscle weakness, stiffening of the hind limbs and an ataxic gait were observed at the 2-3 months of age. The disease rapidly progresses tremor, myoclonus, and death by six weeks after onset (Sango et al. 1995; Phaneuf et al. 1996). In adult Neu4^{-/-}Hexa^{-/-} mice milder disease phenotype observed. This should result from the contribution of the other sialidases the bypass (Seyrantepe, Lema, et al. 2010).

NEU1 interacts with protective protein/cathepsin A (PPCA) and β -galactosidase and forms a lysosomal multienzyme complex. It was showed that NEU1 mostly active toward sialyloligosaccharides and sialylglycoproteins but it can also hydrolyze some ganglioside such as GM3 and GD1a and has weak activity toward GM2. Analyzing of skin fibroblast from sialidosis and galactosialidosis showed that GM3 ganglioside metabolism was impaired. What is more, visceral tissues of sialidosis patients have GM3 and GD3 ganglioside storage (Seyrantepe, Lema, et al. 2010).

NEU3, the plasma-membrane-associated form of sialidases, shows high substrate specificity towards gangliosides. It modulates cell-surface biological events and has a role in different cellular processes such as cell adhesion, recognition, and differentiation. It localized at the outer leaflet plasma membrane and inner leaflet of the endosomal compartment. In this way, NEU3 can degrade gangliosides inserted into the plasma membrane of adjacent cells (Zanchetti et al. 2007). It is expressed mostly in the heart but also in the brain, spleen, lung, kidney, and testis. In situ hybridization analysis of the brain showed that it is present in the cerebral cortex and the granule cell layer, Purkinje cells, and deep cerebellar nucleus of the cerebellum (Hasegawa et al. 2000).

Interestingly, it was found that the mouse NEU3, but not NEU2, can hydrolyze the sialic acid from GM1 and GM2 in the presence of GM2 activator protein. These results provide evidence for the conversion of GM2 into GA2 by NEU3 and support the presence of the GA2 pathway for the catabolism of GM2 in the mouse. The interaction of GM1 and GM2 with GM2AP might induce the conformational change and so N-

acetylgalactose amine and sialic acid residues can be hydrolyzed by HEXA and sialidase, respectively (Li et al. 2001)

The administration of the radiolabeled GD1a ganglioside to murine Neu3-transfected cells causes a significant decrease of GD1a and GM3 and an increase of GM1 in comparison with mock-transfected cells. The modification of the ganglioside pattern was reversible and strictly dependent on transient NEU3 expression. These results were important to show NEU3 can hydrolyze ganglioside substrates in intact living cells at a neutral pH, with the involvement of cell-to-cell interactions (Papini et al. 2004)

Human fibroblast was administered with radioactive GM3. Radioactive LacCer, Cer, and SM production were observed. Radioactive SM can be formed only when GM3 reaches lysosomes. To be sure that which part of the catabolic process occurred also at the cell surface, lysosomal activity and endocytosis of the cell were blocked. Radioactive lactosylceramide and SM was not observed, while ceramide was produced. This proved that GM3 disappears and turns to LacCer, GlcCer, and Cer, respectively. Overexpression of NEU3 resulted in a higher production of ceramide in the plasma membrane (Valaperta et al. 2006).

NEU3 has a role in many biological processes such as neuronal differentiation, T-cell activation, monocyte differentiation, cell adhesion, and motility. Besides, it is upregulated in many human cancers, including colon, renal, prostate, and ovarian cancers. To analyze the role of NEU3 in tumor development, Neu3 deficient mice were generated. Their susceptibility to tumorigenesis in carcinogen-induced models of sporadic and colitis-associated colon cancer was analyzed and it was determined that Neu3 deficiency lowered the incidence of colitis-associated colon carcinogenesis (Yamaguchi et al. 2012).

1.4. Effect of Lysosomal Storage to Central Nervous System

Lysosomal storage disorders, affect the central nervous system, cause activation of neuroinflammatory responses. The central nervous system consists of main neurons, microglial cells, and macroglial cells. Macroglial cells are astrocytes and oligodendrocytes (Rasband 2016). Under normal conditions, microglial cells stay in the inactive stage but the accumulated macromolecules activate microglial cells causing an

increased inflammatory response via the production of inflammatory cytokines and chemokines. This is known as microgliosis (Vitner et al. 2010). Cytokines are small secreted proteins that have a specific effect on the interactions and communications between cells (Zhang and An 2007). Chemokines are a superfamily of secreted small molecules involved in immunoregulatory and inflammatory processes. Increased levels of chemokines and their respective receptors have been found in numerous pathological conditions (Reichel et al. 2009). Alterations in the gene expression of inflammatory cytokine and chemokine gene expressions were shown directly related to neuroinflammation in lysosomal storage disorders (Bosch and Kielian 2015).

Microgliosis cause increased inflammatory response which has a major contribution to disease pathology (Vitner et al. 2010). They work to recruit and activate peripheral immune cells at affected sites. It can act to activate neighboring microglia, astrocytes, neurons, or oligodendrocytes (Bosch and Kielian 2015).

1.4.1. Astrocytes

Astrocytes, are the most abundant cell type in the CNS, have a function in cellular support during CNS development, ion homeostasis, uptake of neurotransmitters, contribution to the CNS immune system and neuromodulation. Another role is the preservation of the host tissue integrity following injury. Injury cause activation of astrocytes, called astrogliosis (Figure 1.5) (Ridet et al. 1997).

They contribute to neuroinflammation by their secretion of various chemokines. Once activation, astrocytes undergo a morphological change as increase intermediate filament expression (i.e., glial fibrillary acidic protein (GFAP) and vimentin) and reactive astrocytes have been involved in the pathogenesis of various neurodegenerative diseases (Bosch and Kielian 2015).

Studies revealed that ganglioside accumulation causes neuroinflammation in several lysosomal storage disorders. It was demonstrated that the storage of GM1 and GM2 ganglioside in the CNS led to inflammation characterized as microgliosis and astrogliosis which are correlated with the amount of stored ganglioside. Inflammation and inflammatory cytokines (TNF α , IL1 β , and TGF β 1) were absent in Tay-Sachs mice

(Hexa^{-/-}) but were most widespread in Sandhoff (Hexb^{-/-}), GM1 gangliosidosis mice (Jeyakumar et al. 2003) and GM2-gangliosidosis patients (Wada et al. 2000). Activation of microglia and astrocytes resulted in inflammatory mediators production (Myerowitz et al. 2002). Significantly increased levels of TNF- α pro-inflammatory cytokine was showed in the TSD patient cerebrospinal fluid (Hayase et al. 2010). Five inflammation biomarkers, ENA-78, MCP-1, MIP-1 α , MIP-1 β , TNFR2 were also distinguished in the cerebrospinal fluid of patients with infantile and juvenile gangliosidosis (Utz et al. 2015). Different lysosomal storage disorders including Niemann–Pick type C disease (Baudry et al. 2003), Gaucher disease (Farfel-Becker et al. 2011), mucopolysaccharidosis type I, IIIA and III (Wilkinson et al. 2012) and neuronal ceroid lipofuscinoses (Kollmann et al. 2013) also display prominent microglial and astrocyte activation. At times of inflammation, up-regulation of cytokines and their receptors within the CNS was observed, with concomitant effects on brain function (Jeyakumar et al. 2003)

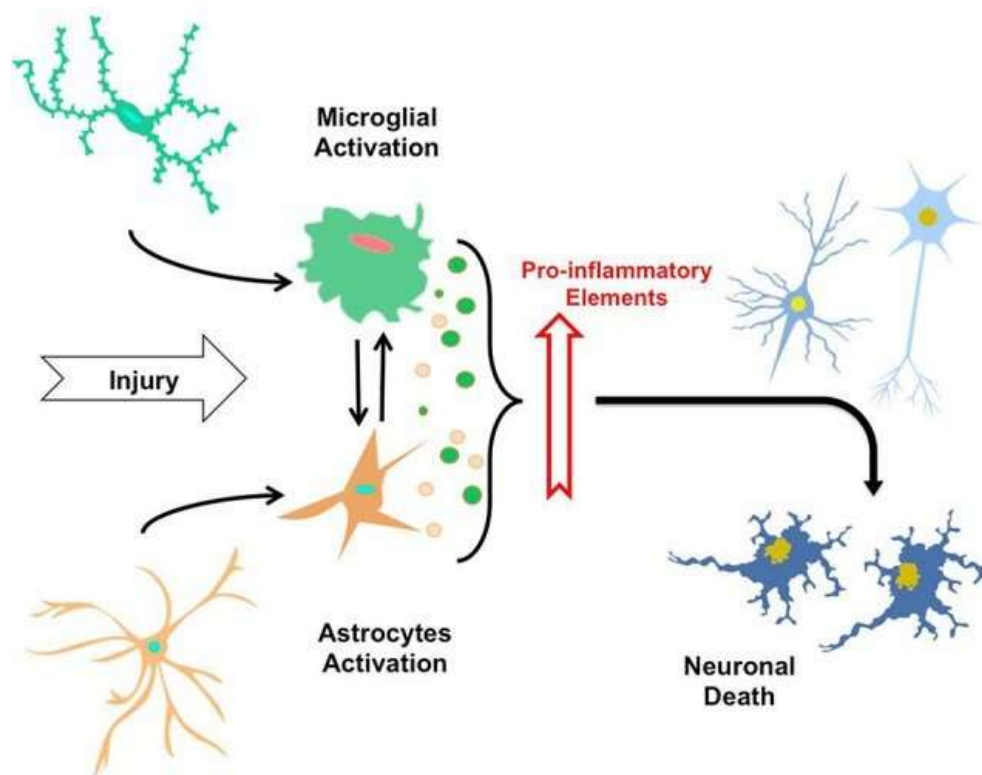


Figure 1.5. The neuroinflammatory process. Damage or injury causes activation of astrocytes and microglia, leading to morphological changes and secretion of pro-inflammatory elements such as cytokines. These process eventually trigger neuronal death (Source: Morales et al. 2014)

Activated astrocytes were known as mediate inflammatory responses in the CNS. They became activated when sensing neuronal damage. They express inflammatory proteins, including cytokines, proteases and complement proteins. Samples of cerebral cortex from a 2-year-old male suffering from Sandhoff disease, from 32-month-old male suffering from Tay-Sachs and from a normal 9-month-old male who died in an accident were analyzed to show how neurodegeneration cause neuroinflammation with loss of neurons in individuals with these disorders. Immunostaining for glial fibrillary acidic protein (GFAP) was shown that the number of astrocytes was increased in the patients' sections with the characteristic of an activated state (Myerowitz et al. 2002).

1.4.2. Neurons

Accumulation of undegraded molecules in lysosomes eventually leads to swelling of cells, deterioration of cell functions and cell death (Tardy et al. 2004). Endoplasmic reticulum and oxidative stress are known to facilitate apoptosis in LSD patients. It has been observed that ER stress marker genes (ATF6, Calnexin, Grp78, and XBP1) and oxidative stress marker genes (superoxide dismutase-2 (SOD2), catalase and thioltransferase-1 (TTase1)) are increased when fibroblast cells from Tay-Sachs and other LSD patients are examined. The increase in expression levels of these genes is an apoptosis indicator in the cells (Wei et al. 2008).

Many signaling events occur in the plasma membrane. The structure of the cavea and lipid rafts in the plasma membrane varies depending on the type and amount of gangliosides (D'Azzo et al. 2006). Gangliosides are important in the structure and organization of cell membranes. Although they are usually located in the outer membrane of the cell, 10% of them are also found in mitochondria and endoplasmic reticulum. Gangliosides are key signaling molecules that play a role in cellular recognition, binding, receptor signal transduction, growth regulation, and differentiation. Besides, due to increased ganglioside levels, cellular stress conditions occur and the apoptotic program is triggered (D'Azzo et al. 2006).

Accumulation of gangliosides and related glycolipids was thought to trigger programmed cell death. When autopsy samples from Tay-Sachs and Sandhoff patients

were examined using the in situ DNA end-labeling technique, apoptosis was observed in the cerebral cortex, brain stem, cerebellum and spinal cord in both of the patient samples. Besides, when Hexa^{-/-} and Hexb^{-/-} (Sandhoff mice) mouse models have been observed using the DNA laddering technique, it was determined that there was apoptosis-associated DNA fragmentation in the cerebral cortex, brain stem, cerebellum and spinal cord of Hexb^{-/-} mice (Huang et al. 1997).

1.4.3. Oligodendrocytes

Oligodendrocytes, a type of glial cells, have a function in the formation of myelin to provide support and insulation to axons (Rasband 2016). The oligodendrocyte provides multiple axons with myelin sheaths and can renew its myelin sheaths three times within a day. Myelination is a necessary step for optimal signal transduction in the CNS (Peferoen et al. 2014).

Activated microglia produces various pro-inflammatory mediators, chemokines, and cytokines. In such environments, oligodendrocytes which are particularly susceptible to these microglia-derived factors resulted in producing poor-quality myelin and oligodendrocyte death (Peferoen et al. 2014).

1.5. The Mouse Brain

The mouse brain is composed of various regions, including the cerebral cortex, hippocampus, thalamus, cerebellum, pons, etc. The cerebral cortex has functions on the perception of sensory information, control of voluntary movements, memory, personality traits, and intelligence. The retrosplenial cortex and secondary motor cortex are functional in memory, spatial cognition and navigation to sensorimotor networks involving the control of movement (Yamawaki et al. 2016). The primary motor and somatosensory cortex were reported to be the most efficient region for pain control. The pain signal is

transmitted from the thalamus to the primary motor cortex via the somatosensory cortex (Lee et al. 2017).

The hippocampus has diverse functions on memory, navigation, and exploration (Rubin et al. 2014). The entorhinal cortex provides input to the hippocampus through two pathways; one via the DG and CA3 fields and the other via CA1 and the subiculum (Wible 2013). Output signals are from CA3 and CA1 to subcortical areas and the entorhinal cortex, respectively. Due to the independent inputs and outputs CA3 and CA1, these areas make separate contributions to spatial or temporal processing of memory (Eichenbaum 2017).

The main function of the thalamus is primary sensory processing by reciprocally communicating and relaying signals between the cerebellar regions and the cortex. It is the central sensory and motor relay station of the brain. It contributes to motor functions by transmitting information from the cerebellum to motor areas of the cerebral cortex. It has also function in the regulation of consciousness, sleep, and alertness (Medsker et al. 2015).

The cerebellum has a function on motor coordination, spatial navigation, and working memory. Purkinje cells in the cerebellum are especially responsible for spatial navigation (Lee et al. 2018).

Pons relays information from the cerebrum to the cerebellum and regulates our sleep/wake cycle, level of consciousness and alertness. It has also a role in stimulating breathing (Vermehren-Schmaedick et al. 2012)

1.6. Behavioral Analysis

Behavioral analysis in animal models has been used to get knowledge about brain function and the neural mechanisms of human diseases. Commonly used laboratory rodents, such as mice and rats, provide a useful tool for studying the behaviors and mechanisms like locomotor ability (Shiotsuki et al. 2010; Gómez-Grau et al. 2017), learning, memory (Nampoothiri et al. 2017), anxiety-related behaviors (Seibenhener and Wooten 2015), etc.

1.6.1. Rotarod Analysis

A rotarod performance test is used to determine motor coordination, balance and motor learning for evaluation of cerebellar deficits in rodents (Shiotsuki et al. 2010). Animals are trained to walk on a rod rotating at the constant speed. Once the animals have learned, the motor performance evaluated. The animals with defective motor coordination fall when the rotation speed exceeds their motor coordination capacity (Nampoothiri et al. 2017). It is also used to measure motor performance in different lysosomal storage disorders such as Sandhoff disease (Gulinello et al. 2008), Mucopolysaccharidosis IIIB (Heldermon et al. 2010), Pompe disease (Sidman et al. 2008), Niemann-Pick type C (Schlegel et al. 2016; Gómez-Grau et al. 2017) and α -Mannosidosis (D'Hooge et al. 2005).

1.6.2. Footprint Analysis

The footprint test is used to assess the gait and identify any abnormal movements in mice. The hind paws of the mice were coated with non-toxic black paint. Then, the animals are allowed to walk along a runway 50 cm long and 10 cm wide (with 10-cm-high walls) in an enclosed box. The test is also used in lysosomal storage disorder like Niemann-Pick type C (Gómez-Grau et al. 2017).

1.6.3. Grip Strength Analysis

Grip strength is generally used tests to determine the effect of lesions, drugs and other toxins on motor functions. During the experiment, the tail of the animal is pulled gently in rear direction, it grasps the bar and pulls with either fore- or hindlimb as long as it can, after which it leaves the bar (Nampoothiri et al. 2017). It is also used in lysosomal

storage disorders such as Niemann-Pick type C (Gómez-Grau et al. 2017), α -Mannosidosis (D'Hooge et al. 2005) and Pompe disease (Foley et al. 2010).

1.6.4. Passive Avoidance Analysis

Passive avoidance test is used to evaluate the fear motivated cognitive memory relating to hippocampal, cortical and striatal connections. There are two chambers. One chamber is well-lit while the other is dark a shock cage. The experiment continues for three days. The first day is the training period. The animal is put into the well-lit chambers and allowed to adapt for about 30 s. Then, the door separating the chambers is opened and the animal moves readily into the dark chamber. The second day, the same procedure is followed and when the animal enters the dark chamber with all four paws in, the door is shut and the animal gets a mild electric foot shock through the floor. The final day, to measure the learning ability, the same protocol is followed without the electrical shock. The latency or uncertainty of the animal to enter the dark chamber is measured (Nampoothiri et al. 2017).

1.6.5. Morris Water Maze Analysis

Morris water maze analysis is used to detect spatial learning and memory deficits. The test is especially sensitive in the determination of the effect of hippocampal lesions. However, deficiencies in the striatum, neocortical areas, basal forebrain, and cerebellum can also be examined. First of all, the animal is trained in the presence of a visible platform and cues on the wall. The animal learns to climb onto the platform to escape from the water and to avoid the necessity to swim. The other days, it is tested to find an invisible platform by using cues on the wall. (Nampoothiri et al. 2017). The memory and learning ability was analyzed with Morris water maze test in different lysosomal storage disorders such as Mucopolysaccharidosis type IIIA (Fu et al. 2016), Fabry disease

(Hofmann et al. 2017), α -Mannosidosis (D'Hooge et al. 2005) and Niemann Pick Type C disease (Schlegel et al. 2016).

1.6.6. Open Field Analysis

An open field maze includes a wall-enclosed area with sufficient height to prevent the mice from escaping. The maze shape is generally square with an area large enough to prompt a feeling of openness in the center of the maze. A simple analysis of general locomotor ability and anxiety-related emotional behaviors are determined via open field test. The technique also provides to the investigation of different pharmacological compounds for anxiolytic or anxiogenic effects (Seibenhener and Wooten 2015). Open Field Analysis was also used to detect anxiety-related behaviors in different lysosomal storage disorders such as Sandhoff disease (Gulinello et al. 2008) Niemann Pick Type C disease (Schlegel et al. 2016), α -Mannosidosis (D'Hooge et al. 2005) and Fabry disease (Hofmann et al. 2017).

1.7. Aim of the Study

NEU3 is the plasma-membrane-associated form of the sialidases. Its biological function towards gangliosides has been revealed in various in vitro studies. The project aimed to understand the contribution of NEU3 to metabolic bypass on the Tay-Sachs mouse model (Hexa^{-/-}) by generating the double deficient mouse model. The newly created Hexa^{-/-}Neu3^{-/-} mice had both complete absences in the activity of the β -Hexosaminidase A and NEU3 enzyme. In this study, it was planned to analyze the biological role of NEU3 on the ganglioside degradation pathway by performing molecular biologic, biochemical, pathological and behavioral analysis.

CHAPTER 2

MATERIALS AND METHODS

2.1. Animals

Hexa^{-/-} deficient mice were obtained from backcrossing of Neu4^{-/-}Hexa^{-/-}Neu1^{-/-} triple mice with wild type mice strain C57/Black6 (Timur et al. 2015). In these crossings mostly brothers and sisters were mated with each other to have mice in the same genetic background. Neu3^{-/-} deficient mice were created by deletion of part of exon3 of Neu3 (Yamaguchi et al. 2012) and donated by Prof. Taeko Miyagi (Division of Cancer Glycosylation Research, Institute of Molecular Biomembrane and Glycobiology, Tohoku Pharmaceutical University, Sendai, Japan) to generate Hexa^{-/-}Neu3^{-/-} double deficient mouse model.

Hexa^{-/-} deficient mice were crossed with Neu3^{-/-} deficient mice to obtain heterozygous females and males. Then, heterozygous brothers and sisters were mated with each other to create wild type (Hexa^{+/+}Neu3^{+/+}), Hexa^{-/-} (Hexa^{-/-}Neu3^{+/+}), Neu3^{-/-} (Hexa^{+/+}Neu3^{-/-}) and Hexa^{-/-}Neu3^{-/-} deficient mice models with the same background (Table 2.1).

All mice have been mated and maintained in the Turkish Council on Animal Care (TCAC) accredited animal facility of Izmir Institute of Technology according to the TCAC guidelines. Mice have been housed under constant temperature and humidity on a 12 h light: dark cycle. The animal care and the use in the experiments were granted by the Animal Care and Use Committee of Izmir Institute of Technology, Izmir, Turkey.

Table 2.1. Crossing of Hexa^{-/-} and Neu3^{-/-} mice

	Breeding pairs	Expected genotypes in the F1 generation
F1 generation	Hexa ^{-/-} ♀ X Neu3 ^{-/-} ♂	Hexa ^{+/-} Neu3 ^{+/-}
	OR	
	Neu3 ^{-/-} ♀ X Hexa ^{-/-} ♂	
	Breeding pairs	Expected genotypes in the F2 generation
F2 generation	Hexa ^{+/-} Neu3 ^{+/-} ♀ X Hexa ^{+/-} Neu3 ^{+/-} ♂	Hexa^{+/+}Neu3^{+/+} (1/16)
		Hexa ^{+/-} Neu3 ^{+/+} (2/16)
		Hexa^{-/-}Neu3^{+/+} (1/16)
		Hexa ^{-/-} Neu3 ^{+/-} (2/16)
		Hexa ^{+/+} Neu3 ^{+/-} (2/16)
		Hexa ^{+/-} Neu3 ^{+/-} (4/16)
		Hexa ^{+/-} Neu3 ^{-/-} (2/16)
		Hexa^{+/+}Neu3^{-/-} (1/16)
		HexA^{-/-}Neu3^{-/-} (1/16)

2.2. Genotyping of Mice

To determine the genotypes of WT, Hexa^{-/-} and Neu3^{-/-} and Hexa^{-/-}Neu3^{-/-} mice, genomic DNA isolation and PCR reactions were applied.

2.2.1. Genomic DNA Isolation

The genotypes of mice were determined after the genomic DNA isolation from the tail of the mice. Tail taken from mouse was put in an eppendorf tube and 500 μ l lysis buffer (10% 1M Tris pH 7.6, 2.5% 0.2M EDTA, 20% SDS, 4% 5M NaCl) with 12 μ l Proteinase K (from 25 μ g/ μ l solution) was added. Samples, incubated overnight in an incubator shaker at 55°C at 70 rpm, were centrifuged at 14.000 rpm for 10 min. The supernatant was transferred into the new tube and the same volume 100% isopropanol was added on the sample. DNA was collected and transferred into a new tube containing 70% ethanol. After 1 min centrifugation at 14.000 rpm, the supernatant was removed and the remaining ethanol was air-dried for 10 min. Then, DNA was dissolved in 200 μ l distilled water and incubated at 55°C for 1 hour. Finally, the concentration of DNA was measured with a Nanodrop spectrophotometer (Thermo Scientific, USA).

2.2.2. PCR Reaction

The PCR for Hexa was performed with 100ng genomic DNA in the 25 μ l reaction mix including 1X PCR buffer (Invitrogen), 3mM MgCl₂, 0.4 mM of dNTPs, 0.4 pmol of forward primers (HexaF and PGK), 0.8 pmol of reverse primer (HexaR), 4% DMSO and 1.75 units Taq polymerase (Invitrogen, USA). Conditions for PCR were; 1 cycle 3 min at 94°C; 30 cycles 45 sec at 94°C, 45 sec at 60°C, 45 sec at 72°C; and 1 cycle 10 min at 72°C. Allele-specific primers for wild type and mutant allele of the Hexa gene was shown in Table 2.2.

Neu3 PCR reaction was carried out with 100 ng DNA in 50 μ l reaction mix including 1X PCR buffer (Invitrogen, USA), 3mM MgCl₂, 0.4 mM of dNTPs, 0.6 pmol of forward primer (551F), 0.3 pmol of reverse primers (552R and 553R) and 2.5 units Taq polymerase (Invitrogen, USA). Conditions for PCR were 1 cycle 3 min at 94°C; 30 cycles 45 sec at 94°C, 30 sec at 56°C, 3 min at 72°C; and 1 cycle 10 min at 72°C. Allele-specific primers for wild type and mutant allele of Neu3 gene were shown in Table 2.2.

After PCR was completed, all PCR samples were run on 1% agarose gel.

Table 2.2. Sequences of used primers in genotyping

Gene	Primer	Binding Location	Primer Sequence
Hexa	HexaF	WT allele	GGCCAGATACAATCATACAG
	HexaR	WT-KO allele	CTGTCCACATACTCTCCCCACAT
	PGK	KO allele	CACCAAAGAAGGGAGCCGGT
Neu3	Neu3F	WT-KO allele	AAGCAGAGAACATTCTTGAGAGAGCACAGC
	552R	KO allele	TCGTGCTTTACGGTATCGCCGCTCCCGATT
	553R	WT allele	GTGAGTTCAAGAGCCATGTTGCTGATGGTG

2.3. Body Weight Measurement

Weight of WT, Hexa^{-/-}, Neu3^{-/-} and Hexa^{-/-}Neu3^{-/-} mice was recorded per week starting from 8 weeks up to 20 weeks.

2.4. Gross Appearance and X-Ray Analysis of Mice

4.5-month-old WT, Hexa^{-/-}, Neu3^{-/-} and Hexa^{-/-}Neu3^{-/-} mice were anesthetized and put on the white paper. Their gross appearance was obtained with a photograph machine.

4.5-month-old WT, Hexa^{-/-}, Neu3^{-/-} and Hexa^{-/-}Neu3^{-/-} mice were anesthetized. When they were under anesthesia, their X-Ray images were obtained at EMOT hospital Kahramanlar/ İzmir.

2.5. Thin-Layer Chromatography Analysis

2.5.1. Lipid Isolation

Acidic and neutral glycosphingolipids should be separated from each other (Sandhoff et al. 2002). Brain, liver, kidney, and testis of 2.5 and 4.5-month-old WT, Hexa^{-/-}, Neu3^{-/-} and Hexa^{-/-}Neu3^{-/-} mice was be obtained with liquid nitrogen and stored at -80oC until used in the experiment.

Starting tissue amount for brain, liver, kidney, and testis was optimized. 25 mg brain and 50 mg liver, kidney and testis tissues were homogenized on ice in 1.5 ml of distilled water with Ultra Turrax Homogenizer (IKA, Germany) (Table 2.3). The sample was sonicated for 3 min with Sonicator (Bandelin, Germany). After the evaporation with a gentle nitrogen stream, the sample was extracted 2 times with 3 ml of acetone by removing the supernatant. Then, the residual pellet was extracted twice with 1.5 ml chloroform/ methanol/ distilled water (10/10/1) and 2 ml of chloroform/ methanol/ distilled water (30/60/8) with 2000 rpm 5 min centrifugation. All supernatant including acidic and neutral glycosphingolipids was collected in the neutral glass tube.

Neutral and acidic glycosphingolipids obtained from chloroform/ methanol/ distilled water extracts were separated on DEAE A-25 columns (bed volume: 300 µl). DEAE A-25 columns were washed three times with chloroform/ methanol/ distilled water (30/60/8) and once with chloroform/ methanol/ distilled water (10/10/1). Then, the extracts were load on the column and wash with 4 ml methanol. The flow-through and wash were taken as neutral glycosphingolipids. Later, acidic glycosphingolipids were eluted with 4 ml of 500 mM methanolic potassium acetate (potassium acetate in methanol).

Acidic glycosphingolipids were desalted Supelclean™ LC-18 SPE column (Sigma-Aldrich, USA). Columns were placed on the Chromabond Vacuum manifold (MachereyNagel) and the vacuum was fixed to 3-4Hg. Supelclean™ LC-18 SPE was washed 2 times with 2 ml methanol and 2 ml 500 mM methanolic potassium acetate. Acidic glycosphingolipids extract was loaded on the column. Then, the column was washed with 10 ml of distilled water. The sample was eluted with 4 ml methanol and 4 ml methanol/chloroform (1/1) in a low vacuum (<2Hg). The eluted sample was evaporated with a gentle nitrogen stream before loading the TLC plate with silica gel (CAMAG, Switzerland).

2.5.2. Thin-Layer Chromatography

The equilibrium time of the tank to form a vaporous environment by the evaporation of solutions was 2 hours 15 min. Acidic and neutral glycosphingolipids were separated with the running solvent chloroform/ methanol/ 0.2% aqueous CaCl₂ (60/35/8).

Table 2.3. The isolated and sprayed amount of neutral and acidic glycosphingolipid for TLC analysis of brain, liver, kidney, testis

Tissue	Weight of Tissue for Isolation	Sprayed Amount of Acidic Glycosphingolipids	Sprayed Amount of Neutral Glycosphingolipids
Brain	25 mg	7.5 mg	7.5 mg
Liver	50 mg	25 mg	7.5 mg
Kidney	50 mg	25 mg	7.5 mg
Testis	50 mg	25 g	15 mg

The neutral and acidic glycosphingolipids fractions were solved in chloroform/methanol/ distilled water (10/10/1) and were sprayed onto the silica covered TLC plates (Merck, USA) with a Linomat V (CAMAG, Switzerland). The amount of neutral and acidic glycosphingolipid loaded onto the plate was optimized in different experiment sets. The optimized amount of sprayed acidic and neutral glycosphingolipids were indicated in Table 2.3. The plate was put into the tank and the samples were run. The migration amount of lipids was optimized as 11 cm.

2.5.3. DEAE Sephadex A25 Ion Exchange Column Preparation

DEAE Sephadex A25 (GE Healthcare) Ion Exchange column was prepared to distinguish acidic and neutral glycosphingolipids (Yu and Ledeen 1972). The DEAE-Sephadex A25 was prepared by washing 1 g of the resin three times with 10 ml methanol/chloroform/ 0.8 M sodium acetate (60/30/8) solution. Then, the resin was incubated overnight in the same solvent for equilibration. This treatment converted the resin from the chloride to the acetate form. Following day, the resin was washed three times with 10 ml of methanol/ chloroform/ water (60/30/8) solution and incubated in methanol/chloroform/ water (60/30/8) solution in glass bottle until usage.

Glass wool (Sigma-Aldrich, USA) was washed with methanol/ chloroform/ water (60/30/8) solution and put into a 225 mm glass Pasteur pipette. Then, the resin was put into the Pasteur pipette. During the experiment, resin didn't completely dry off.

2.5.4. Staining with Orcinol and Visualization

0.04 g orcinol was solved in 10 ml 25% sulfuric acid (2.5 ml H₂SO₄ and 7.5 ml d H₂O) in 50ml glass TLC sprayer (Sigma-Aldrich, USA). Orcinol (Sigma-Aldrich, USA) formed a colorless solution and was stabilized in 5 min. After the completion of the run, the plate was completely dried by airflow. Dye was sprayed on the plates. Then,

the plates were put onto the TLC heater (CAMAG, Switzerland) at 120 °C until the glycosphingolipids bands appear. After the staining, lipids were identified by comparing with brain ganglioside standards (Avanti Polar Lipids). Images of the plate were taken with the HP Scanner.

2.6. Mass Spectrometer Analysis

The brains of 4.5-month-old WT, Hexa^{-/-}, Neu3^{-/-} and Hexa^{-/-}Neu3^{-/-} mice were obtained with liquid nitrogen. 300 mg brain tissue was homogenized in 3 ml methanol with Ultra Turrax Homogenizer (IKA). 3 ml chloroform was added to the suspension and incubated 15 min at 37 °C in an ultrasound bath as 3 times for 3 min for 15 min incubation period.

The tissue pellet was spin down at 2000 rpm for 5 min. The supernatant was taken into a fresh glass vial. Extraction was repeated for tissue pellet once with 2 ml chloroform/methanol/ water (10/10/1) and once with chloroform/methanol/water (30/60/8). Combined supernatants were evaporated with a gentle nitrogen stream.

Total lipids were sent to the mass spectrometry laboratory of Prof. Dr. Roger Sandhoff (Lipid Pathobiochemistry Group, German Cancer Research Center, Heidelberg, Germany) with dry ice. The amount of LacCer, GM3, GM2, GM1, GA2, and GA1 in the total brain was quantified by mass spectrometric analysis.

2.7. Anti GM2/Lamp1 Staining

4.5-month-old WT, Hexa^{-/-}, Neu3^{-/-} and Hexa^{-/-}Neu3^{-/-} mice were anesthetized and fixed with 0.9% NaCl and 4% paraformaldehyde by cardiac perfusion. The brains were incubated in 4% Paraformaldehyde for 16 hours. After that, the brains were incubated in 10% and 20% for 2 hours and 30% sucrose for 16 hours solution at +4 °C. The brains were embedded in OCT (Sigma-Aldrich, USA).

To detect presence of GM2 on lysosomes, 10 µm coronal brain sections obtained by Cryostat (Leica Biosystems, United States, CM1850-UV) was stained by anti-GM2 antibody (KM966) and anti-Lamp1 antibody (Abcam- Cambridge, UK) primary antibody and goat anti-human Dylight 488 Fluorescent antibody (Thermo Scientific, USA) and Goat anti-rabbit Alexa Flour 568 (Abcam, Cambridge, UK) secondary antibody.

Slides were put on the ice to provide tissue defrosting slowly. Sections were washed with 1X PBS for 10 min. Then, sections were treated with ice-cold acetone for 10 min to get permeabilization. After washing 2 times with 1X PBS for 5 min, tissues were blocked with blocking buffer (4% BSA, 10% goat serum and 0.3M glycine in 1XPBS) 1 hour at room temperature. Anti-GM2 (1:500) and Anti-Lamp1 (1:500) primary antibody was diluted in the blocking buffer. 30 µl the diluted primary antibody was applied to tissue sections on the slide. It was incubated overnight at +4oC in a humidified chamber. The slides were washed three times in PBS, 5 min each time. Goat anti-human Dylight 488 fluorescent antibody and Goat anti-rabbit Alexa Flour 568 secondary antibody was diluted in the blocking buffer. 30 µl the diluted secondary antibody was applied to tissue sections on the slide. It was incubated one hour at room temperature in a humidified chamber. Finally, slides were washed 4 times with 1X PBS, 5 min each time. Finally, slides were mounted with fluoroshield mounting medium with DAPI (Abcam, Cambridge, UK) and glass coverslip will be put on the slides. The images will be obtained with Fluorescent Microscopy (Olympus, Germany).

2.8. Transmission Electron Microscopy

Transmission electron microscopy analysis of the cerebral cortex of 4.5-month-old WT, Hexa^{-/-}, Neu3^{-/-} and Hexa^{-/-}Neu3^{-/-} mice was performed in the laboratory of Prof. Dr. Esra Erdemli, which is located in Departments of Histology and Embryology, Ankara University, Ankara, Turkey. Transmission electron microscopy analysis of cerebellar and cerebral cortex neurons, testis, and kidney tissues from 4.5-month-old Hexa^{-/-}Neu3^{-/-} mice was performed in the laboratory of Prof. Dr. Emin Oztas from Departments of Histology and Embryology, GATA Medical School, Ankara, Turkey.

Brain, testis, and kidney were dissected from mice. The tissue pieces were fixed in 2.5% glutaraldehyde in 0.1 M phosphate buffer (pH 7.4), post-fixed in 1% osmium tetroxide in dH₂O, dehydrated using a graded acetone series, and embedded in Araldite CY-212.

Semi-thin sections (1 μ m thick) were stained with toluidine blue and then observed under a light microscope. Then, the areas for histological evaluation of the tissues were selected. Ultrathin sections (40–60 nm thick) were prepared on copper grids (200 mesh). They were double-stained with uranyl acetate and lead citrate. Images were obtained using a Zeiss Libra 120 electron microscope (Carl Zeiss Microscopy GmbH, Germany).

2.9. May-Grunwald Giemsa Staining

Total blood was obtained from 4.5-month-old WT, Hexa^{-/-}, Neu3^{-/-} and Hexa^{-/-} Neu3^{-/-} mice tail to detect the presence of lysosomes on lymphocytes and monocytes cells. May Grunwald (Merck) dye was diluted 1:1 ratio and Giemsa (Merck) dye was diluted 1:9 ratio with water.

3 μ l blood, including 0.1M EDTA, was separated on the slide. Then, it was fixed with methanol 30 sec at room temperature and dried completely. Slides were stained with May-Grunwald 5 min at room temperature and washed with water 5 times for 3 min. Later, slides were stained with Giemsa 30 min at room temperature and washed with water 5 times for 3 min. Finally, the slides were dried and mounted with cytoaseal mounting medium and cover glass.

2.10. Enzyme Activity Assay

The specific activity of Sialidase, β -Hexosaminidase, β -Galactosidase, β -Glucosidase, and α -L-Iduronidase enzymes was measured from brain tissues of 2.5- and

4.5-month-old WT, Hexa^{-/-}, Neu3^{-/-} and Hexa^{-/-}Neu3^{-/-} to see the effect of NEU3 on Tay Sachs mouse model.

A standard curve with 4-Methylumbelliferyl (4-MU) was prepared. Substrates were fluorescently tagged with 4-MU. Each enzyme digested the specific substrate and 4-MU was released. Enzymes and their specific substrates were shown in Table 2.4. The released concentration of each 4-MU was calculated depending on the standard curve by Fluorescence Spectrophotometer (Shimadzu) in emission wavelength of 365 nm and excision wavelength of 445 nm. The protocol was optimized to measure the specific activity of Sialidase (Table 2.5), β -Galactosidase (Table 2.6), β -Glucosidase (Table 2.7), α -L-Iduronidase (Table 2.8) and β -Hexosaminidase (Table 2.9) enzymes.

Table 2.4. Substrates used for enzyme activity assay

Enzyme	Substrate
Sialidase	2'-(4-Methylumbelliferyl)- α -D-N-acetylneuraminic acid
β -Hexosaminidase	4-Methylumbelliferyl-2-asetamido-4,6-0-benziliden-2-deoksi- β -D-glucopyranoside
β -Galactosidase	4-Methylumbelliferyl β -D-galactopyranoside
β -Glucosidase	4-Methylumbelliferyl β -D-glucopyranoside
α -L-Iduronidase	4-Methylumbelliferyl α -L-iduronide

25 mg brain tissue was homogenized in 200 μ l distilled water with Ultra Turrax Homogenizer (IKA) and sonicated at 60 V for 10 sec with Sonicator (Bandelin). To measure the activity of Sialidase, β -Galactosidase, β -Glucosidase, and α -L-iduronidase, 40 μ l of the homogenate was diluted in 0.5 M sodium acetate at pH 4.5 with 1/5 ratio. The homogenate was ready to set up a reaction.

Table 2.5. Sialidase enzyme activity assays

Blank	Sample
50µl substrate	50µl substrate
40µl 0.5M sodium acetate buffer (pH4.5)	40µl 0.5M sodium acetate buffer (pH4.5)
10µl dH2O	10µl sample
30 min incubation at 37°C	
3.9 ml 0.2M glycine buffer (pH 10.8) to stop reaction	

Table 2.6. β-Galactosidase enzyme activity assays

Blank	Sample
25µl substrate	25µl substrate
50µl 0.1M NaCl	50µl 0.1M NaCl
25µl dH2O	25µl sample
10 min incubation at 37°C	
3.9ml 0.2M glycine buffer (pH10.8) to stop reaction	

Table 2.7. β-Glucosidase enzyme activity assays

Blank	Sample
50µl substrate	50µl substrate
40µl 0.5M sodium acetate buffer (pH4.5)	40µl 0.5M sodium acetate buffer (pH4.5)
10µl dH2O	10µl sample
30 min incubation at 37°C	
3.9ml 0.2M glycine buffer (pH10.8) to stop reaction	

Table 2.8. α -L-Iduronidase enzyme activity assays

Blank	Sample
50 μ l substrate	50 μ l substrate
40 μ l 0.5M sodium acetate buffer (pH4.5)	40 μ l 0.5M sodium acetate buffer (pH4.5)
10 μ l dH ₂ O	10 μ l sample
30 min incubation at 37°C	
3.9ml 0.2M glycine buffer (pH10.8) to stop reaction	

Table 2.9. β -Hexosaminidase enzyme activity assay

Blank	Sample
75 μ l substrate	75 μ l substrate
25 μ l dH ₂ O	25 μ l sample
30 min incubation at 37°C	
3.9ml 0.2M glycine buffer (pH10.8) to stop reaction	

For β -Hexosaminidase enzyme activity, 20 μ l of the homogenate was diluted in 0.1 M sodium citrate at pH 4.3 with 1/5 ratio. To measure only β -Hexosaminidase enzyme activity diluted homogenates were incubated at 55°C for three hours before setting reaction. The reactions were prepared on ice as shown in Table 2.9.

The protein concentration of the samples was measured by Bradford Reagent (Sigma-Aldrich, USA). For this purpose, 5 μ l of diluted homogenates were diluted in their specific buffer with 1/4 ratio. 5 μ l of sample and 250 μ l Bradford reagent was incubated for 10 min at room temperature in dark and absorbance of each was measured in a spectrometer (Bio-Rad) at 595 nm. Protein concentration was determined depending on the BSA standard curve. To calculate specific enzyme activity following calculation will be used for each sample.

Enzyme Activity (nmol/hour/ml) = Concentration of 4-MU x (Final reaction volume/Sample volume) x (1/time in hour)

Specific Enzyme Activity (nmol/mg protein/hour) = Enzyme activity / protein concentration

2.11. Effects of GM2 Accumulation to CNS

2.11.1. Sample Preparation

WT, Hexa^{-/-}, Neu3^{-/-} and Hexa^{-/-}Neu3^{-/-} mice were anesthetized and fixed with 0.9% NaCl and 4% paraformaldehyde with cardiac perfusion. The brains were incubated in 4% paraformaldehyde for 16 hours. After that, the brains were incubated in 10% and 20% for 2 hours and 30% sucrose for 16 hours solution at +4 °C. The brains were embedded in OCT (Sigma-Aldrich, USA). The coronal brain sections obtained by Cryostat (Leica Biosystems, United States, CM1850-UV).

2.11.2. Hematoxylin–Eosin Staining

Cortex and cerebellum of 4.5-month-old WT, Hexa^{-/-}, Neu3^{-/-} and Hexa^{-/-}Neu3^{-/-} mice were stained with Hematoxylin–Eosin to detect tissue morphology.

The 10 µm coronal brain sections from the mice at the indicated ages were stained with Gill's hematoxylin (Merck, Germany) for 3 min, followed by differentiation in 70% ethanol:1 N HCl (99:1, v/v), washing under running tap water and staining with eosin Y solution 0.5% alcoholic (Merck, Germany) for 1 min. Finally, they were dehydrated 2 times respectively with 95% ethanol, 100% ethanol, and xylene for 2 min each and mounted with mounting medium.

2.11.3. TUNEL Staining

Terminal dUTP nick end-labeling (TUNEL) analysis was performed using the ApopTag Fluoresceinin Situ Apoptosis Detection Kit (Millipore, USA) according to the manufacturer's specifications. Briefly, the brain sections from each group (n=4) were fixed with 1% paraformaldehyde in PBS for 10 minutes at room temperature and post-fixed in precooled ethanol: acetic acid solution (2:1) for 5 minutes at -20°C. The sections were incubated with terminal deoxynucleotidyl transferase at 37°C for 1 hour and followed by incubation with an anti-digoxygenin conjugate for 30 minutes at room temperature. Propidium iodide (0.5µg/mL) was added as a nuclear counterstain. The slides were mounted with mounting medium including antifade. Images were obtained using a fluorescence microscope under 488 nm fluorescence light (Olympus, Germany).

2.11.4. Anti-NeuN Staining

To detect the presence of neurons on the mice brain (n=3), 10 µm coronal brain sections were stained with Anti-NeuN (Cell Signaling Technology, The Netherlands) and Goat anti-rabbit Alexa Flour 568 (Abcam, Cambridge, UK) secondary antibody.

The slides were put on the ice to provide tissue defrosting slowly. The sections were washed with 1X PBS for 10 min. Then, they were also blocked in a humidified chamber with 5% goat serum and 0.3% Triton X-100 in PBS. Anti-NeuN was diluted in the blocking buffer at 1:50. They were applied overnight at 4 °C in a humidified chamber. The binding of NeuN was visualized using goat anti-rabbit Alexa Fluor 568 antibody (1:500) in blocking buffer. It was incubated one hour at room temperature in a humidified chamber. Finally, slides were washed 4 times with 1X PBS, 5 min each time and mounted with Fluoroshield mounting medium with DAPI (Abcam, Cambridge, UK) and images were obtained using fluorescence microscopy (Olympus, Germany).

2.11.5. Anti-GFAP Staining

To detect the presence of glial fibrillary acidic protein on the mice brain (n=3), 10 µm coronal brain sections were stained with Anti-GFAP (Sigma-Aldrich, USA) primary antibody and Goat anti-mouse Alexa Fluor 568 (Abcam, Cambridge, UK) secondary antibody.

The slides were put on the ice to provide tissue defrosting slowly. The sections were washed with 1X PBS for 10 min. Then, they were also blocked in a humidified chamber with 5% goat serum and 0.3% Triton X-100 in PBS. Anti-GFAP was diluted to 1:200 in blocking buffer and applied overnight at 4 °C in a humidified chamber. The slides were washed three times in PBS, 5 min each time. The binding of GFAP was visualized using goat anti-mouse Alexa Fluor 568 antibody (1:500) in blocking buffer. It was incubated one hour at room temperature in a humidified chamber. Finally, slides were washed 4 times with 1X PBS, 5 min each time and mounted with Fluoroshield mounting medium with DAPI (Abcam, Cambridge, UK) and images were obtained using fluorescence microscopy (Olympus, Germany).

2.11.6. Anti-CNPase Staining

To detect the presence of oligodendrocytes on the mice brain (n=3), 10 µm coronal brain sections were stained with anti-CNPase primary antibody (Cell Signaling Technology, The Netherlands) and anti-rabbit Alexa Fluor 488 (Abcam, Cambridge, UK) secondary antibody.

The slides were put on the ice to provide tissue defrosting slowly. The sections were covered with 4% paraformaldehyde in 1X PBS for 15 min at room temperature. Then, they were rinsed three times in 1X PBS for 5 min each. They were incubated with ice-cold 100% methanol for 10 min at -20°C and rinsed in 1X PBS for 5 min. Lastly, they were also blocked in a humidified chamber with 5% goat serum and 0.3% Triton X-100 in PBS. Anti-CNPase (1:100) was diluted in the blocking buffer. They were applied

overnight at 4 °C in a humidified chamber. The slides were washed three times in PBS, 5 min each time. The binding of CNPase was visualized using goat anti-rabbit Alexa Fluor 488 antibody (1:500) in blocking buffer. It was incubated one hour at room temperature in a humidified chamber. Finally, slides were washed 4 times with 1X PBS, 5 min each time and mounted with Fluoroshield mounting medium with DAPI (Abcam, Cambridge, UK) and images were obtained using fluorescence microscopy (Olympus, Germany).

2.12. Behavioral Analysis

2.12.1. Rotarod Test

WT (n=8), Hexa^{-/-} (n=7), Neu3^{-/-} (n=10), and Hexa^{-/-}Neu3^{-/-} (n=11) mice at 2.5-months-old of age, WT (n=7), Hexa^{-/-} (n=6), Neu3^{-/-} (n=5), and Hexa^{-/-}Neu3^{-/-} (n=2) mice at 3.5-month-old of age and WT (n=19), Hexa^{-/-} (n=14), Neu3^{-/-} (n=17), and Hexa^{-/-}Neu3^{-/-} (n=16) mice at 4.5-month-old of age were subjected to the rotarod test. All mice were first trained to walk on the rotarod at constant rotation speeds in 5 min. Then, the session was performed with the rotarod rotating at an incremental speed starting at 4 rpm and accelerating over a 5 min period up to 40 rpm. The time on the rod will be recorded with Sedacomv2.0 (Harvard Apparatus, USA). Obtaining the required amount of animals at the same time is difficult. Therefore, this experiment was done on different experiment sets and results were put together.

2.12.2. Footprint Test

WT (n=3), Hexa^{-/-} (n=3), Neu3^{-/-} (n=3), and Hexa^{-/-}Neu3^{-/-} (n=4) mice at 4.5-month-old of age were subjected to the footprint test. The fore and hind paws of WT, Hexa^{-/-}, Neu3^{-/-} and Hexa^{-/-}Neu3^{-/-} mice were painted with non-toxic ink. Then, the

mice will be walking on the white paper. Their walking pattern was obtained with the HP Scanner. In this test, to avoid possible confounding effects in gait abilities due to practice in other behavioral tasks, a separate set of animals was used.

2.12.3. Grip Strength Measurement Test

2.5-month-old WT (n=5), Hexa^{-/-} (n=5), Neu3^{-/-} (n=4), and Hexa^{-/-}Neu3^{-/-} (n=4) mice; and 4.5-month-old WT (n=4), Hexa^{-/-} (n=4), Neu3^{-/-} (n=4), and Hexa^{-/-}Neu3^{-/-} (n=4) mice were subjected to forelimb grip strength test with a Grip Strength Meter (IITC Life Science, USA). The gauge was reset to 0 g after stabilization, and a mouse was led to spontaneously grab a T-shaped bar. The connection of the bar to a digital force transducer allowed quantification of strength as a pull force in grams. The order of mice tested was randomized, and the inspector was blinded to genotypes of mice.

2.12.4. Passive Avoidance Test

WT (n=4), Hexa^{-/-} (n=6), Neu3^{-/-} (n=5), and Hexa^{-/-}Neu3^{-/-} (n=6) mice at 2.5-month-old of age and WT (n=10), Hexa^{-/-} (n=6), Neu3^{-/-} (n=10), and Hexa^{-/-}Neu3^{-/-} (n=6) mice at 4.5-month-old of age were subjected to the passive avoidance test. The test was conducted as previously described. The apparatus consisted of a two-compartment box, a light compartment connected to a dark compartment by a guillotine door. When the animal stepped into the dark compartment with all four paws, the door was closed and a 0.2 mA foot shock was delivered for 1 s. The latency times for entering the dark compartment were measured in the training test and the retention test 24 h later. The maximum entry latency allowed in the retention session was 300 s. A Shut Avoid Vol. 1.8 (Harvard Apparatus, USA) was used for the experiment.

2.12.5. Morris Water Maze Test

2.5-month-old WT (n=4), Hexa^{-/-} (n=8), Neu3^{-/-} (n=3), and Hexa^{-/-}Neu3^{-/-} (n=3) mice; and 4.5-month-old WT (n=6), Hexa^{-/-} (n=3), Neu3^{-/-} (n=3), and Hexa^{-/-}Neu3^{-/-} (n=3) mice were subjected to Morris Water Maze Test to examine their spatial memory and hippocampal damage. The test was conducted as previously described (Calhan and Seyrantepe 2017). The first three days were for acquisition training with a visible platform (1 cm above the platform) located in a circular pool (diameter, 140 cm; depth, 45 cm) filled with dry milk in water (22°C). Each mouse had 60 secs to reach the platform. Each day, the location of cues and platform were changed and the mice were released into the water at 3 different locations. Days 4-8 were for reversal training with an invisible platform (1 below the platform). Each day, platform location was stable and mice were put into water from 3 different locations and given 90 s to find the platform. If they exceeded the given time, they were guided and allowed to stay on the platform for 5 s on the first day. Measurements were acquired with a Sony camera (SSC-G18) centrally positioned above the water tank. Behavioral differences were analyzed using the Panlab SMART Video Tracking System v0.3 (Harvard Apparatus, USA). Animals were allowed to dry under a heat lamp after each trial to avoid hypothermia, and all experiments were started at the same time each day.

2.12.6. Open Field Test

2.5-month-old WT (n=8), Hexa^{-/-} (n=8), Neu3^{-/-} (n=9), and Hexa^{-/-}Neu3^{-/-} (n=13) mice; and 4.5-month-old WT (n=15), Hexa^{-/-} (n=10), Neu3^{-/-} (n=15), and Hexa^{-/-}Neu3^{-/-} (n=17) mice were subjected to open field test. The apparatus for this assay consisted of a 40x40 cm in surface area and was surrounded from all sides by a 40 cm transparent wall. A digital camera was mounted directly above the apparatus. Mice were placed in one of the corners of the open field and allowed to explore undisturbed for 5

min. Behavioral differences were analyzed using the Panlab SMART Video Tracking System v0.3 (Harvard Apparatus, USA).

2.13. Statistical Analysis

GraphPad QuickCalcs (GraphPad Software, La Jolla, CA, USA) statistical software was used for the statistical analysis. All values are expressed as the mean \pm SEM. The differences were tested using one-way-ANOVA for behavioral analysis and immunofluorescence analysis. A p-value of less than 0.05 was considered statistically significant.

CHAPTER 3

RESULTS

3.1. Genotyping of Knockout Mice

The genotypes of WT, Hexa^{-/-}, Neu3^{-/-} and Hexa^{-/-}Neu3^{-/-}-mice were determined by the PCR with Hexa and Neu3 allele-specific primers (Table 2.2).

Hexa PCR reaction had been carried out with primers HexaF, HexaR, and PGK. HexaF and HexaR generated a DNA fragment of 420 bp derived from the WT allele while primers PGK and HexaR generated a DNA fragment of 210 bp derived from the KO allele (Figure 3.1)

Neu3 PCR reaction had been carried out with primers Neu3F, 552R and 553R. Neu3F and 553R generated a DNA fragment of 1022 bp derived from WT allele, whereas 551F and 552R generated a DNA fragment of 601 bp derived from the KO allele (Figure 3.1)

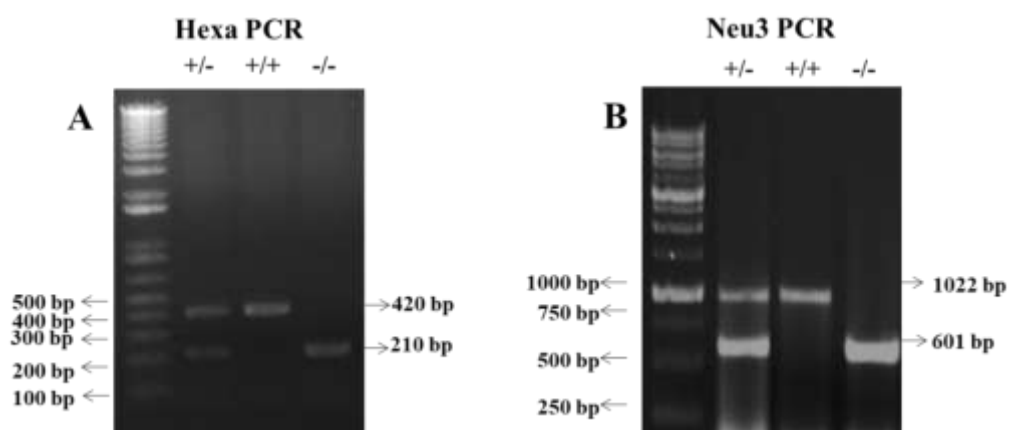


Figure 3.1. Gel images of Hexa (A) and Neu3 (B) PCR products

WT, Hexa^{-/-}, Neu3^{-/-} mice strain were produced offsprings. However, it was realized that Hexa^{-/-}Neu3^{-/-} double deficient mice were mostly infertile. To get Hexa^{-/-}Neu3^{-/-} mice with high probability, Hexa^{+/-}Neu3^{-/-} female mice were crossed with Hexa^{+/-}Neu3^{-/-} male mice or Hexa^{-/-}Neu3^{+/-} female mice were crossed with Hexa^{-/-}Neu3^{+/-} male mice.

3.2. Body Weight Measurement

Body Weight of WT, Hexa^{-/-}, Neu3^{-/-} and Hexa^{-/-}Neu3^{-/-} male and female mice were recorded per week from 8 weeks to 20 weeks. It was observed that Hexa^{-/-}Neu3^{-/-} female mice started to lose weight after 17 weeks and continued to lose weight until its death at the age of nearly 20 weeks (Figure 3.2 A). The body weight ratio of 20-week-old Hexa^{-/-}Neu3^{-/-} male mice was significantly decreased as 0.70 fold compared to its age-matched WT male mice ($p < 0.0001$) (Figure 3.2 B). Similarly, it was determined that Hexa^{-/-}Neu3^{-/-} male mice started to lose weight after the 15 weeks and continue losing weight until its death at the age of nearly 20 weeks ($p < 0.0001$) (Figure 3.2 C). The body weight ratio of 20-week-old Hexa^{-/-}Neu3^{-/-} male mice was decreased as 0.72 fold compared to its age-matched WT male mice (Figure 3.2 D).

Gross appearance 4.5-month-old WT, Hexa^{-/-}, Neu3^{-/-} and Hexa^{-/-}Neu3^{-/-} mice was obtained (Figure 4E). The difference between the bodies of the mice can be detected by the eye. The length of Hexa^{-/-}Neu3^{-/-} mice was much smaller than age-matched WT, Hexa^{-/-} and Neu3^{-/-} mice (Figure 3.2 E).

X-Ray images of 4.5-month-old WT, Hexa^{-/-}, Neu3^{-/-} and Hexa^{-/-}Neu3^{-/-} mice were obtained at EMOT hospital Kahramanlar/ İzmir when they were under anesthesia (Figure 4H). It was observed that there was a hump on the back of the neck only in the Hexa^{-/-}Neu3^{-/-}. This means that there were skeletal deformations in the body of Hexa^{-/-}Neu3^{-/-} (Figure 3.2 F).

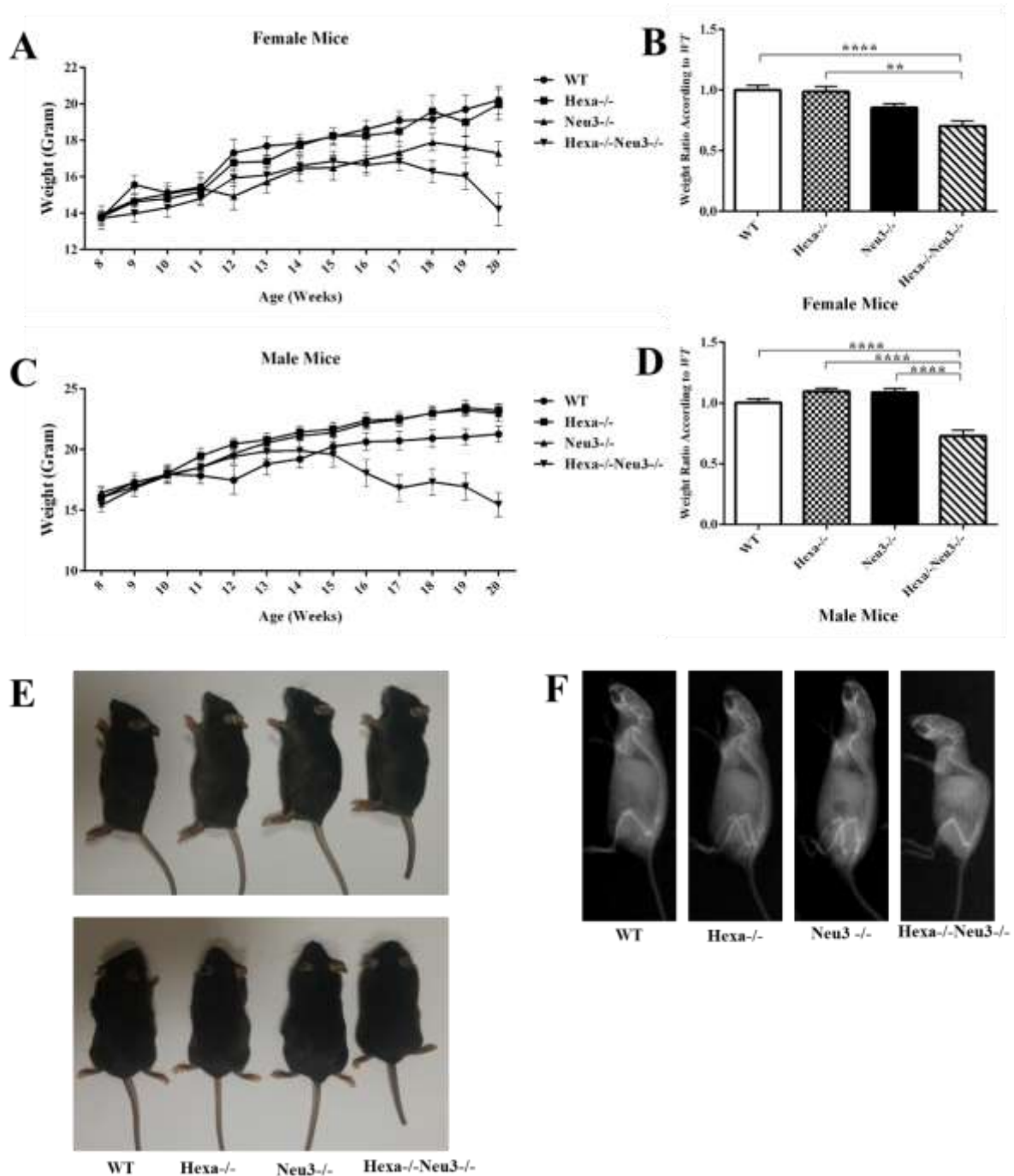


Figure 3.2. Weight measurements of WT, Hexa^{-/-}, Neu3^{-/-} and Hexa^{-/-}Neu3^{-/-} female (A) and male (C) mice starting from 8 weeks up to 20 weeks. The weight ratio of 20 weeks old female (B) and male (D) mice according to WT mice. Gross appearance of 4.5-month-old WT, Hexa^{-/-}, Neu3^{-/-} and Hexa^{-/-}Neu3^{-/-} male mouse (E). X-ray images of 4.5-month-old WT, Hexa^{-/-}, Neu3^{-/-} and Hexa^{-/-}Neu3^{-/-} male mouse (F) Data show mean \pm SEM of measurements. Significant levels of data were determined using the one-way ANOVA. (* $p < 0.05$, ** $p < 0.025$, *** $p < 0.001$ and **** $p < 0.0001$)

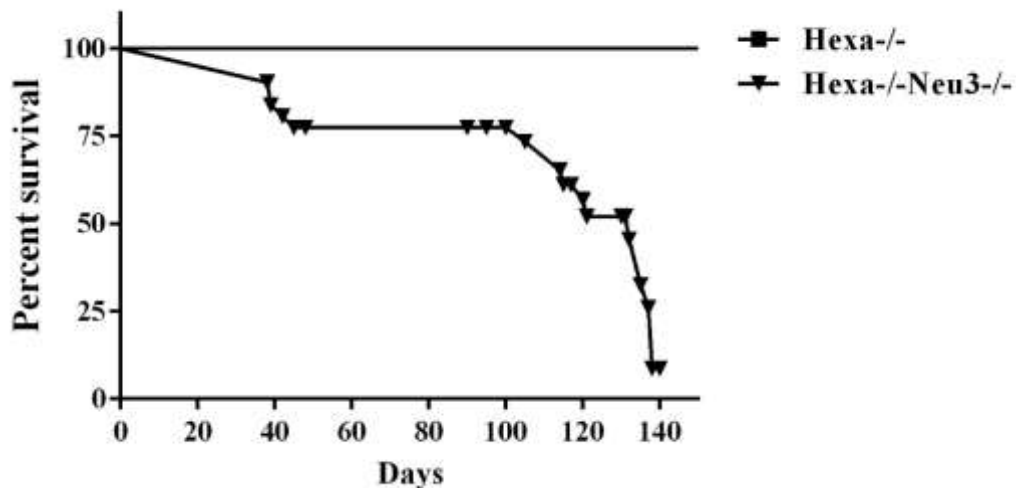


Figure 3.3. Survival graph of Hexa-/- and Hexa-/-Neu3-/- mice

It was realized that disease progression was different from mice to mice. Hexa-/- Neu3-/- double deficient mice have tremors, muscle weakness and an ataxic gait in 5 months of age. Hexa-/-Neu3-/- mice live a maximum of 5 months. Sudden deaths and the disease symptoms are observed at different times until 5 months of age (Figure 3.3). To see the progressive effect of GM2 accumulation, mice were analyzed at specific periods. Tay-Sachs disease phenotypes were tested at 2.5- and 4.5-month-old Hexa-/-Neu3-/- double deficient mice.

3.3. Thin-Layer Chromatography Analysis

It was known from previous works that there is GM2 accumulation in Hexa-/- mice brain (Sango et al. 1995; Seyrantepe, Lema, et al. 2010) and SM2a (gangliosylceramide sulfate) accumulation in Hexa-/- kidney (Sandhoff et al. 2002). The TLC from liver and testes of Hexa-/- mice has not been carried out. Thin-layer chromatography analyses were optimized for our laboratory conditions with DEAE Sephadex A25 Ion Exchange Column. Brain, liver, kidney, and testis of 2.5 and 4.5-month-old WT, Hexa-/-, Neu3-/-, and Hexa-/-Neu3-/- mice were analyzed.

Acidic and neutral glycosphingolipids from the brain (Figure 3.4 A), testes (Figure 3.5 A), liver (Figure 3.6 A) and kidney (Figure 3.7 A) of 2.5- and 4.5-month-old WT, Hexa^{-/-}, Neu3^{-/-} and Hexa^{-/-}Neu3^{-/-} mice were analyzed. 7.5 mg acidic and neutral GSLs from the brain, 25 mg acidic and 15 mg neutral GSLs from testes and 25 mg acidic and 7.5 mg neutral GSLs from liver and kidney were applied on the TLC plate.

Our results showed that there are differences in both acidic and neutral GSL in the brain (Figure 3.4), testes (Figure 3.5), liver (Figure 3.6) and kidney (Figure 3.7).

TLC analysis from the brain showed that GM2 and GA2 ganglioside levels increased in 2.5 and 4.5-month-old Hexa^{-/-} and Hexa^{-/-}Neu3^{-/-} mice compared to WT and Neu3^{-/-} mice. However, the most affected one was Hexa^{-/-}Neu3^{-/-} mice. Stored GM2 levels in Hexa^{-/-}Neu3^{-/-} mice compared to Hexa^{-/-} mice significantly increased 10 fold and 13 fold in 2.5 and 4.5-month-old mice, respectively. Hexa^{-/-}Neu3^{-/-} mice also had a notable increase in accumulated GA2 levels compared to Hexa^{-/-} mice as 1.7 fold and 3.5 fold in 2.5 and 4.5-month-old mice, respectively. All of the results were shown that there was a progressive increase in the GM2 and GA2 level of 2.5-month-old Hexa^{-/-}Neu3^{-/-} mice (Figure 3.4 B and C, respectively) and 4.5-month-old Hexa^{-/-}Neu3^{-/-} mice (Figure 3.4 D and E, respectively)

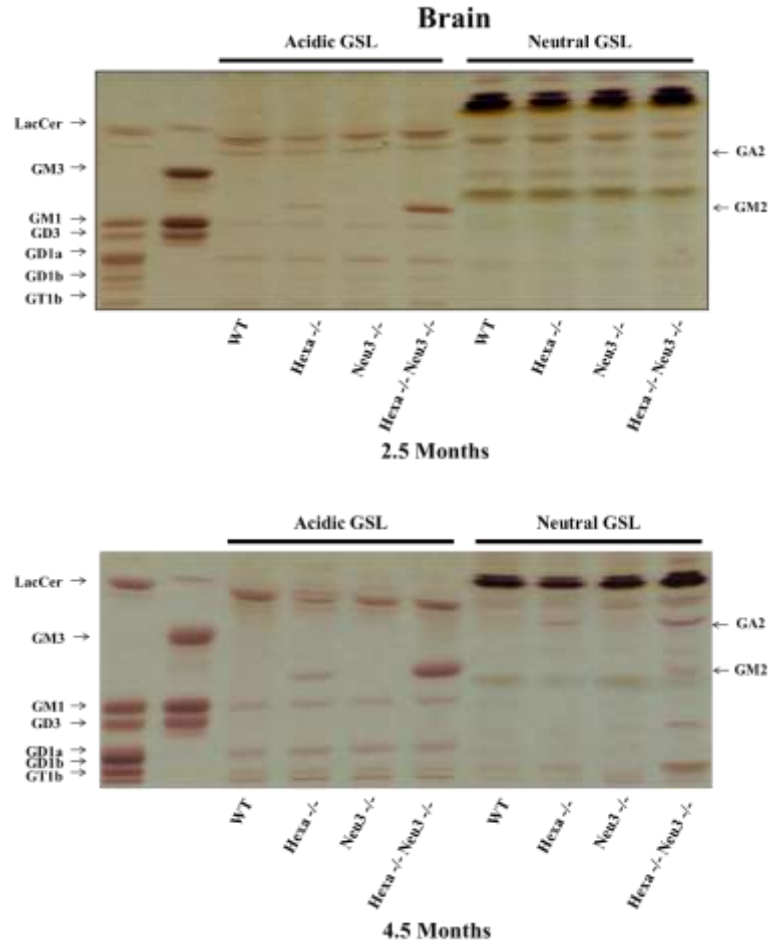
2 different GM2 isoforms were observed only in testes of Hexa^{-/-}Neu3^{-/-} mice. Age-dependent accumulations of GM2 were observed in Hexa^{-/-}Neu3^{-/-} mice as 2 fold (Figure 3.5 B and C). GM2 wasn't detected in WT, Hexa^{-/-} and Neu3^{-/-} mice.

GM2 was detected WT, Hexa^{-/-}, Neu3^{-/-} and Hexa^{-/-}Neu3^{-/-} mice liver. GM2 level significantly increased in 2.5 and 4.5-month-old Hexa^{-/-}Neu3^{-/-} mice compared to WT mice as 4.6 fold and 17 fold, respectively. Age-dependent accumulation in the amount of GM2 was observed in the liver of Hexa^{-/-}Neu3^{-/-} mice. (Figure 3.6 B and C).

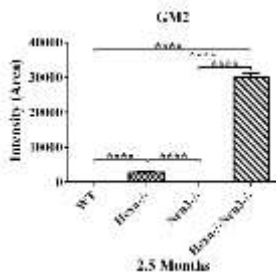
Age-dependent accumulation in the amount of GM2 was also observed in the kidney Hexa^{-/-}Neu3^{-/-} mice (Figure 3.7 B and C).

Thin-layer chromatography analyses of Hexa^{-/-}Neu3^{-/-} mice demonstrated that GM2 accumulation found in the brain, testis, liver, and kidney of these mice.

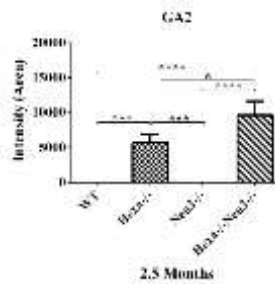
A



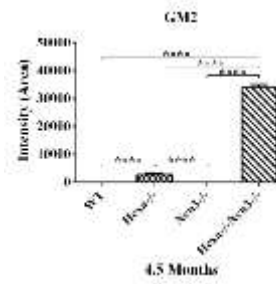
B



C



D



E

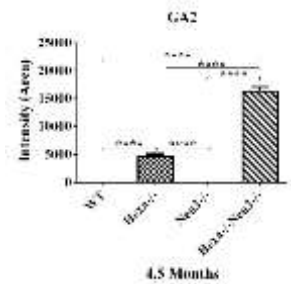


Figure 3.4. TLC images of orcinol-stained acidic and neutral glycosphingolipids from the brain of 2.5- and 4.5-month-old WT, Hexa^{-/-}, Neu3^{-/-} and Hexa^{-/-}Neu3^{-/-} mice (A). 7.5 mg acidic and neutral GSL from the brain were applied on the TLC plate. GM2 and GA2 levels were shown in the brain of 2.5- (B and C, respectively) and 4.5- (D and E, respectively) month-old WT, Hexa^{-/-}, Neu3^{-/-} and Hexa^{-/-}Neu3^{-/-} mice. Data show mean ± SEM of measurements. Significant levels of data were determined using the one-way ANOVA (*p<0.05, ***p<0.001 and ****p<0.0001). Arrows indicate the positions of the ganglioside standards. (n=6 for 4.5-month-old mice and n=4 for 2.5-month-old mice)

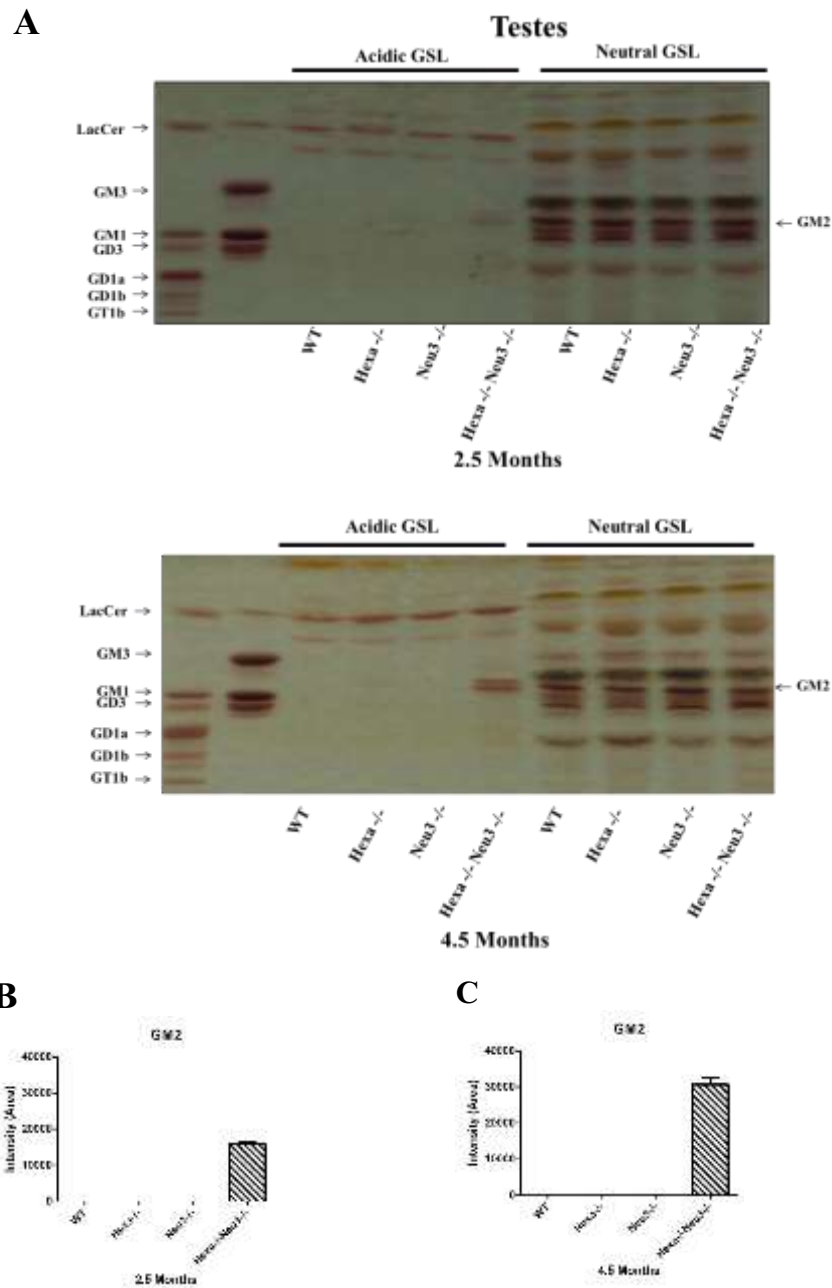


Figure 3.5. TLC images of orcinol-stained acidic and neutral glycosphingolipids from testes of 2.5- and 4.5-month-old WT, Hexa^{-/-}, Neu3^{-/-} and Hexa^{-/-}Neu3^{-/-} mice (A). 25 mg acidic and 15 mg neutral GSL from testes were applied on the TLC plate. GM2 levels were shown in the testes of 2.5- (B) and 4.5- (C) month-old WT, Hexa^{-/-}, Neu3^{-/-} and Hexa^{-/-}Neu3^{-/-} mice. Significant levels of data were determined using the one-way ANOVA ****p<0.0001). Arrows indicate the positions of the ganglioside standards. (n=3 for 4.5-month-old mice and n=3 for 2.5-month-old mice)

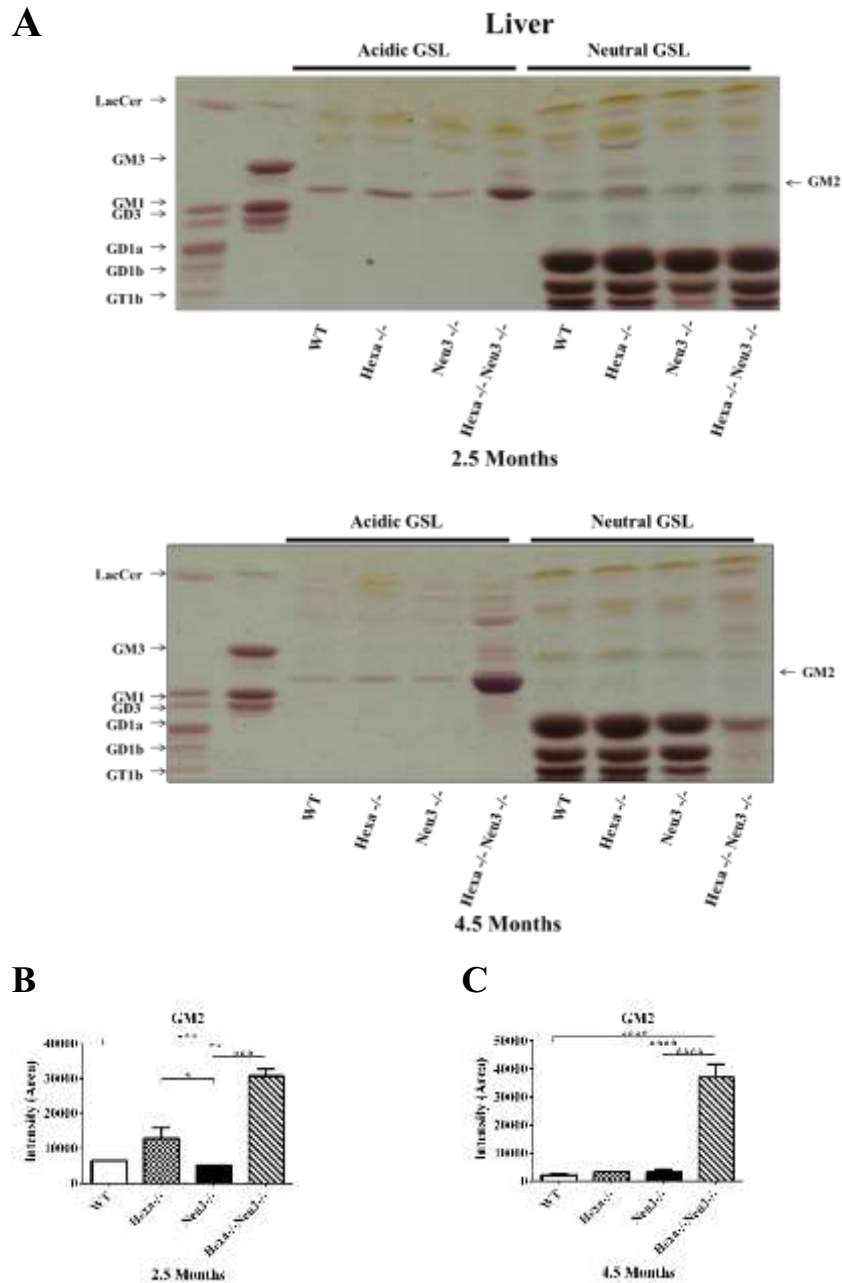


Figure 3.6. TLC images of orcinol-stained acidic and neutral glycosphingolipids from the liver of 2.5- and 4.5-month-old WT, Hexa^{-/-}, Neu3^{-/-} and Hexa^{-/-}Neu3^{-/-} mice (A). 25 mg acidic and 7.5 mg neutral GSL from the liver were applied on the TLC plate. GM2 level was shown in the liver of 2.5- (B) and 4.5- (C) month-old WT, Hexa^{-/-}, Neu3^{-/-} and Hexa^{-/-}Neu3^{-/-} mice. Data show mean \pm SEM of measurements. Significant levels of data were determined using the one-way ANOVA (* $p < 0.05$, ** $p < 0.025$, *** $p < 0.001$ and **** $p < 0.0001$). Arrows indicate the positions of the ganglioside standards. (n=3 for 4.5-month-old mice and n=2 for 2.5-month-old mice)

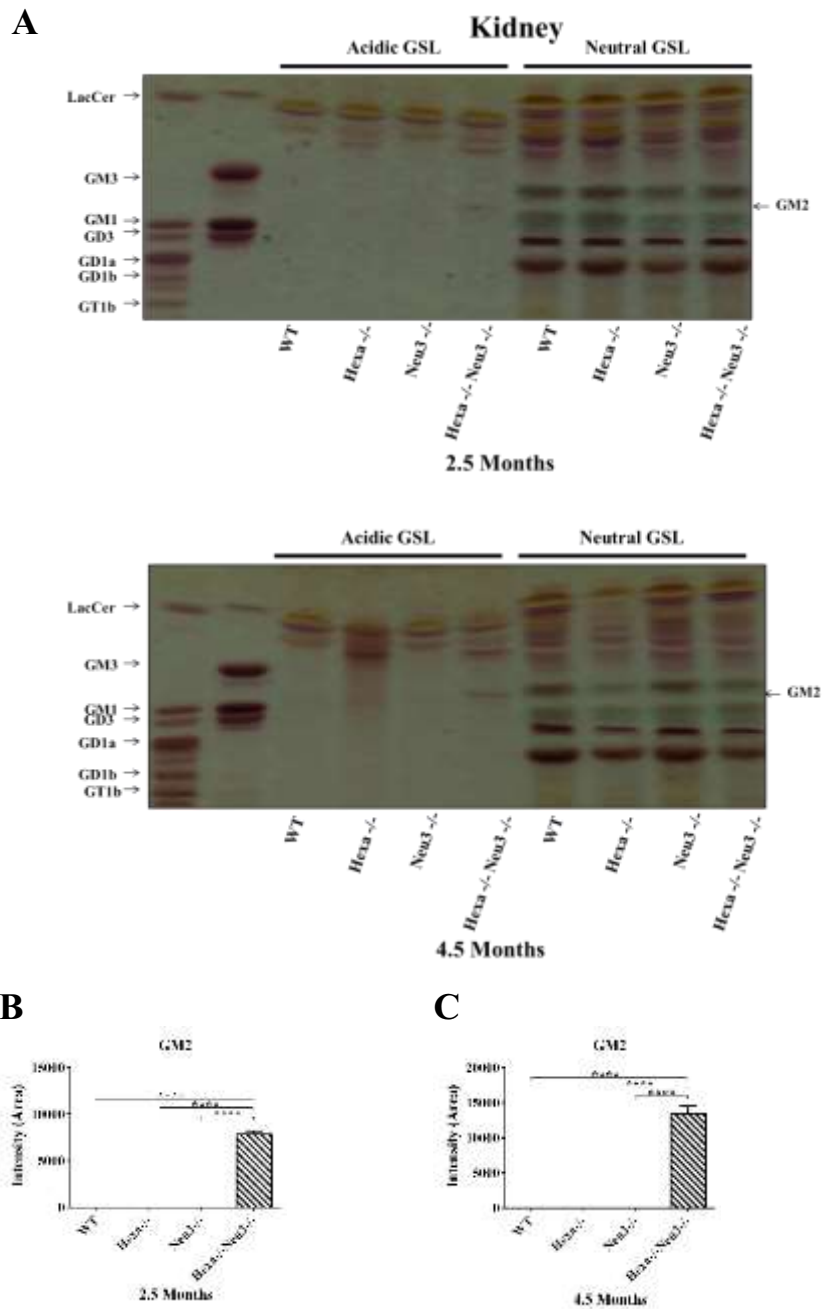


Figure 3.7. TLC images of orcinol-stained acidic and neutral glycosphingolipids from the kidney of 2.5- and 4.5-month-old WT, *Hexa*^{-/-}, *Neu3*^{-/-} and *Hexa*^{-/-}*Neu3*^{-/-} mice (A). 25 mg acidic and 7.5 mg neutral GSL from the kidney was applied on the TLC plate. GM2 level was shown in the kidney of 2.5- (B) and 4.5- (C) month-old WT, *Hexa*^{-/-}, *Neu3*^{-/-} and *Hexa*^{-/-}*Neu3*^{-/-} mice. Arrows indicate the positions of the ganglioside standards. Data show mean \pm SEM of measurements. Significant levels of data were determined using the one-way ANOVA (*** p < 0.0001). (n = 2 for 4.5-month-old mice and n = 2 for 2.5-month-old mice)

3.4. Mass Spectrometer Analysis

The brains of 4.5-month-old WT, Hexa^{-/-}, Neu3^{-/-} and Hexa^{-/-}Neu3^{-/-} mice obtained with liquid nitrogen and total ganglioside isolation were performed. The isolated lipids were sent to the mass spectrometry laboratory of Prof. Dr. Roger Sandhoff (Lipid Pathobiochemistry Group, German Cancer Research Center, Heidelberg, Germany) with dry ice. Amount of LacCer, GM3, GM2, GM1, GA2 aThe brains of 4.5-month-old WT, Hexa^{-/-}, Neu3^{-/-} and Hexa^{-/-}Neu3^{-/-} mice obtained with liquid nitrogen and total ganglioside isolation were performed. The isolated lipids were sent to the mass spectrometry laboratory of Prof. Dr. Roger Sandhoff (Lipid Pathobiochemistry Group, German Cancer Research Center, Heidelberg, Germany) with dry ice. Amount of LacCer, GM3, GM2, GM1, GA2, and GA1 in the total brain was quantified by mass spectrometric analysis (Figure 3.8)

According to mass spectrometry analysis of LacCer, GM3, GM2, GM1, GA2, GA1 gangliosides, there was an increase in the LacCer, GM3, GM2, GA2 level in 4.5-month-old Hexa^{-/-}Neu3^{-/-} mice brain compared to age-matched counterparts. Amount of GM2 (Figure 3.8 A), GA2 (Figure 3.8 B), LacCer (Figure 3.8 C) and GM3 (Figure 3.8 D), significantly increased 49.40, 36.61, 3.19 and 2.43, fold, respectively, in Hexa^{-/-}Neu3^{-/-} mice brain compared to WT mice brain (Figure 3.8; Table 3.1). There was an insignificant decrease in the amount of GM1 and GA1 ganglioside as 36% and 16 %, respectively, in Hexa^{-/-}Neu3^{-/-} mice brain compared to WT mice brain (Figure 3.8 E and F). The place of gangliosides which is increased or decreased in 4.5-month-old Hexa^{-/-}Neu3^{-/-} mice brain was shown on the pathway (Figure 3.8 G).

GM2 ganglioside level 11.86 fold increased in Hexa^{-/-} mice and 49.40 fold increased in the Hexa^{-/-}Neu3^{-/-} mice compared to WT mice. GA2 ganglioside level 9.59 fold increased in Hexa^{-/-} mice and 36.61 fold increased in the Hexa^{-/-}Neu3^{-/-} mice compared to WT mice. These results showed that sialidase NEU3 had a function on metabolic bypass by the degradation of GM2 to yield GA2 followed by hydrolysis of the GalNAc moiety by Hex B to yield LacCer. Therefore, in Hexa^{-/-}Neu3^{-/-} mouse GM2 level increase, nearly a 5-fold increase compared to Hexa^{-/-} mouse. The reason for the increase in the GA2 level should result from the activity of other sialidases on the GM2

ganglioside such as Neu4 and Neu1.nd GA1 in the total brain was quantified by mass spectrometric analysis (Figure 3.8).

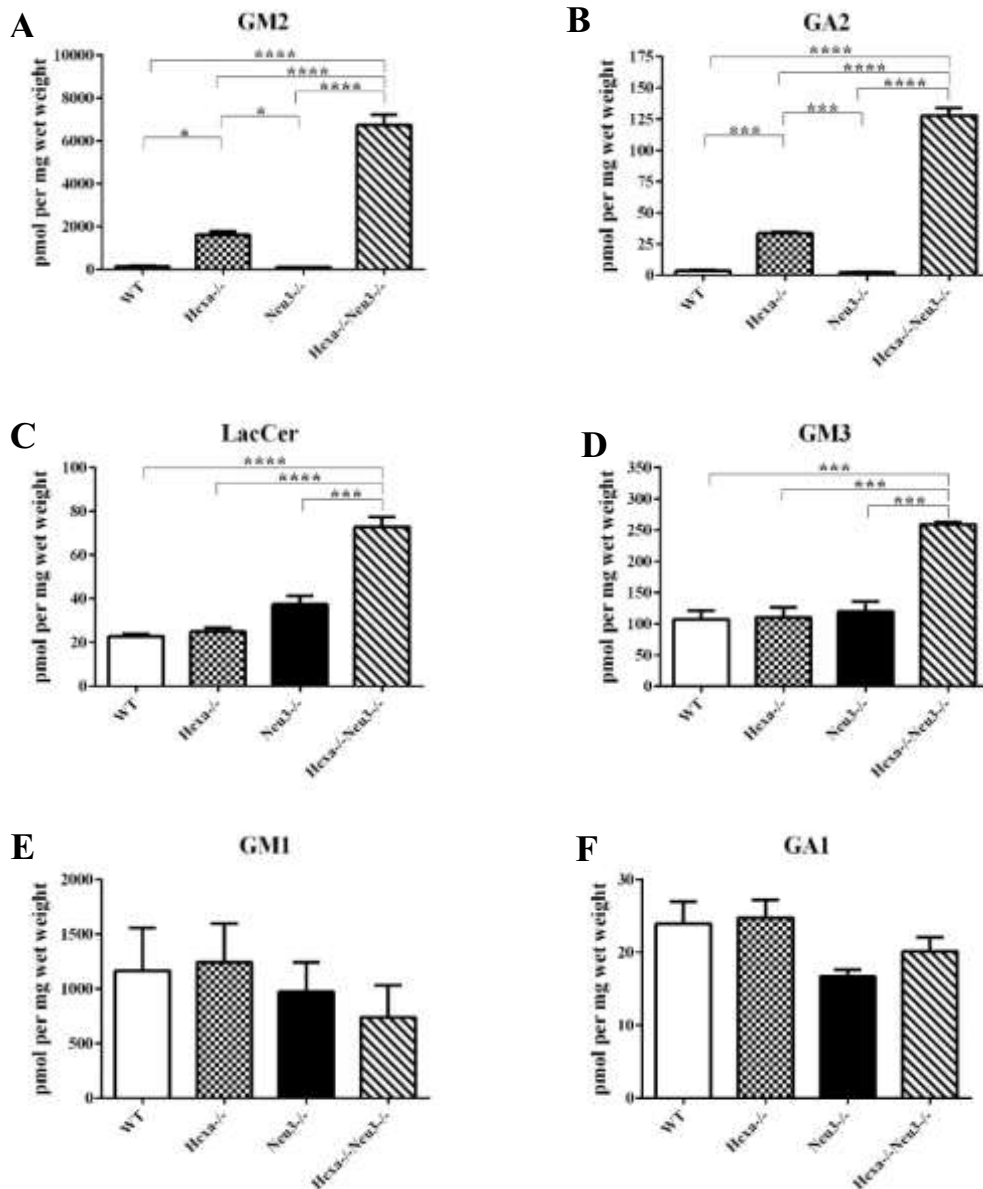


Figure 3.8. Mass spectrometric analysis of GM2 (A), GA2 (B), LacCer (C), GM3 (D), GM1(E) and GA1 (F) in the brain of 4.5-month-old WT, Hexa^{-/-}, Neu3^{-/-} and Hexa^{-/-}Neu3^{-/-} mice. The place of gangliosides which is increased or decreased in 4.5-month-old Hexa^{-/-}Neu3^{-/-} mice brain. Data show mean \pm SEM of measurements. Significant levels of data were determined using the one-way ANOVA (* $p < 0.05$, *** $p < 0.001$ and **** $p < 0.0001$)

3.5. GM2 and Lysosome Staining

To detect the presence of GM2 on lysosomes, 10 μm coronal brain sections from 2.5-month-old mice WT, Hexa^{-/-}, Neu3^{-/-} and Hexa^{-/-}Neu3^{-/-} mice were stained by anti-GM2 antibody and anti-lamp1 antibody. Green signals indicated the presence of GM2, red signals indicated the presence of lysosomes. Lamp1 is lysosome-associated membrane proteins 1. LAMPs are transmembrane proteins with glycosylated luminal domain and a short cytosolic tail and have a function in the maintenance of the structural integrity of the lysosomal membrane (Huynh et al. 2007). Yellow signals indicated the presence of GM2 on lysosomes.

The number of GM2 accumulated neuron cells was significantly increased in Hexa^{-/-}Neu3^{-/-} mice brain regions, including the hippocampus, cortex, thalamus, cerebellum, and pons compared to Hexa^{-/-} mice. No GM2 was detected in WT and Neu3^{-/-} mice.

Abnormal GM2 accumulation was detected in the CA3, CA2 and CA1 hippocampal region of Hexa^{-/-}Neu3^{-/-} (Figure 3.9 A) compared to Hexa^{-/-} mice. There was an approximately 7 fold increase in pyramidal cells of the hippocampal region of Hexa^{-/-}Neu3^{-/-} compared to Hexa^{-/-} mice (Figure 3.9 B).

Approximately 7 fold increase was detected in the primary motor and somatosensory area of the cerebral cortex of Hexa^{-/-}Neu3^{-/-} mice compared to Hexa^{-/-} (Figure 3.10 A, B) mice. GM2 accumulation was also observed in the retrosplenial and secondary motor cortex (data not shown).

Approximately 7.5 fold increase was detected in the thalamus of Hexa^{-/-}Neu3^{-/-} mice compared to Hexa^{-/-} mice (Figure 3.11 A, B).

Abnormal GM2 accumulation was detected in the Purkinje layer and granular layer of Hexa^{-/-}Neu3^{-/-} mice compared to readily detectable levels in the granular layer of Hexa^{-/-} mice. GM2 amount was increased approximately 18 fold in the cerebellum of Hexa^{-/-}Neu3^{-/-} compared to Hexa^{-/-} mice (Figure 3.12 A, B).

Approximately 7.5 fold increase was detected in the pons of Hexa^{-/-}Neu3^{-/-} mice compared to Hexa^{-/-} mice (Figure 3.13 A, B).

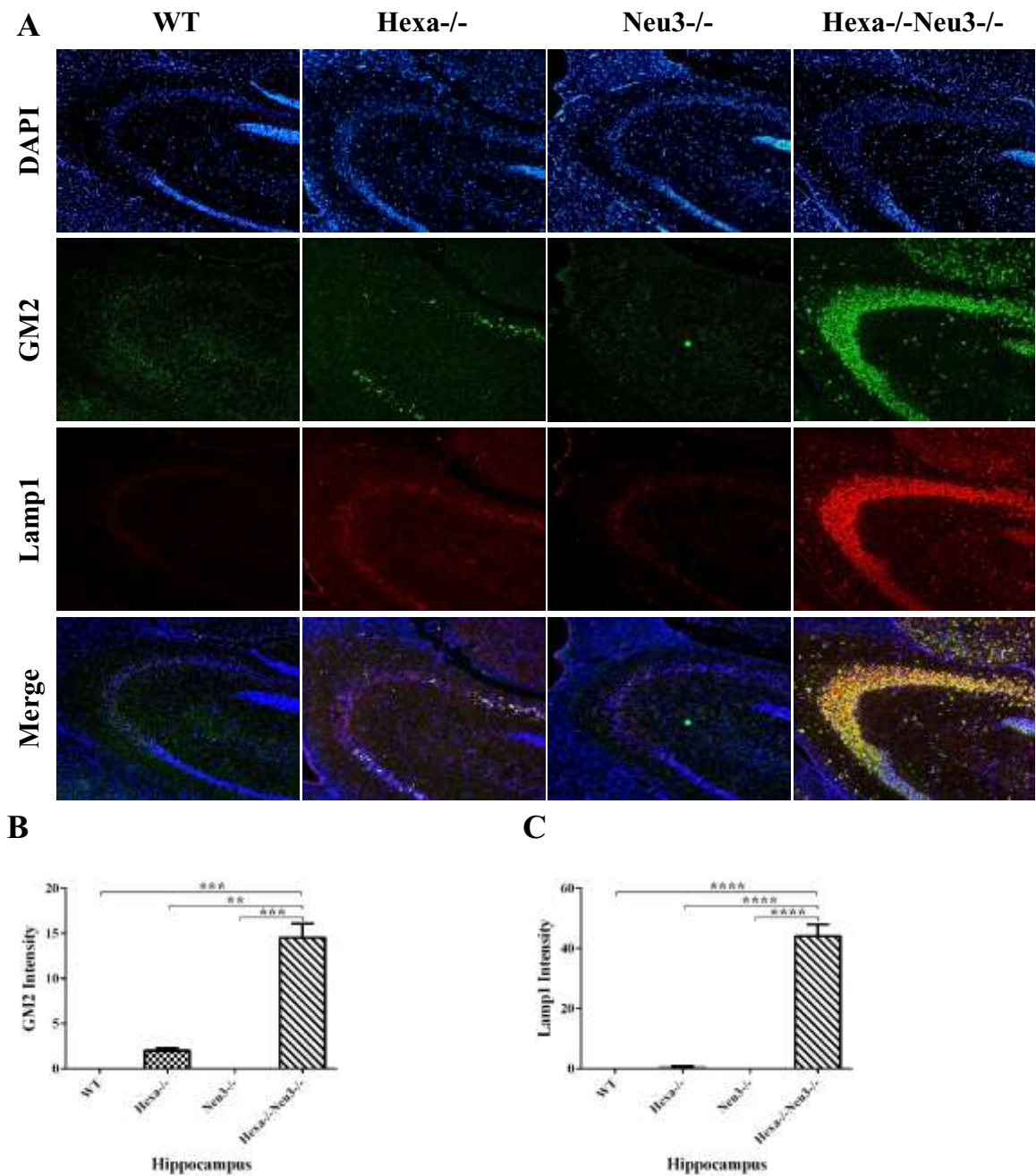


Figure 3.9. Immunohistochemistry to detect the lysosomal storage of GM2 ganglioside in the hippocampus of 4.5-month-old WT, Hexa^{-/-}, Neu3^{-/-} and Hexa^{-/-}Neu3^{-/-} mice. The sections were dual-labeled with anti-GM2 antibody(Green) and anti-LAMP1(Red) antibody. DAPI (Blue) was used to show the position of the nucleus. Yellow signals indicated the presence of GM2 on lysosomes. 10x microscopic images were obtained with the Olympus fluorescence microscope. Histograms show the GM2 (B) and lysosome (C) level. Data show mean ± SEM of measurements. Significant levels of data were determined using the one-way ANOVA (**p<0.025, ***p<0.001 and ****p<0.0001)

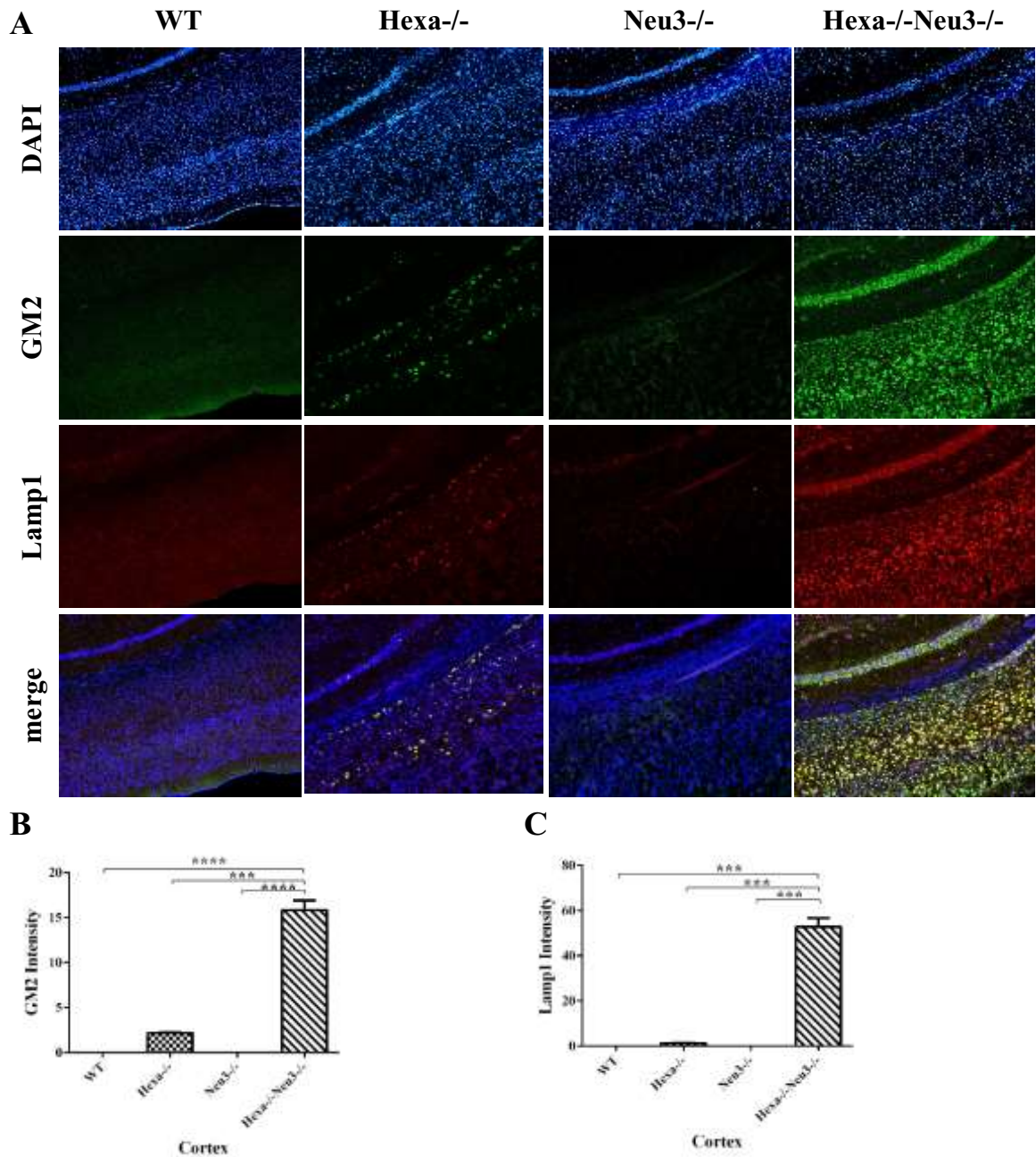


Figure 3.10. Immunohistochemistry to detect the lysosomal storage of GM2 ganglioside in the cortex of 4.5-month-old WT, Hexa^{-/-}, Neu3^{-/-} and Hexa^{-/-}Neu3^{-/-} mice. The sections were dual-labeled with anti-GM2 antibody (Green) and anti-LAMP1(Red) antibody. DAPI (Blue) was used to show the position of the nucleus. Yellow signals indicated the presence of GM2 on lysosomes. 10x microscopic images were obtained with the Olympus fluorescence microscope. Histograms show the GM2 (B) and lysosome (C) level. Data show mean \pm SEM of measurements. Significant levels of data were determined using the one-way ANOVA (** $p < 0.025$, *** $p < 0.001$ and **** $p < 0.0001$)

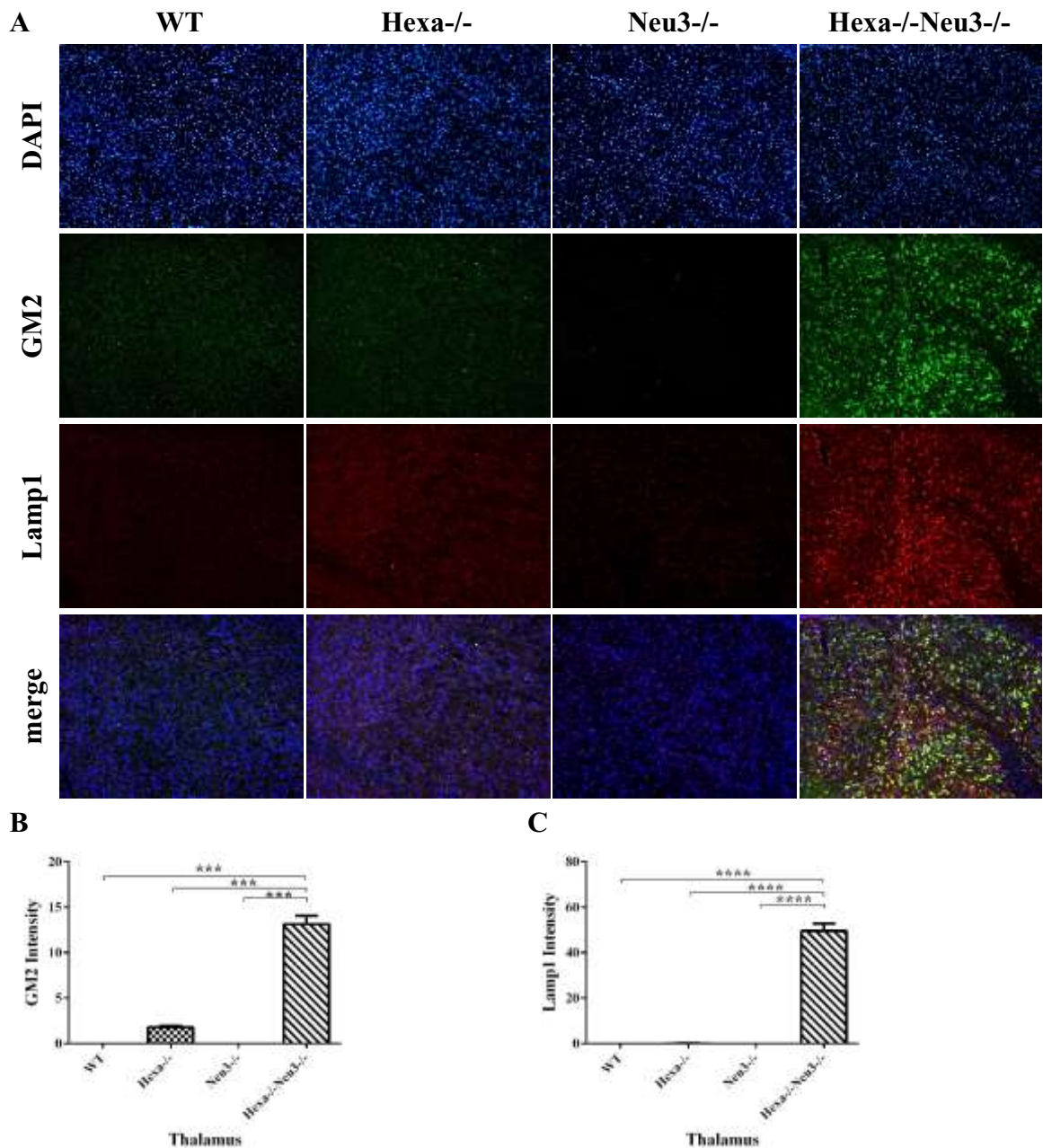


Figure 3.11. Immunohistochemistry to detect the lysosomal storage of GM2 ganglioside in the thalamus of 4.5-month-old WT, Hexa^{-/-}, Neu3^{-/-} and Hexa^{-/-}Neu3^{-/-} mice. The sections were dual-labeled with anti-GM2 antibody (Green) and anti-LAMP1(Red) antibody. DAPI (Blue) was used to show the position of the nucleus. Yellow signals indicated the presence of GM2 on lysosomes. 10x microscopic images were obtained with the Olympus fluorescence microscope. Histograms show the GM2 (B) and lysosome (C) level. Data show mean \pm SEM of measurements. Significant levels of data were determined using the one-way ANOVA (**p<0.025, ***p<0.001 and ****p<0.0001)

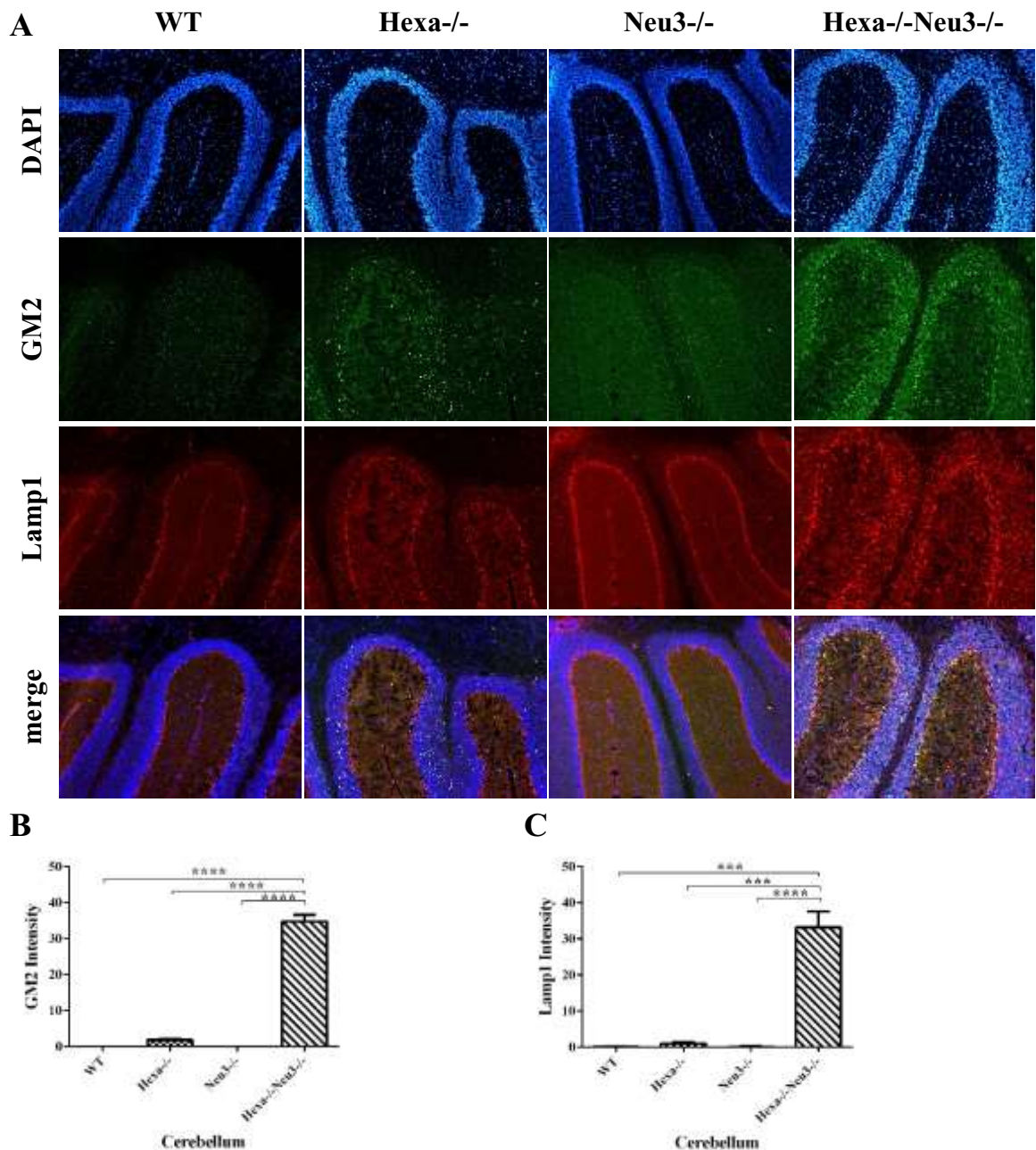


Figure 3.12. Immunohistochemistry to detect the lysosomal storage of GM2 ganglioside in the cerebellum of 4.5-month-old WT, Hexa^{-/-}, Neu3^{-/-} and Hexa^{-/-}Neu3^{-/-} mice. The sections were dual-labeled with anti-GM2 antibody (Green) and anti-LAMP1(Red) antibody. DAPI (Blue) was used to show the position of the nucleus. Yellow signals indicated the presence of GM2 on lysosomes. 10x microscopic images were obtained with the Olympus fluorescence microscope. Histograms show the GM2 (B) and lysosome (C) level. Data show mean \pm SEM of measurements. Significant levels of data were determined using the one-way ANOVA (** $p < 0.025$, *** $p < 0.001$ and **** $p < 0.0001$)

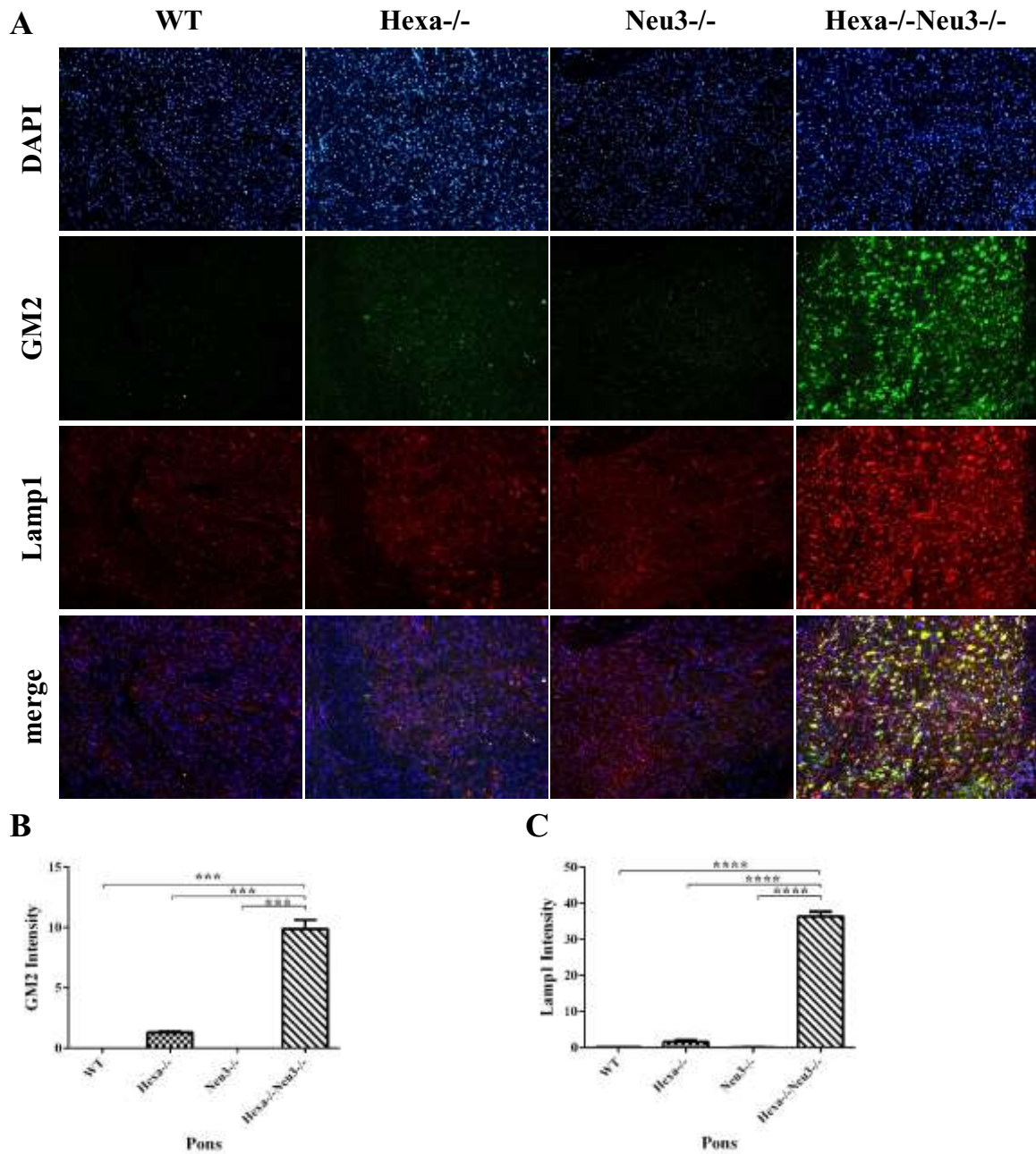


Figure 3.13. Immunohistochemistry to detect the lysosomal storage of GM2 ganglioside in the pons of 4.5-month-old WT, Hexa^{-/-}, Neu3^{-/-} and Hexa^{-/-}Neu3^{-/-} mice. The sections were dual-labeled with anti-GM2 antibody (Green) and anti-LAMP1(Red) antibody. DAPI (Blue) was used to show the position of the nucleus. Yellow signals indicated the presence of GM2 on lysosomes. 10x microscopic images were obtained with the Olympus fluorescence microscope. Histograms show the GM2 (B) and lysosome (C) level. Data show mean \pm SEM of measurements. Significant levels of data were determined using the one-way ANOVA (** $p < 0.025$, *** $p < 0.001$ and **** $p < 0.0001$)

The number of lysosomes accumulated neuronal cells were also significantly increased in Hexa^{-/-}Neu3^{-/-} mice brain regions, including the hippocampus, cortex, thalamus, cerebellum, and pons compared to WT and single-gene knockout aged-matched counterparts. According to intensity analysis by ImageJ software, the presence of lysosomes was much more than the amount of GM2 in the hippocampus (Figure 3.9 C), cortex (Figure 3.9 C), thalamus (Figure 3.9 C), cerebellum (Figure 3.9 C) and pons (Figure 3.9 C). Lysosomal accumulation was detected in both Hexa^{-/-} and Hexa^{-/-}Neu3^{-/-} mice. However, the most severe phenotype was detected in the Hexa^{-/-}Neu3^{-/-} mice brain. The presence of lysosomes was increased as 68 fold in the hippocampus (Figure 3.9 C), 42 fold in the cortex (Figure 3.9 C), 110 fold in the thalamus (Figure 3.9 C), 33 fold in the cerebellum (Figure 3.9 C) and 23 fold in the pons (Figure 3.9 C) of Hexa^{-/-}Neu3^{-/-} mice compared to age-matched Hexa^{-/-} mice.

3.6. Transmission Electron Microscopy

In GM2 gangliosidosis patients and animal models, GM2 ganglioside stored in neurons in the form of concentrically arranged lamellae known as membranous cytoplasmic bodies (MCBs) (Yamanaka et al. 1994; Lawson and Martin 2016).

Electron microscopic analysis of 4.5-month-old Hexa^{-/-}Neu3^{-/-} mice demonstrated an abnormal increase in lysosomes, which is a noticeable morphological marker of neurons that are associated with LSDs. Compared to the WT and single-gene knockout aged-matched counterparts, Hexa^{-/-}Neu3^{-/-} mice had numerous membranous cytoplasmic bodies with concentric ring-like structures similar to those reported in GM2 gangliosidosis patients (Figure 3.14).

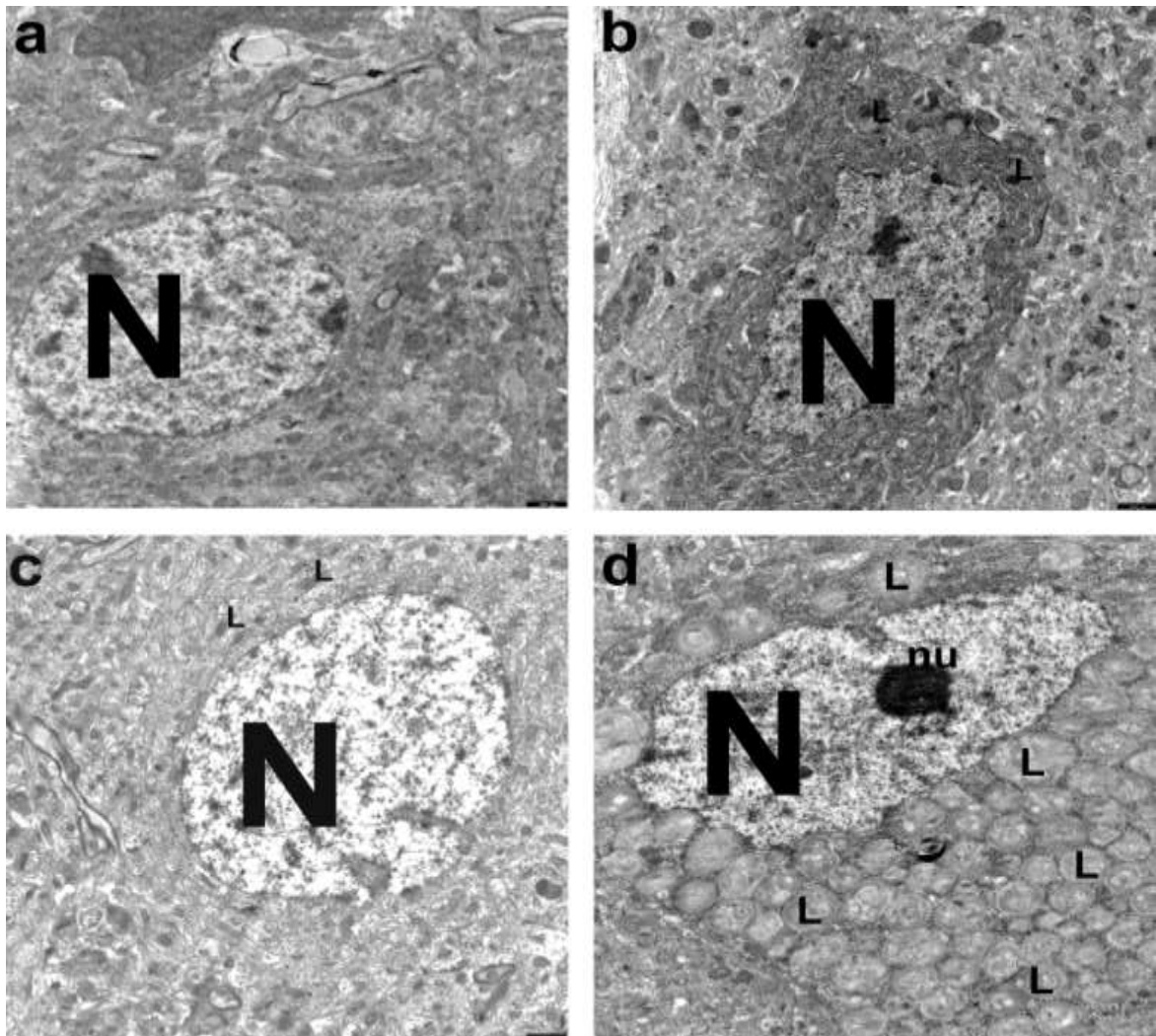


Figure 3.14. Transmission electron micrograph of membranous cytoplasmic bodies in the cortex of WT (A), Hexa^{-/-} (B), Neu3^{-/-} (C) and Hexa^{-/-}Neu3^{-/-} (D) mice. N: nucleus; L: lysosomes; nu: nucleolus

Membranous cytoplasmic bodies in the neuronal lysosomes were observed in the Purkinje cells (Figure 3.15 A), granular cell (Figure 3.15 B) and cerebral neuron (Figure 3.15 C, D), similar to those reported in human Tay-Sachs patients (Figure 3.15 A, D). The inclusions of many small vesicles and complex lamellar structures were also observed in the kidney and testis samples in Hexa^{-/-}Neu3^{-/-} mice (Figure 3.15 E, F).

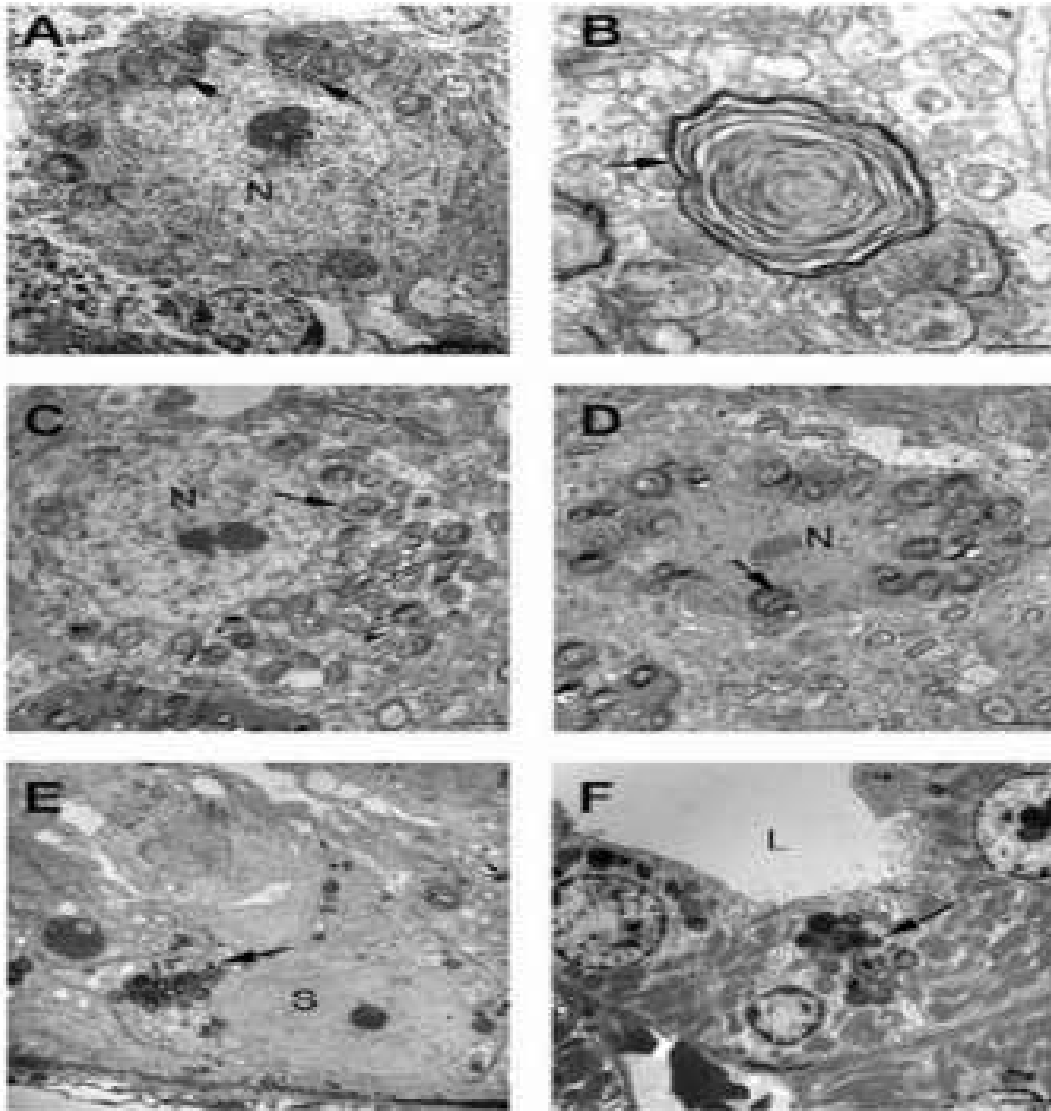


Figure 3.15. Transmission electron micrographs of lysosomal inclusions in cerebellar and cerebral cortex neurons, testis, and kidney tissues from 4.5-month-old Hexa^{-/-}Neu3^{-/-} mice. Representative cerebellar tissue micrographs (A, B). Purkinje cells exhibit numerous cytoplasmic inclusions (A). At high magnification, a granular cell shows cytoplasmic inclusions with lamellar membrane structure (B). Representative cerebral tissue micrographs (C, D). Neurons exhibit numerous cytoplasmic inclusions (C). A possible degenerating neuron shows cytoplasmic inclusions (D). Representative testis tissue micrograph. Cytoplasmic inclusions were observed in the Sertoli cell (E). Representative renal tissue micrograph. A renal tubule cell near the lumen (L) shows numerous cytoplasmic inclusions (F). These data are representative of two samples. Cytoplasmic inclusions were indicated with an arrow. N, nucleus of the Purkinje cell or neuron. S, Sertoli cell nucleus. L, Lumen of renal tissues. Scale bars: A, 5 μ m; B, 500 nm; C, 2 μ m; D, 2 μ m; E, 5 μ m; F, 2 μ m

3.7. May-Grunwald Giemsa Staining

Total blood was obtained from 4.5-month-old WT, Hexa^{-/-}, Neu3^{-/-} and Hexa^{-/-}Neu3^{-/-} mice tail to detect the presence of lysosomes on lymphocytes and monocytes cells (Tamura et al. 2010). The vacuolated monocytes were also observed in the peripheral blood of 4.5-month-old Hexa^{-/-}Neu3^{-/-} mice as GM2 gangliosidosis patients (Figure 3.16 D).

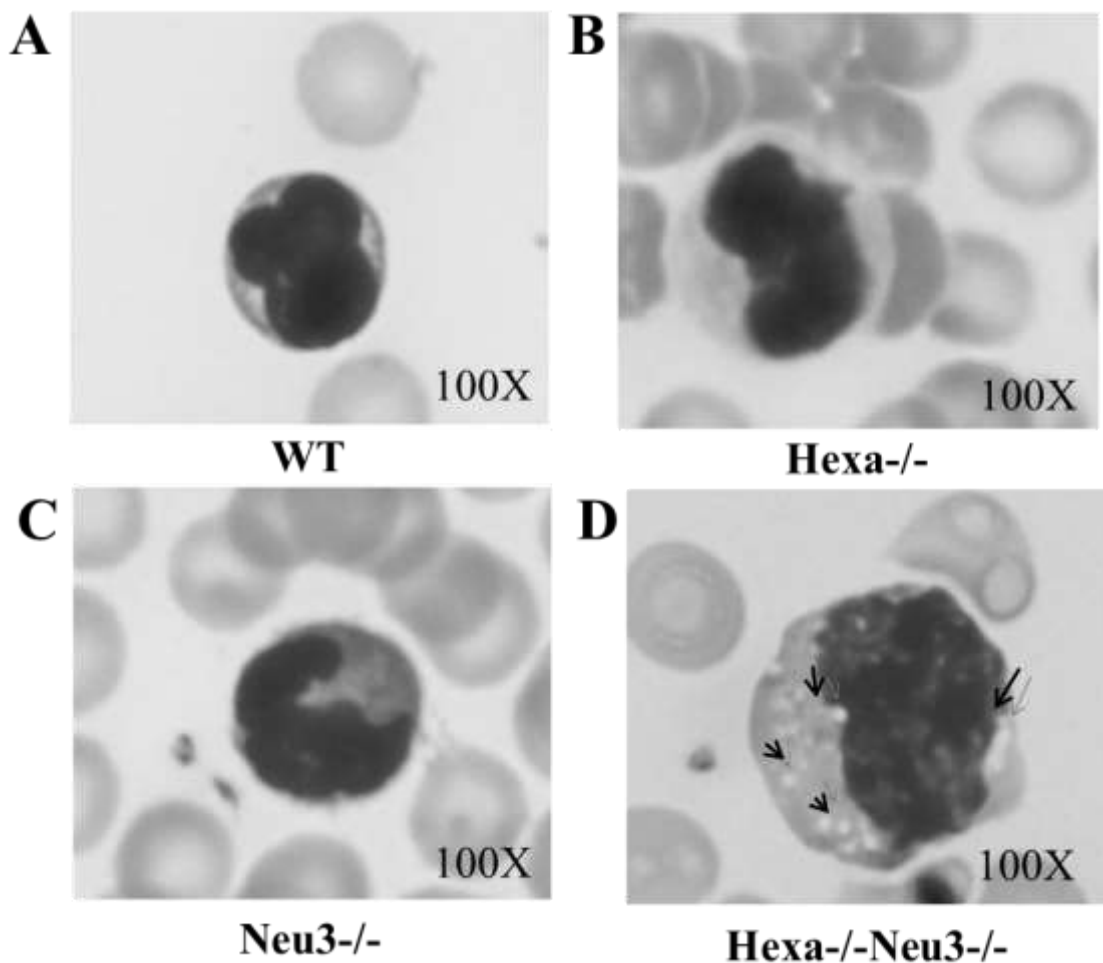


Figure 3.16. Blood smear analysis of 4.5-month-old mice to detect lysosomal accumulation on monocytes. 100x microscopic images were obtained from WT, Hexa^{-/-}, Neu3^{-/-} and Hexa^{-/-}Neu3^{-/-} mice blood with the Olympus light microscope

3.8. Enzyme Activity Assay

The specific activity of Neuraminidase 1, β -Hexosaminidase B, β -Galactosidase, β -Glucosidase, and α -L-Iduronidase enzymes was measured in the brain of 2.5 and 4.5-month-old WT, Hexa^{-/-}, Neu3^{-/-} and Hexa^{-/-}Neu3^{-/-} to see the effect of Neu3 deficiency on Tay-Sachs mouse model.

β -Galactosidase catalyzes the hydrolysis of β -galactosides into monosaccharides by the breaking of a glycosidic bond that removes galactose from ganglioside GA1, GM1, lactosylceramides (Kolter 2012). There was genotype depended on an increase in the activity of β -Galactosidases. The β -Galactosidases activity was decreased in 4.5-month-old mice compared to 2.5-month-old mice as WT (0,6 fold), Hexa^{-/-} (0.9 fold). It was increased in 4.5-month-old mice compared to 2.5-month-old mice as Neu3^{-/-} (1.2 fold) and Hexa^{-/-}Neu3^{-/-} (1,7 fold) (Figure 3.17 A).

β β -Glucosidase catalyzes the hydrolysis of the glycosidic bonds from glycoconjugates with the release of glucose. In the ganglioside degradation pathway, it has function on the cleavage of glucose from glucosylceramide to produce ceramide (Kolter 2012). β -Glucosidase level increase 1.5 fold only in the 4.5-month-old Hexa^{-/-}Neu3^{-/-} mice compared to 2.5-month-old Hexa^{-/-}Neu3^{-/-} mice. (Figure 3.17 B).

β -Hexosaminidase B ($\beta\beta$) predominantly cleaves uncharged substrates such as GA2 and oligosaccharides with terminal N-acetyl-hexosamine (N-acetyl-galactose amine) residues (Kolter 2012). There was both age and genotype depended increase in the activity of β -Hexosaminidase B. Enzymatic activity increased in 4.5-month-old mice compared to 2.5-month-old mice as WT (1.3 fold), Hexa^{-/-} (1.9 fold), Neu3^{-/-} (1.9 fold) and Hexa^{-/-}Neu3^{-/-} (3 fold) (Figure 3.17 C).

Neuraminidase 1 forms a lysosomal multienzyme complex with protective protein/cathepsin A (PPCA) and β -galactosidase. It was showed that Neu1 mostly active toward sialyloligosaccharides and sialylglycoproteins but it can also hydrolyze some ganglioside such as GM3 and GD1a and has weak activity toward GM2. Moreover, GM3 and GD3 ganglioside storage were recognized in the visceral tissues of sialidosis patients (Seyrantepe, Iannello, et al. 2010). There was both age- and genotype-depended increase in the activity of Neuraminidase 1. Enzymatic activity increased in 4.5-month-

old mice compared to 2.5-month-old mice as WT (1.5 fold), Hexa^{-/-} (1.2 fold), Neu3^{-/-} (2.4 fold) and Hexa^{-/-}Neu3^{-/-} (4.6 fold) (Figure 3.17 D).

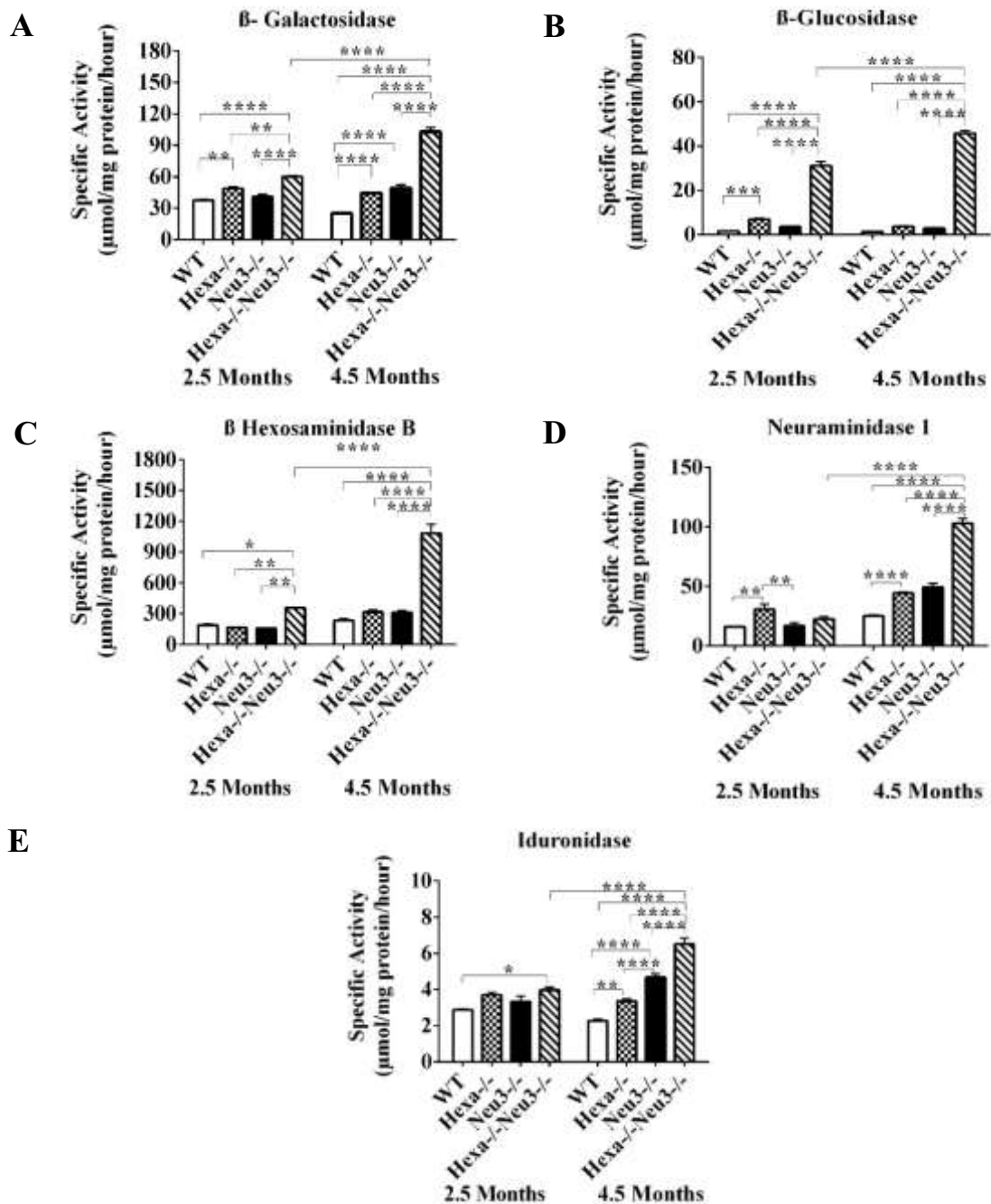


Figure 3.17. The levels of β -Galactosidase (A), β -Glucosidase (B), β -Hexosaminidase B (C), Neuraminidase 1 (D) and Iduronidase (E) in the brain of 2.5 and 4.5-month-old WT, Hexa^{-/-}, Neu3^{-/-} and Hexa^{-/-}Neu3^{-/-} mice. Data show mean \pm SEM of measurements in three mice. Significant levels of data were determined using the two-way ANOVA (* p <0.05, ** p <0.025, *** p <0.001 and **** p <0.0001)

α -L-iduronidase has a function in the degradation pathway of glycosaminoglycans (GAGs), especially two particular GAGs, heparan, and dermatan sulfate. Mucopolysaccharidosis type I (MPS I), an autosomal recessive disease classified as lysosomal storage disorder, is caused by the total or partial deficiency of a lysosomal hydrolase, α -L-iduronidase (IDUA). The absence or the reduced amount of this enzyme leads to the storage of these GAGs in the cell (Kreutz et al. 2013). Although α -L-iduronidase does not have a function on the ganglioside degradation pathway, the α -L-iduronidase level increased genotype depended on the 4.5-month-old mice. Compared to WT mice, the α -L-iduronidase level increased 1.4 fold in Hexa^{-/-} mice, 2 fold Neu3^{-/-} mice and 2.8 fold Hexa^{-/-}Neu3^{-/-} mice brain (Figure 3.17 E).

3.9. Effects of GM2 Accumulation to CNS

3.9.1. Hematoxylin and Eosin Staining

10 μ m coronal brain sections from the cerebral cortex and cerebellum of 4.5-month-old WT, Hexa^{-/-}, Neu3^{-/-} and Hexa^{-/-}Neu3^{-/-} mice were stained with Hematoxylin–Eosin to detect tissue morphology (Wada et al. 2000).

Histological evaluation of the Hexa^{-/-}Neu3^{-/-} mice brain revealed that GM2 storage leads to striking vacuolization found in the cerebral cortex (Figure 3.18 D). The 40X microscopic images straightforwardly emphasized this situation. Vacuolization was not detected WT, Hexa^{-/-}, Neu3^{-/-}-mice brain (Figure 3.18).

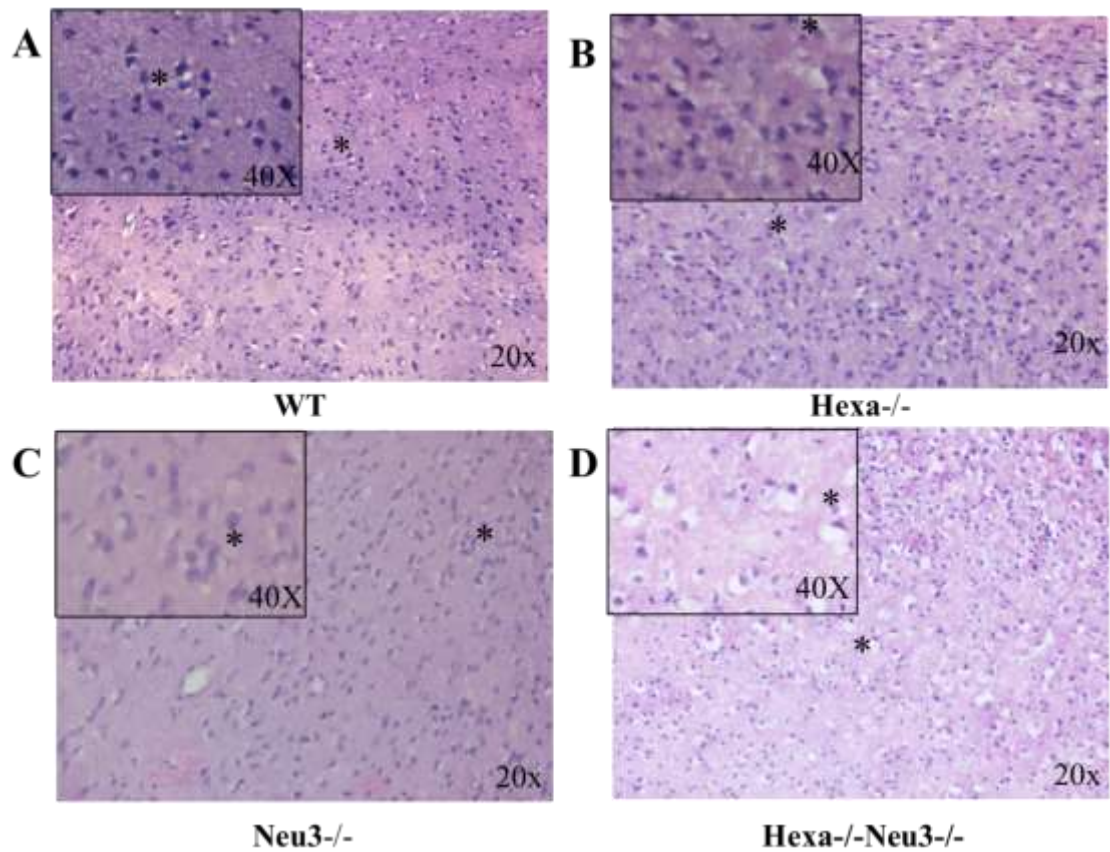


Figure 3.18. Neuropathology in the cortex of 4.5-month-old Hexa^{-/-}Neu3^{-/-} mice compared with WT, Hexa^{-/-} and Neu3^{-/-} mice with Hematoxylin–Eosin staining. 20x and 40X microscopic images were obtained with the Olympus light microscope

Purkinje cells in the cerebellum were significantly affected in the Hexa^{-/-}Neu3^{-/-} mice compared to the WT and single-gene knockout aged-matched counterparts. The 40X microscopic images have specified this situation. While 4.5-month-old WT, Hexa^{-/-} and Neu3^{-/-} mice had the normal Purkinje cell layer, Hexa^{-/-}Neu3^{-/-} mice had defected Purkinje layer (Figure 3.19).

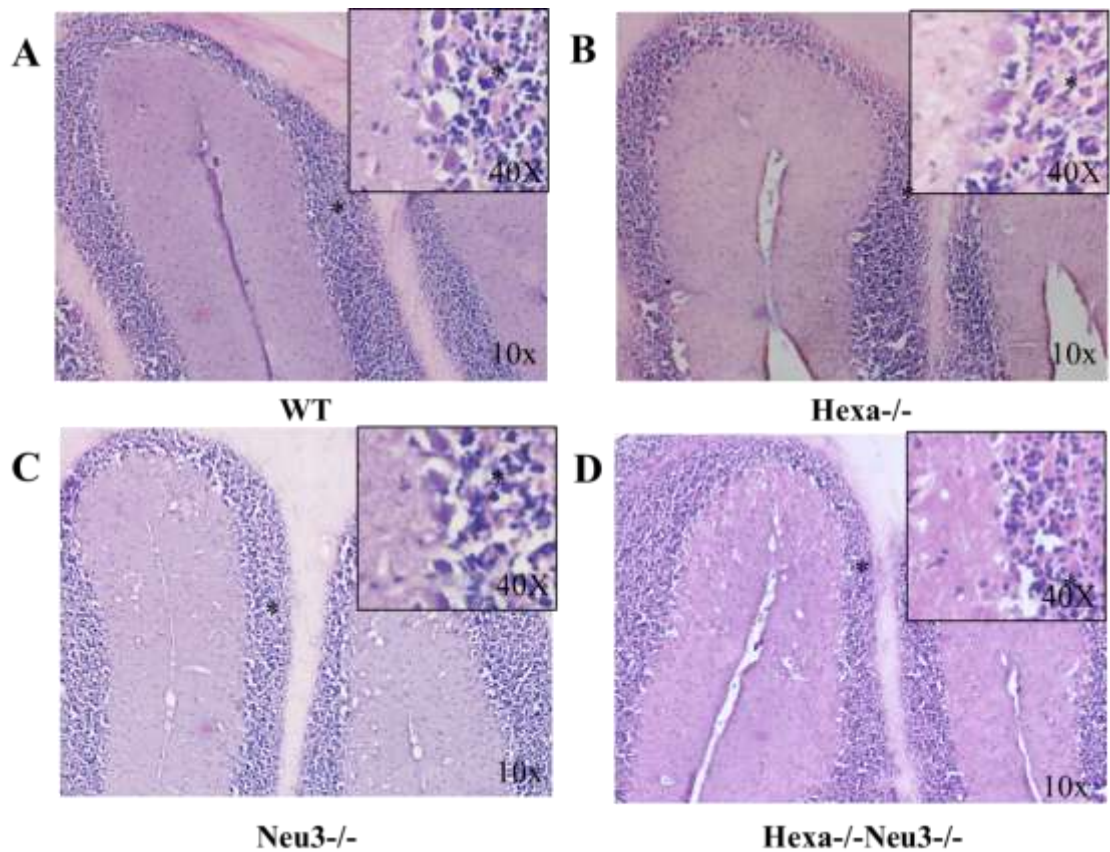


Figure 3.19. Neuropathology in the cerebellum of 4.5-month-old Hexa^{-/-}Neu3^{-/-} mice compared with WT, Hexa^{-/-} and Neu3^{-/-} mice with Hematoxylin–Eosin staining. 10x and 40X microscopic images were obtained with the Olympus light microscope

3.9.2. Neuronal Death

To detect how the mechanism of apoptosis was affected by the increase in GM2 gangliosides and neuroinflammation in Hexa^{-/-}Neu3^{-/-} mice brain region. Terminal deoxynucleotidyl transferase (TdT) dUTP nick-end labeling (TUNEL) assays (Millipore - ApopTag® Fluorescein In Situ Apoptosis Detection Kit) was used to detect apoptosis. According to the manufacturer of the ApopTag® Fluorescein In Situ Apoptosis Detection Kit, via the kit, the DNA strand breaks are detected by enzymatically labeling the free 3'-OH termini with modified nucleotides. Due to the DNA fragmentation, new DNA ends that are generated in morphologically identifiable nuclei and apoptotic bodies. However,

normal or proliferative nuclei, which have relatively insignificant numbers of DNA 3'-OH ends, usually do not stain during the experiment. Both single-stranded and double-stranded breaks associated with apoptosis are detected.

It was shown that there were elevated levels of cell death in the hippocampus of Hexa^{-/-}Neu3^{-/-} mice compared to the WT, Hexa^{-/-}, Neu3^{-/-} mice. Green signals were the indicator of apoptosis. Nuclei were stained with Propidium iodide. It stains the nucleus red. Green signals come from the nucleus of the apoptotic cells. TUNEL positive neurons were observed as yellow. It was shown that there were elevated levels of cell death in the hippocampus and cerebellum of Hexa^{-/-}Neu3^{-/-} mice compared to the WT, Hexa^{-/-}, Neu3^{-/-} mice (Figure 3.20). It was 9.1 fold in the hippocampus (Figure 3.20 B) and 2.7 fold in the cerebellum (Figure 3.20 C) of Hexa^{-/-}Neu3^{-/-} mice compared to the age-matched WT mice.

To characterize the number of neuron cells, 10 µm coronal brain sections from 2.5- and 4.5-month-old WT, Hexa^{-/-}, Neu3^{-/-} and Hexa^{-/-}Neu3^{-/-} mice were immunostained with the anti-NeuN antibody, which recognizes neurons.

There was no significant change in the neuron number of 2.5-month-old Hexa^{-/-}Neu3^{-/-} mice compared to age-matched control groups in different regions of the central nervous system. Loss of NeuN immunoreactivity could be explained by neuronal death in the damaged area of the brain (Gusel'nikova and Korzhevskiy 2015). Although there was neuroinflammation in the 2.5-month-old Hexa^{-/-}Neu3^{-/-} mice, there was no loss in neurons (Figure 3.21).

4.5-month-old Hexa^{-/-}Neu3^{-/-} mice showed a loss in neuronal density compared to age-matched control groups in different regions of the central nervous system. It was demonstrated that the number of NeuN-positive neurons was significantly reduced in the cortex as approximately 50% (Figure 3.22 R), in the thalamus as approximately 40% (Figure 3.22 S), and pons as approximately 50% (Figure 3.22 U) in Hexa^{-/-}Neu3^{-/-} mice compared to WT mice. In the granular layer of the cerebellum, there was no significant change in terms of neuronal density (Figure 3.22 T). Thus, the decrease in NeuN immunostaining is correlated with the increase in the number of apoptotic cells.

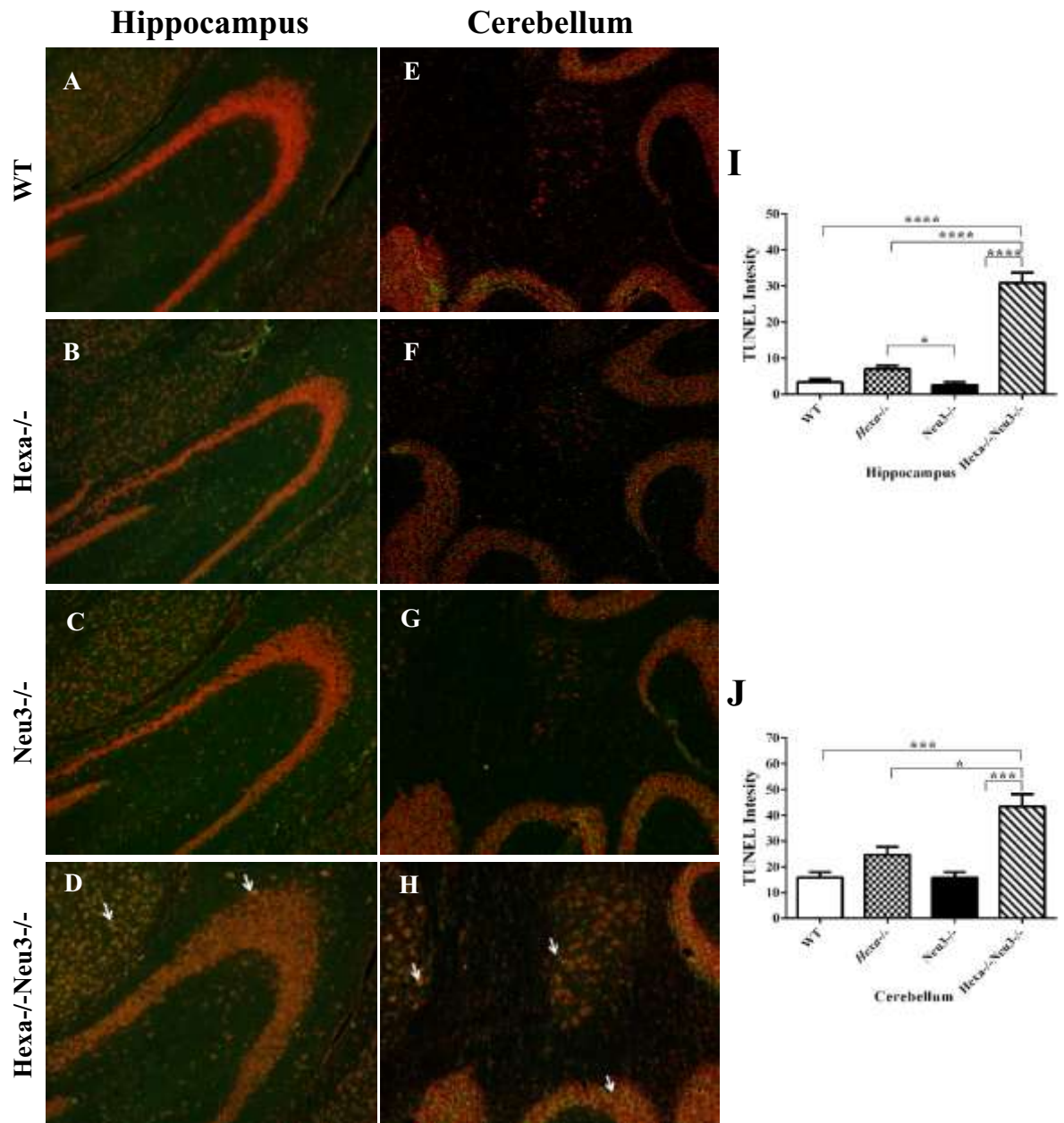


Figure 3.20. The TUNEL assay for 4.5-month-old mice. The sections from the hippocampus (A, B, C, and D, respectively) and cerebellum (E, F, G, and H, respectively) of WT, Hexa^{-/-}, Neu3^{-/-} and Hexa^{-/-}Neu3^{-/-} mice were stained with Terminal deoxynucleotidyl transferase (TdT) as green. Nuclei are counterstained with Propidium iodide (PI) in red. TUNEL positive neurons were observed as yellow. Quantification of apoptosis was determined with colog2 on image for the hippocampus (I), cerebellum (J). The data are represented as the mean ± SEM. One-way ANOVA was used for statistical analysis. (*p<0.05, ***p<0.01 and ****p<0.001)

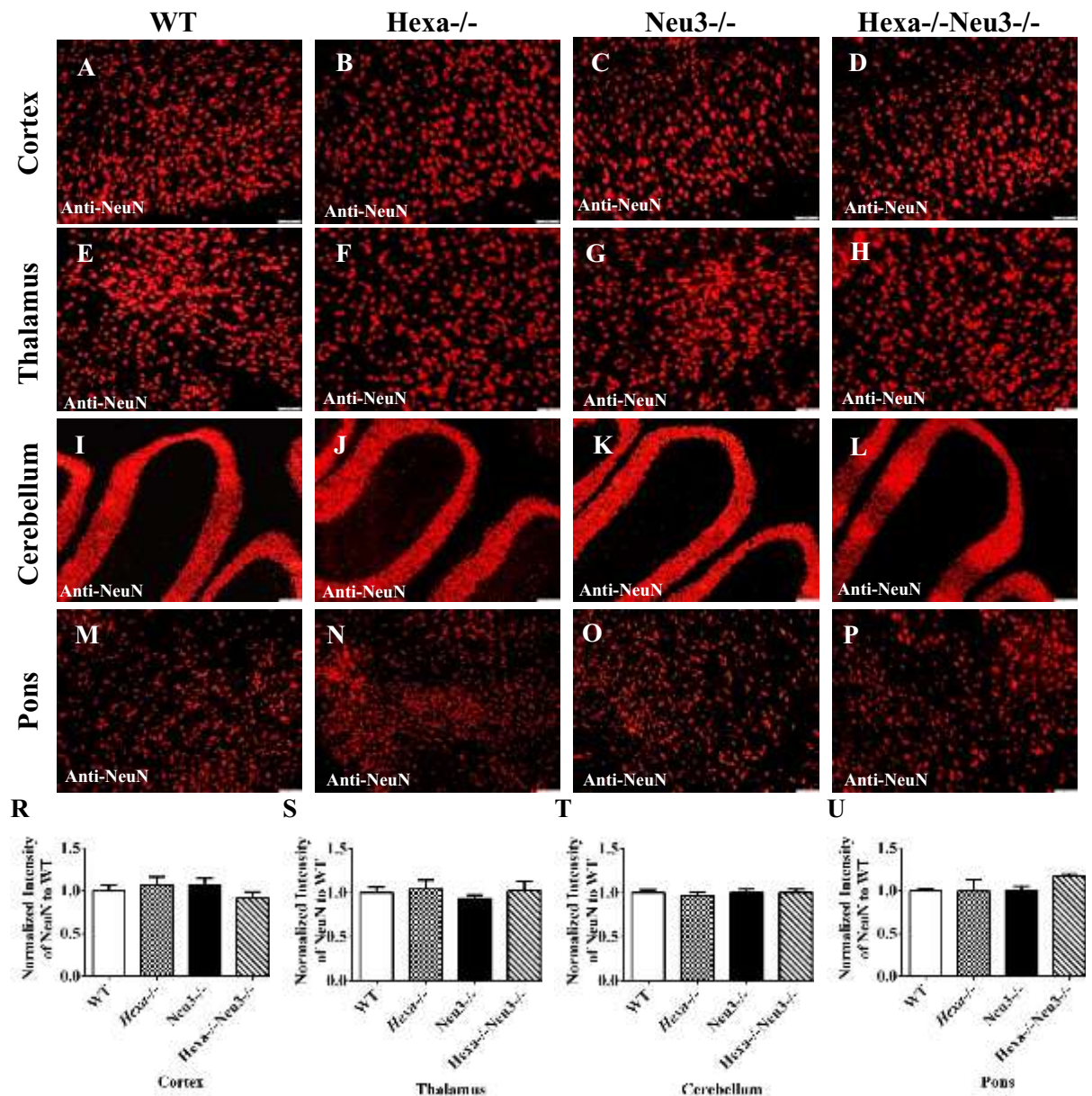


Figure 3.21. The neuron number of 2.5-month-old mice. The sections from cortex (A, B, C, and D, respectively), thalamus (E, F, G, and H, respectively), cerebellum (I, J, K, and L, respectively) and pons (M, N, O and P, respectively) of WT, Hexa^{-/-}, Neu3^{-/-} and Hexa^{-/-}Neu3^{-/-} mice were stained with anti-NeuN antibody (red; neuronal marker). Histograms show the quantification of neuronal density for cortex (R), thalamus (S), cerebellum (T) pons (U). Scale bar 50 μ m for cortex and thalamus. Scale bar 100 μ m for cerebellum and pons. The data are represented as the mean \pm SEM. One-way ANOVA was used for statistical analysis

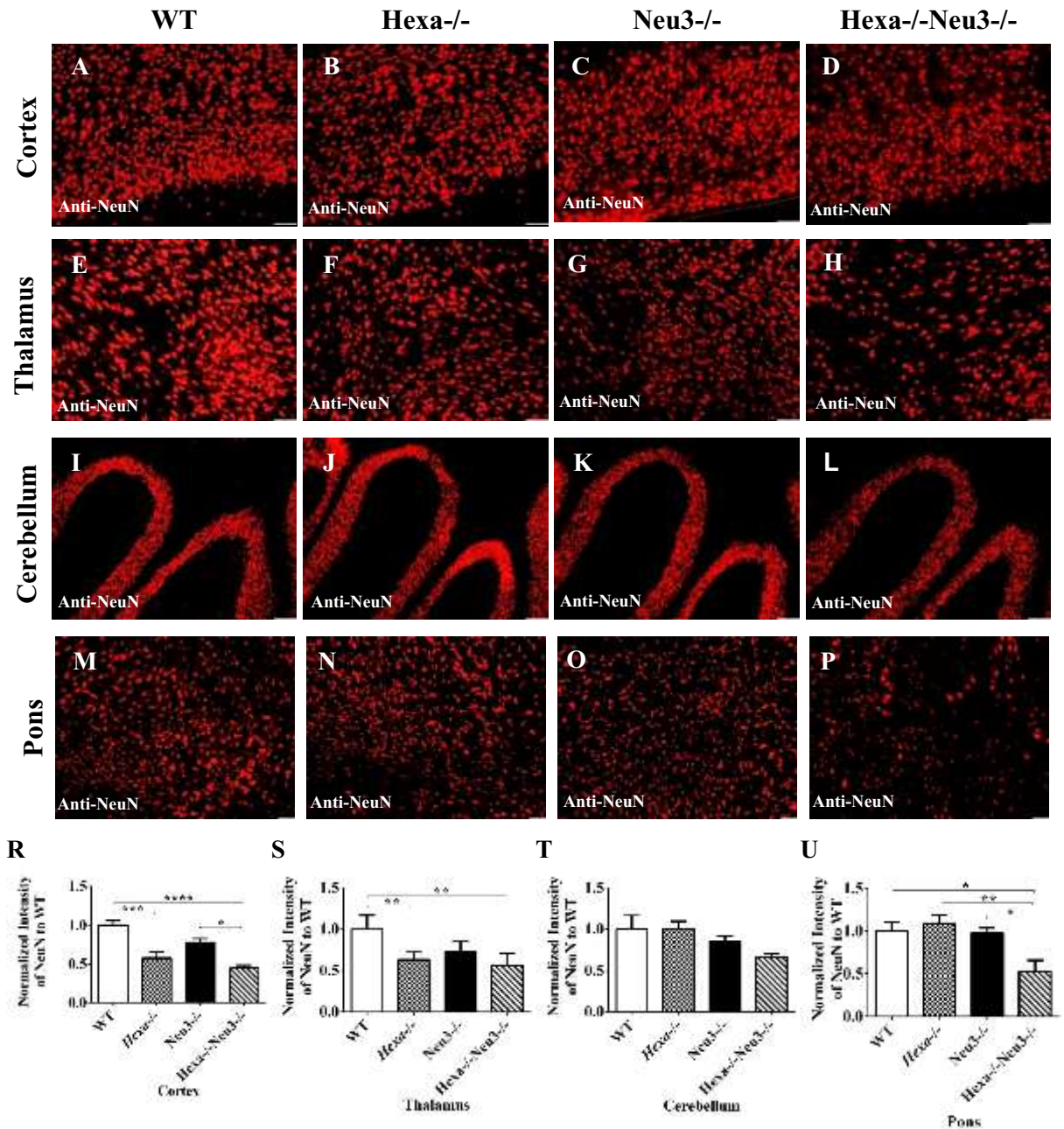


Figure 3.22. The neuron number of 4.5-month-old mice. The sections from cortex (A, B, C, and D, respectively), thalamus (E, F, G, and H, respectively), cerebellum (I, J, K, and L, respectively) and pons (M, N, O and P, respectively) of WT, Hexa^{-/-}, Neu3^{-/-} and Hexa^{-/-}Neu3^{-/-} mice were stained with anti-NeuN antibody (red; neuronal marker). Histograms show the quantification of neuronal density for cortex (R), thalamus (S), cerebellum (T) pons (U). Scale bar 50 μ m for cortex and thalamus. Scale bar 100 μ m for cerebellum and pons. The data are represented as the mean \pm SEM. One-way ANOVA was used for statistical analysis. (* $p < 0.05$, ** $p < 0.025$, *** $p < 0.01$ and **** $p < 0.001$)

3.9.3. Astrocyte Analysis

Activated astrocytes undergo a morphological change as an increase in intermediate filament expressions like glial fibrillary acidic protein (GFAP) and vimentin. To visualize the location of astrocytes and presence of astrogliosis, 10 μm brain sections from WT, Hexa^{-/-}, Neu3^{-/-} and Hexa^{-/-}Neu3^{-/-} mice were labeled with the anti-GFAP antibody.

Glial fibrillary acidic protein (GFAP) immunohistochemistry revealed strong astrogliosis in the hippocampus, cortex, and cerebellum of both 2.5 and 4.5-month-old Hexa^{-/-}Neu3^{-/-} mice compared to age-matched counterparts similar to Tay-Sachs and Sandhoff patients (Figure 3.23 and 3.24).

3.9.4. Oligodendrocyte Analysis

To characterize how neuroinflammation affected oligodendrocytes, 10 μm coronal brain sections from 2.5- and 4.5-month-old WT, Hexa^{-/-}, Neu3^{-/-} and Hexa^{-/-}Neu3^{-/-} mice at were immunostained with the CNPase antibody, which recognizes oligodendrocytes.

There was no significant change in the oligodendrocytes cell number of 2.5-month-old Hexa^{-/-}Neu3^{-/-} mice compared to age-matched control groups (Figure 3.25).

4.5-month-old Hexa^{-/-}Neu3^{-/-} mice showed a loss in the number of CNPase positive cells compared to age-matched WT, Hexa^{-/-} and Neu3^{-/-} mice. The oligodendrocytes cell number was significantly reduced in cortex as approximately 45%, in thalamus and cerebellum as approximately 55%, and pons as approximately 35% in Hexa^{-/-}Neu3^{-/-} mice (Figure 3.26 D, H, L, and P, respectively) compared to WT mice (Figure 3.26 A, E, I and M, respectively). The oligodendrocyte cell number was approximately 30% loss in the cortex of Hexa^{-/-} mice compared to WT mice. In the thalamus, cerebellum, and pons there were no significant changes in the oligodendrocytes

cell number of Hexa^{-/-} (Figure 3.26 F, J, and N, respectively) and Neu3^{-/-} (Figure 3.26 G, K, and O, respectively) mice compared the WT mice.

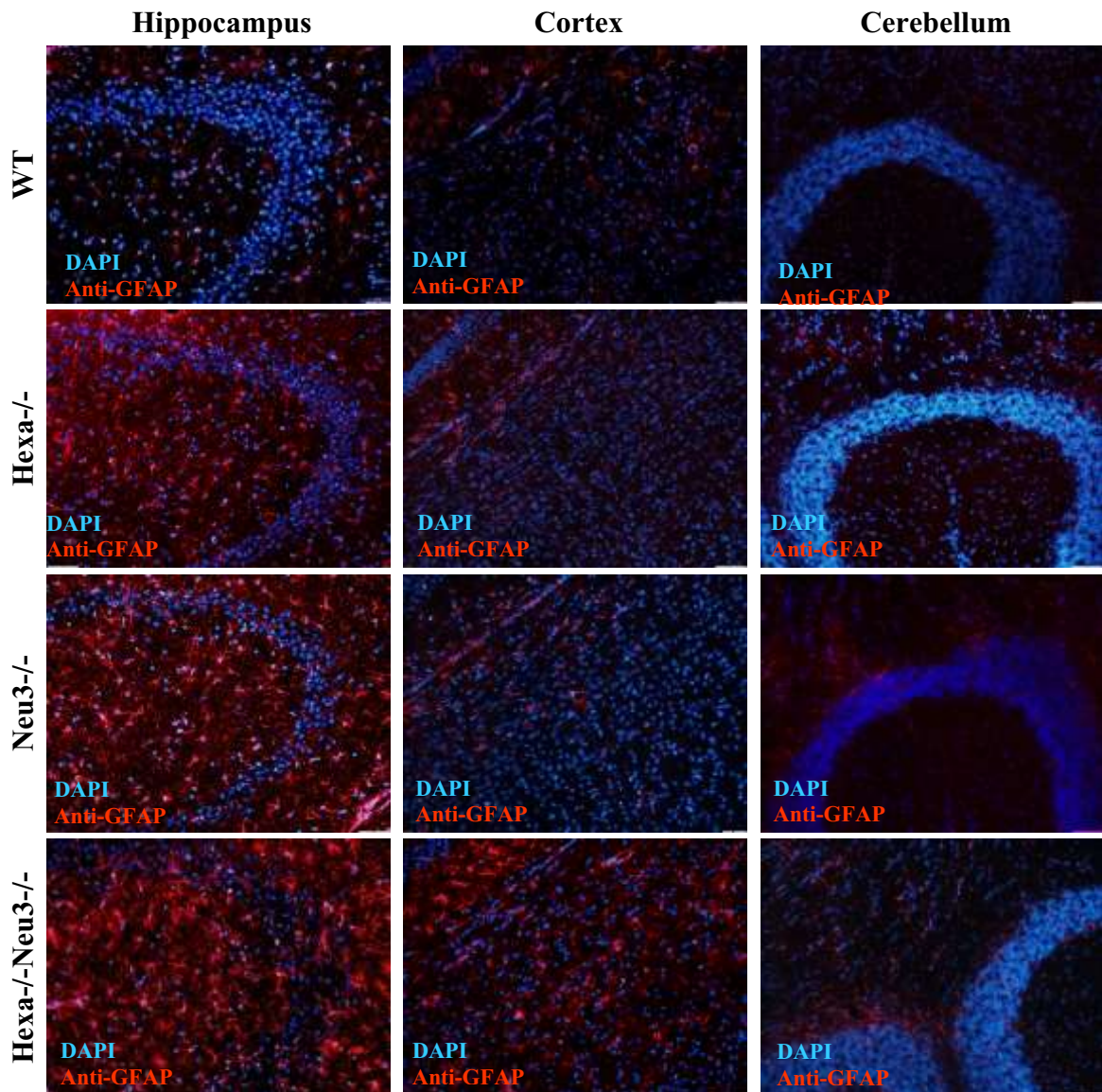


Figure 3.23. Detection of astrocytes in 2.5-month-old mice. The sections from hippocampus, cortex, and cerebellum of WT, Hexa^{-/-}, Neu3^{-/-} and Hexa^{-/-}Neu3^{-/-} mice were stained with anti-GFAP antibody (red) and DAPI (blue; nucleus)

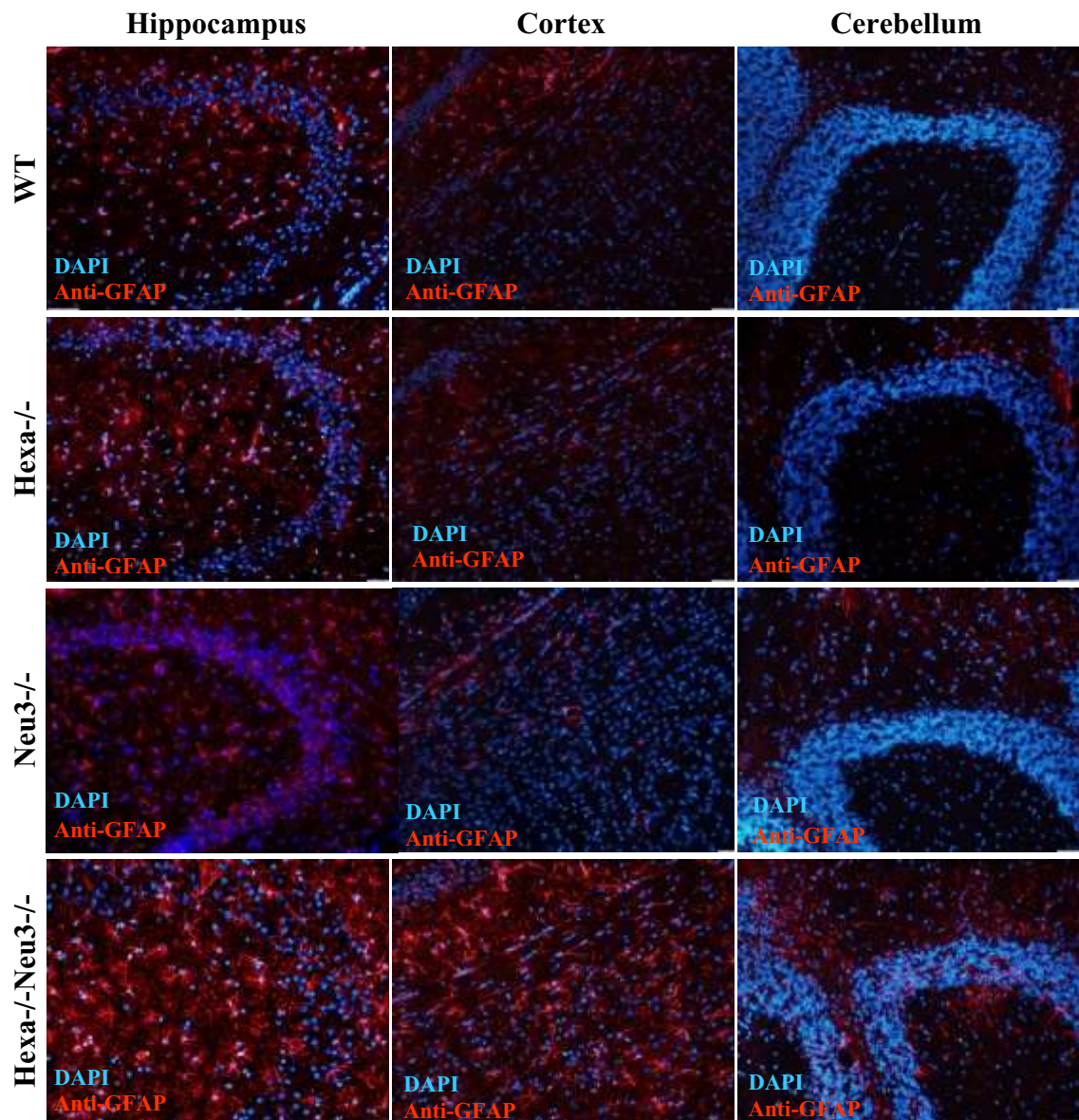


Figure 3.24. Detection of astrocytes in 4.5-month-old mice. The sections from hippocampus, cortex, and cerebellum of WT, Hexa^{-/-}, Neu3^{-/-} and Hexa^{-/-}Neu3^{-/-} mice were stained with anti-GFAP antibody (red) and DAPI (blue; nucleus)

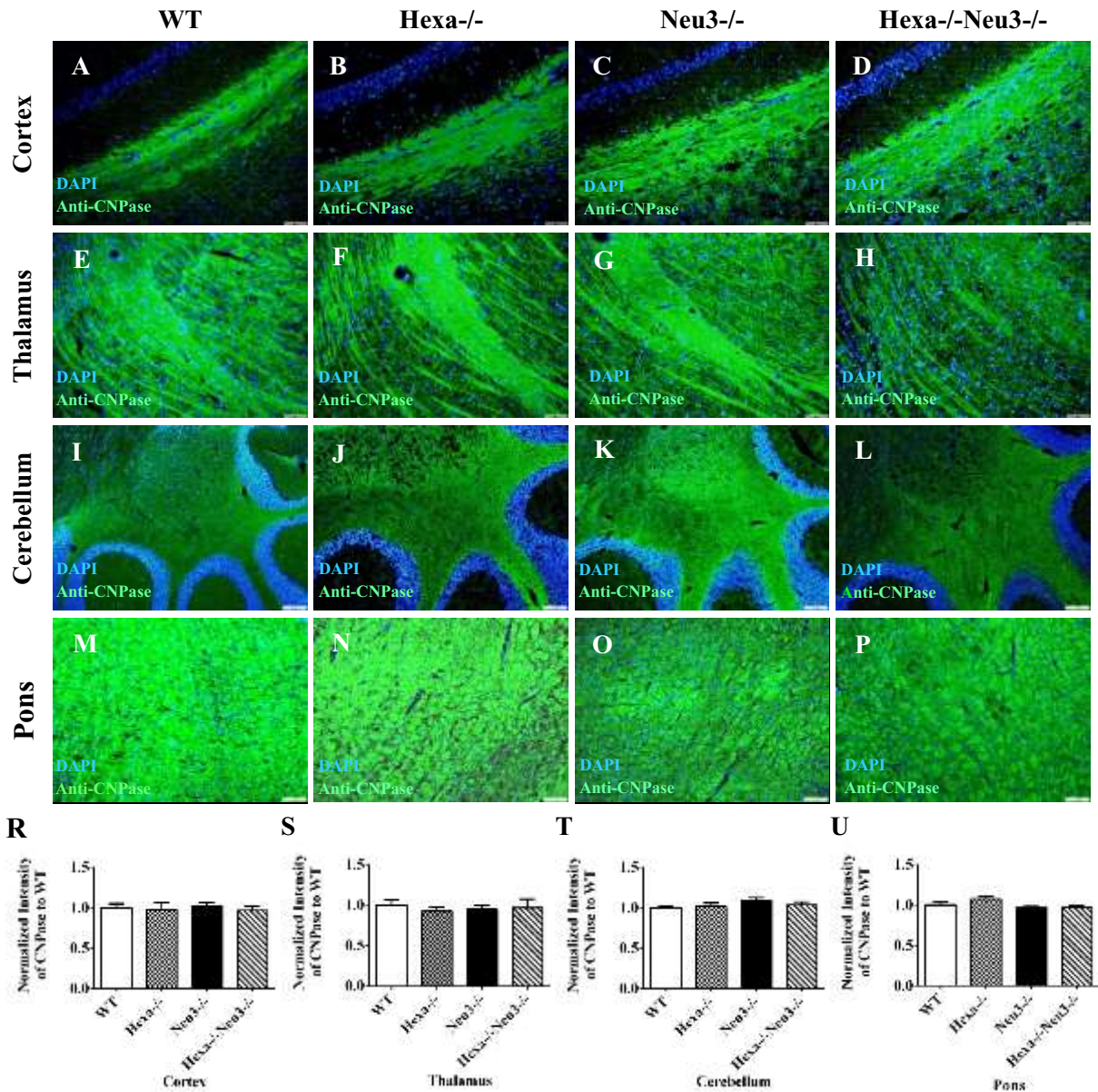


Figure 3.25. Detection of oligodendrocytes number in 2.5-month-old mice. The sections from cortex (A, B, C, and D, respectively), thalamus (E, F, G, and H, respectively), cerebellum (I, J, K, and L, respectively) and pons (M, N, O and P, respectively) of WT, Hexa^{-/-}, Neu3^{-/-} and Hexa^{-/-}Neu3^{-/-} mice were stained with anti-CNPase antibody (green; oligodendrocyte marker) and DAPI (blue; nucleus). Quantification of oligodendrocytes in the hippocampus (V), cortex (W), thalamus (X), cerebellum (Y) and pons (Z). Scale bar 50 μ m for cortex and thalamus. Scale bar 100 μ m for cerebellum and pons. The data are represented as the mean \pm SEM. One-way ANOVA was used for statistical analysis

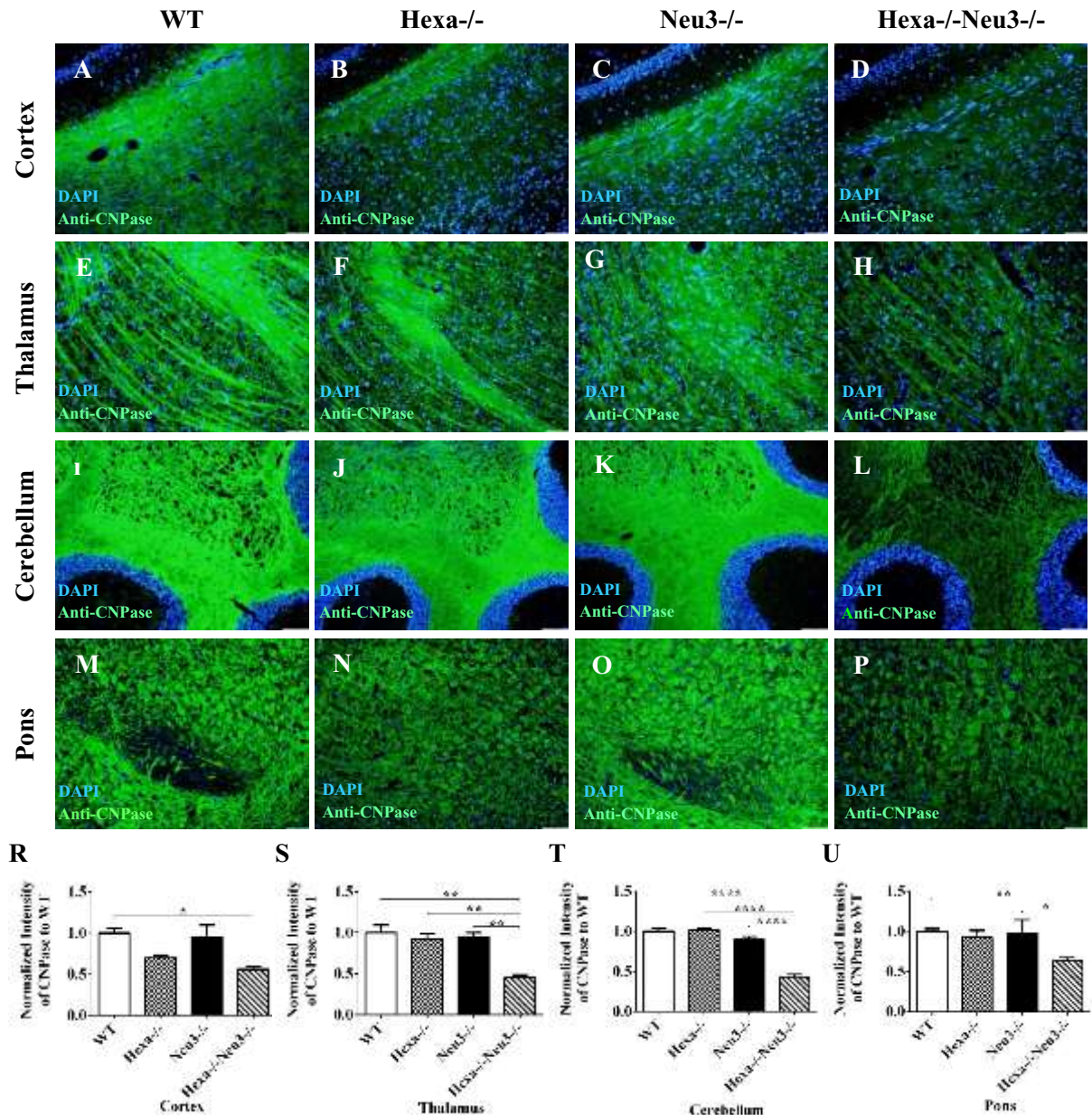


Figure 3.26. Detection of oligodendrocytes number in 4.5-month-old mice. The sections from cortex (A, B, C, and D, respectively), thalamus (E, F, G, and H, respectively), cerebellum (I, J, K, and L, respectively) and pons (M, N, O and P, respectively) of WT, Hexa^{-/-}, Neu3^{-/-} and Hexa^{-/-}Neu3^{-/-} mice were stained with anti-CNPase antibody (green; oligodendrocyte marker) and DAPI (blue; nucleus). Quantification of oligodendrocytes in the hippocampus (V), cortex (W), thalamus (X), cerebellum (Y) and pons (Z). Scale bar 50 μ m for cortex and thalamus. Scale bar 100 μ m for cerebellum and pons. The data are represented as the mean \pm SEM. One-way ANOVA was used for statistical analysis. (* $p < 0.05$, ** $p < 0.025$ and **** $p < 0.001$)

3.10. Behavioral Analysis

3.10.1. Rotarod Test

Rotarod test was used to test used to analyze motor coordination and balance. The time on the rod was detected. The test was done 2.5, 3.5 and 4.5-month-old WT, Hexa^{-/-}, Neu3^{-/-} and Hexa^{-/-}Neu3^{-/-} mice.

There was no observable change in the 2.5-month-old mice (Figure 3.27 A). There was an insignificant decrease in the falling time from the rod in the 3.5-month-old mice (Figure 3.27 B). The most remarkable decrease was detected in 4.5-month-old mice, which was correlated with the amount of stored ganglioside. 4.5-month-old Hexa^{-/-}Neu3^{-/-} mice exhibited a significant decrease in time on rod compared to WT mice as 70% ($p < 0.0001$) and Neu3^{-/-} mice as 61% ($p < 0.0001$) mice (Figure 3.27 C). What is more, 4.5-month-old Hexa^{-/-} mice also displayed a considerably decrease in time on the rod as 45% compared to WT ($p < 0.001$). All in all, motor coordination and balance was significantly decrease while Hexa^{-/-}Neu3^{-/-} mice were aging (Figure 3.27).

3.10.2. Footprint Test

Footprint analysis was used to test the motor coordination and balance of the mice. This analysis evaluated walking pattern (Figure 3.28 A), stride length (Figure 3.28 B), sway length (Figure 3.28 C) and stance length (Figure 3.28 D) of 4.5-month-old WT, Hexa^{-/-}, Neu3^{-/-} and Hexa^{-/-}Neu3^{-/-} mice. When we examined the walking pattern, we observed that Hexa^{-/-}Neu3^{-/-} mice didn't step on separately. Stride length, sway length and stance length significantly decreased as 12% ($p < 0.025$), 36% ($p < 0.0001$) and 20% ($p < 0.0001$) in Hexa^{-/-}Neu3^{-/-} mice compared to age-matched WT mice.

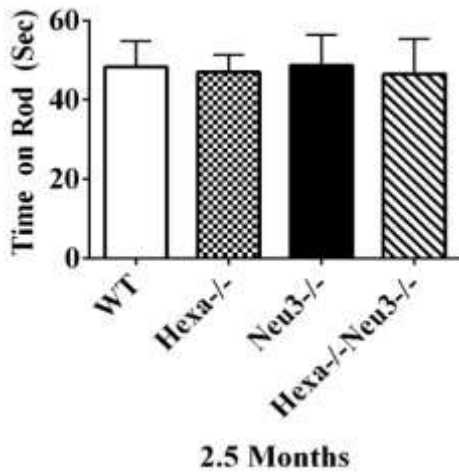
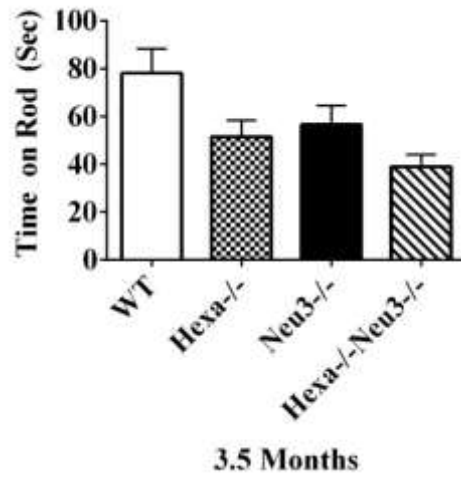
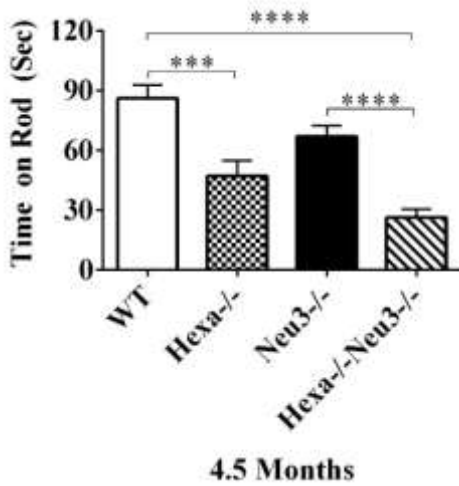
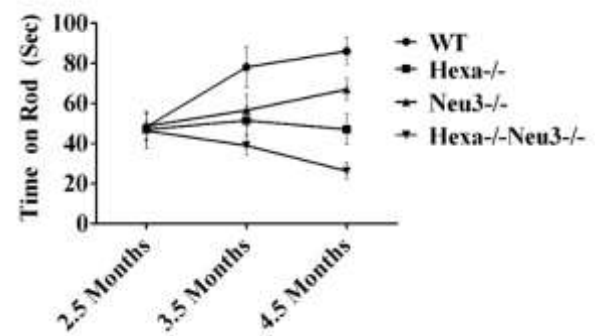
A**B****C****D**

Figure 3.27. Rotarod test of 2.5- (A), 3.5- (B) and 4.5- (C) month-old WT, Hexa^{-/-}, Neu3^{-/-} and Hexa^{-/-}Neu3^{-/-} mice by accelerating speed starting at 4 rpm up to 40 rpm over a 5 min period. Data show mean \pm SEM of measurements. The number of mice was shown in the parenthesis. Significant levels of data were determined using the one-way ANOVA (**p<0.001 and ****p<0.0001)

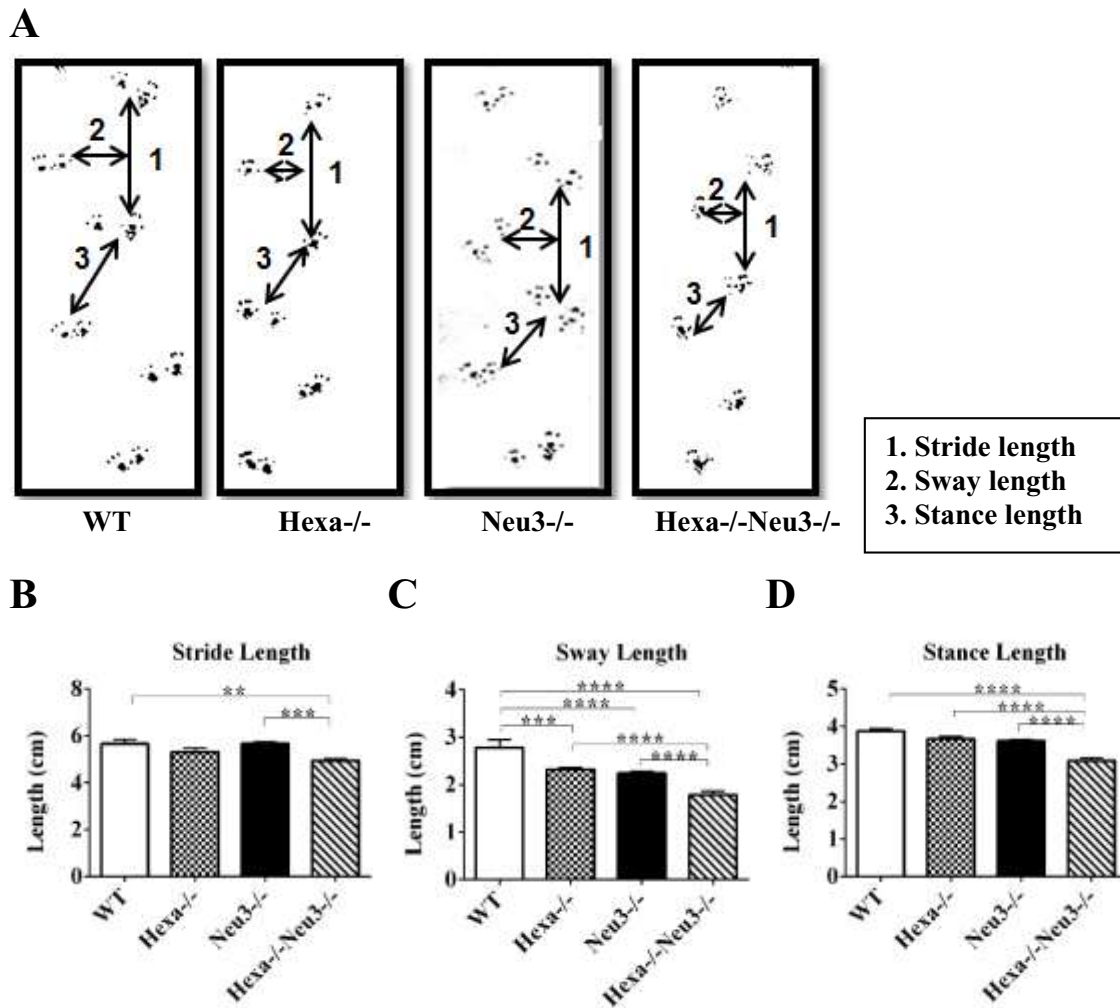


Figure 3.28. Footprints analysis of 4.5-month-old mice. Walking pattern (A), stride length (B), sway length (C) and stance length (D) were evaluated for WT, Hexa^{-/-}, Neu3^{-/-} and Hexa^{-/-}Neu3^{-/-} mice. Histograms represent differences in sway length, stride length, and stance length. Data show mean \pm SEM of measurements. Significant levels of data were determined using the one-way ANOVA (** $p < 0.025$, *** $p < 0.001$ and **** $p < 0.0001$)

3.10.3. Grip Strength Measurement Test

For a more specific measure of muscle strength, grip strength tests were performed (D’Hooge et al. 2005; Foley et al. 2010). When the forelimbs grip strength measurements were performed at the 2.5-month-old mice, a little and insignificant difference was observed in strength between WT, Hexa^{-/-}, Neu3^{-/-} and Hexa^{-/-}Neu3^{-/-} mice (Figure

3.29 A). Compared to WT mice, Hexa^{-/-} and Hexa^{-/-}Neu3^{-/-} mice significantly impaired at 4.5-month-old (87 ± 4.7 in WT, 56.2 ± 6.1 in Hexa^{-/-}, 82 ± 11.2 in Neu3^{-/-} and 26.5 ± 10.5 in Hexa^{-/-}Neu3^{-/-}). The most dramatic impaired one was the Hexa^{-/-}Neu3^{-/-} mice. 4.5-month-old Hexa^{-/-}Neu3^{-/-} mice showed a 70% decrease in muscle strength compared to age-matched WT mice ($p < 0.025$). (Figure 3.29 B). Analysis of Hexa^{-/-}Neu3^{-/-} mice revealed that Hexa^{-/-}Neu3^{-/-} mice had impaired neuromuscular strength and lack of coordinated motor control compared with control groups.

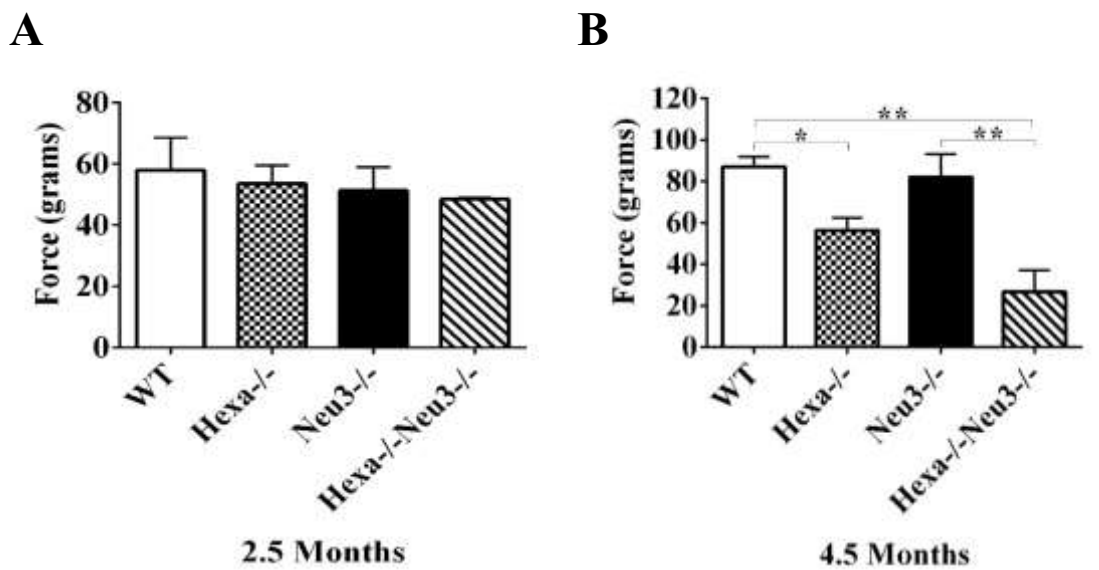


Figure 3.29. Forelimb grip strength of 2.5- (A) and 4.5- (B) month-old mice. Hexa^{-/-}Neu3^{-/-} mice were compared with age-matched WT and single knockouts littermates. The data were presented as the mean \pm SEM. Significant levels of data were determined using the one-way ANOVA (** $p < 0.05$, ** $p < 0.025$)

3.10.4. Passive Avoidance Test

A passive avoidance test was used to test fear-aggravated learning and memory on 2.5 and 4.5-month-old WT, Hexa^{-/-}, Neu3^{-/-} and Hexa^{-/-}Neu3^{-/-} mice. The apparatus has one light and the other dark, separated by a vertical sliding door. The experiment was

carried out in three days. On the first day, the mouse was placed in the light compartment for 30 s. The second day, when the mouse entered the dark compartment, the door was closed and the mouse was given a 0.2 mA electric shock for 2 s. On the third day, the mouse was placed again in the light section with the door opened to allow the mouse to move into the dark section. The latency time for stepping through the door was scored. If there was no damage in the memory of the mice, mice recognize there was an electric shock in the dark compartment and not enter the dark cage.

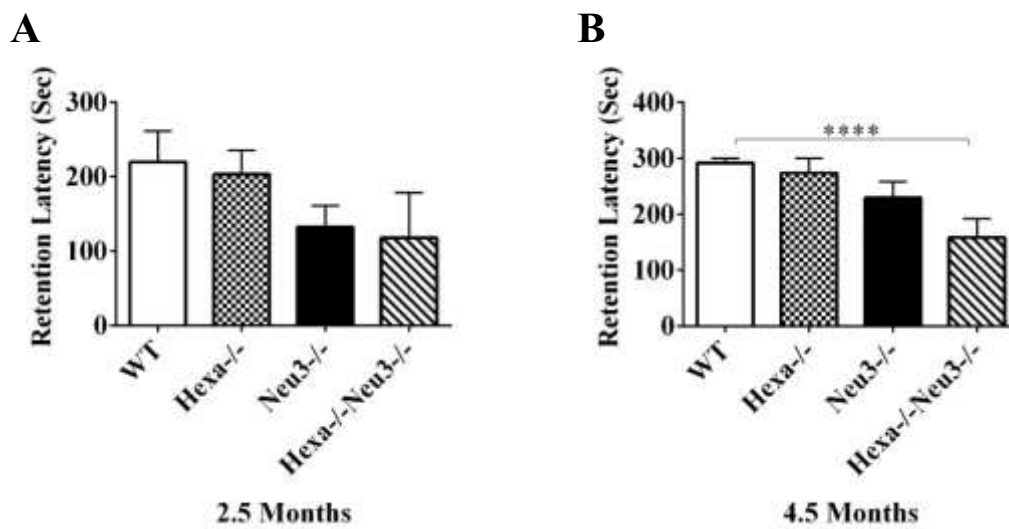


Figure 3.30. Passive avoidance test of 2.5 and 4.5-month-old mice. Hexa^{-/-}Neu3^{-/-} mice were compared with age-matched WT and single knockouts littermates. Latencies to enter the dark compartment on the test day were shown. If mice did not enter the dark compartment within 300 s, the latency time of 300 s was recorded. Data show mean \pm SEM of measurements. Significant levels of data were determined using the one-way ANOVA (****p<0.0001)

Both 2.5-month-old and 4.5-month-old Hexa^{-/-}, Neu3^{-/-} and Hexa^{-/-}Neu3^{-/-} mice memory was effected compared to WT mice (Figure 3.30). After having previously received the electric shock through the feet, 2.5-month-old WT, Hexa^{-/-}, Neu3^{-/-} and Hexa^{-/-}Neu3^{-/-} mice re-entered the dark compartment at the average times: 219 ± 41.3 s, 203 ± 31.8 s, 132 ± 21.8 s, and 118 ± 60 s, respectively. There were no significant changes at the average time. These results may show that the younger age group could

not tolerate light and choose the dark compartment regardless of the 0.2 mA electric shock, for 2 s (Figure 3.30 A).

The significant difference was observed in the memory of 4.5-month-old WT and Hexa^{-/-}Neu3^{-/-} mice. Nearly, all the 4.5-month-old WT mice (292.1 ± 7.9 s) avoided entrance into the dark compartment during the 300 s observation period, whereas the Hexa^{-/-}Neu3^{-/-} mice (19 ± 33.5 s) re-entered the chamber at an average time of ($p < 0.001$). Besides, Hexa^{-/-} and Neu3^{-/-} mice re-entered the chamber in slightly less time than WT mice (Fig. Figure 3.30 B). These results showed that Hexa^{-/-}Neu3^{-/-} mice display a significant deterioration in memory function compared with that in other groups.

3.10.5. Morris Water Maze Test

Morris water maze task was used to detect spatial learning and memory deficits. Both 2.5 and 4.5-month-old Hexa^{-/-}Neu3^{-/-} mice displayed deficits in spatial learning and memory. We used a two-way ANOVA to analyze the data.

WT ($p < 0.001$), Hexa^{-/-} ($p < 0.025$) and Neu3^{-/-} ($p < 0.05$) mice learned to use the visual clues to quickly reach the visible platform in the first 3 days, whereas Hexa^{-/-}Neu3^{-/-} mice took a longer time to swim toward the platform (Figure 3.31 A). All groups initially had difficulty finding the exact location of the hidden platform on day 4. While WT, Hexa^{-/-} and Neu3^{-/-} mice groups quickly improved in their ability to find the platform, both 2.5- and 4.5- month-old Hexa^{-/-}Neu3^{-/-} mice couldn't be able to learn the location of the hidden platform ($p < 0.01$ for 2.5-month-old mice; $p < 0.025$ 4.5-month-old mice). 2.5-month-old WT, Hexa^{-/-} and Neu3^{-/-} mice and 4.5-month-old WT and Neu3^{-/-} mice spent continuously decreased time from day one to five until finding the hidden platform (Figure 3.31 B, D). Latency to target measurements showed that WT, Hexa^{-/-} and Neu3^{-/-} mice used distal clues more efficiently than Hexa^{-/-}Neu3^{-/-} mice (Figure 3.31 A, B).

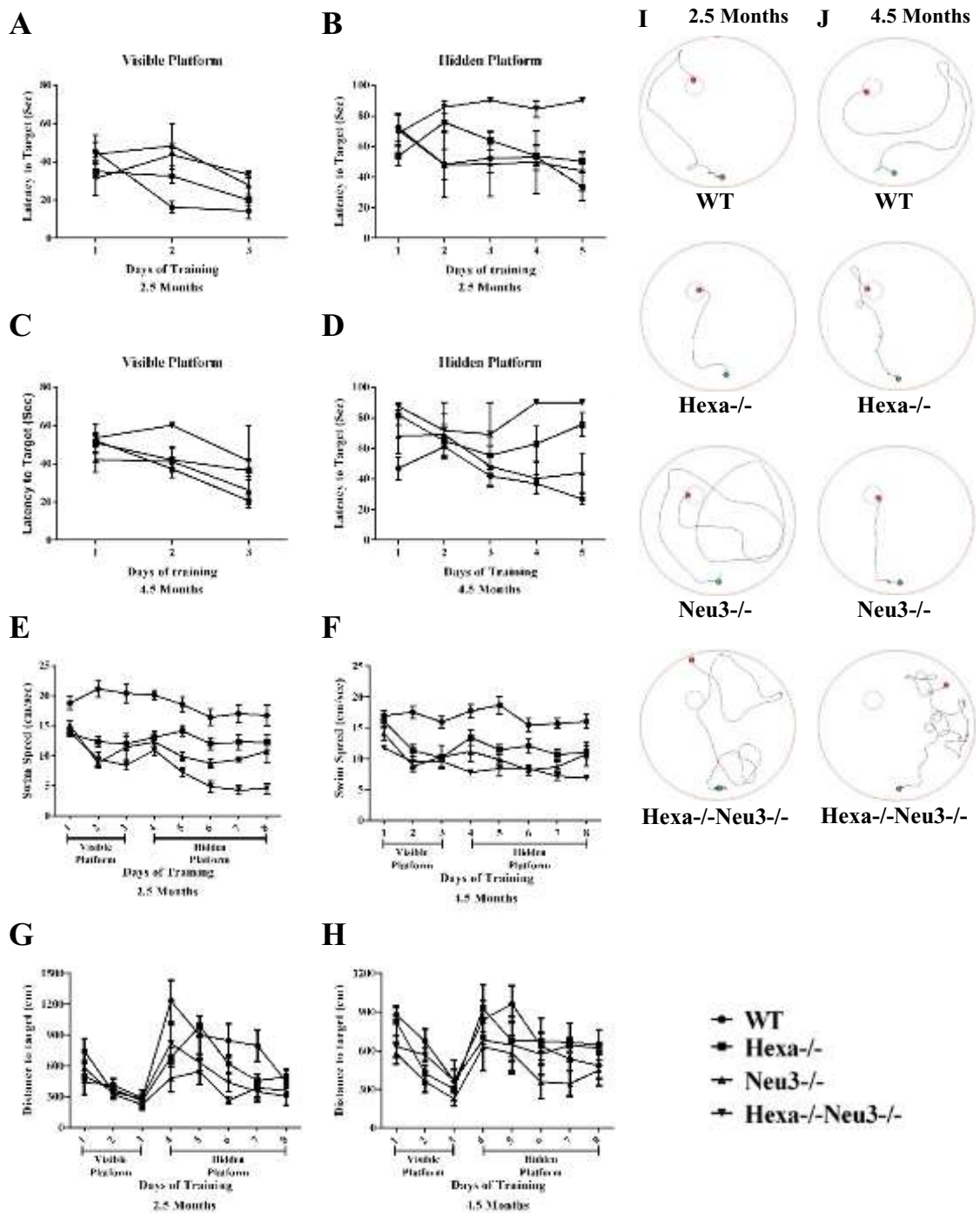


Figure 3.31. Morris water maze test of 2.5- and 4.5-month-old mice. Learning and memory of mice were tested for WT, Hexa^{-/-}, Neu3^{-/-} and Hexa^{-/-}Neu3^{-/-} mice. Latency to the visible platform (A-C, respectively) and hidden platform (B-D, respectively), swim speed (E-F, respectively) and distance to the target (G-H, respectively) were analyzed at 2.5 and 4.5-month-old mice. Typical swim patterns of 2.5 and 4.5-month-old mice on Day 8 were shown (I-J, respectively). Data are presented as means \pm SEM

Swimming speeds recorded in the Morris water maze were significantly lower at 2.5-month-old Hexa^{-/-}Neu3^{-/-} (7.8 ± 0.8) mice compared to age-matched WT (18.6 ± 1.3 , $p < 0.0001$), Hexa^{-/-} (12.7 ± 0.9 , $p < 0.0001$) and Neu3^{-/-} mice (10.8 ± 1.2 , $p < 0.05$) (Figure 3.31 E). The swimming speeds were also significantly lower at 4.5-month-old Hexa^{-/-}Neu3^{-/-} (8.7 ± 0.6) mice compared to age-matched WT (16.8 ± 1 , $p < 0.0001$), Hexa^{-/-} (12 ± 0.9 , $p < 0.001$) and Neu3^{-/-} mice (20.2 ± 1.3 , $p = \text{ns}$) (Figure 3.31 F). However, the average distance spent to find the target platform was similar in WT, Hexa^{-/-}, Neu3^{-/-} and Hexa^{-/-}Neu3^{-/-} mice in both 2.5 and 4.5-month-old mice groups (Figure 3.31 G, H).

Typical swim patterns at the final day of the test revealed that both 2.5 and 4.5-month-old WT, Hexa^{-/-} and Neu3^{-/-} mice used distal clues to find the platform, whereas both 2.5 and 4.5-month-old Hexa^{-/-}Neu3^{-/-} mice couldn't able to find the platform. 4.5-month-old Hexa^{-/-}Neu3^{-/-} mice showed more anxiety-related behaviors compared to the other mice (Figure 3.31 I, J).

3.10.6. Open Field Test

The 5 min open-field test was performed to measure the level of anxiety for 2.5 and 4.5-month-old mice (13). There was a significant difference between the genotype without age, with the main significant effect detected between WT and Hexa^{-/-}Neu3^{-/-} mice. Both 2.5 and 4.5-month-old Hexa^{-/-}Neu3^{-/-} mice showed more anxiety-related behaviors compared to the other genotypes according to the walking patterns (Figure 3.32 C, D) and the amount of time spent in the periphery (Figure 3.32 A) and the center (Figure 3.32 B) of the open field. Hexa^{-/-}Neu3^{-/-} mice spent most of the time in the periphery of the open field. Both 2.5 and 4.5-month-old Hexa^{-/-}Neu3^{-/-} mice showed increased in the spent time in the periphery as 1.2 fold and 1.1 fold, respectively. Additionally, both 2.5 and 4.5-month-old Hexa^{-/-}Neu3^{-/-} mice showed decreased in the spent time in the center as 80% and 65%, respectively.

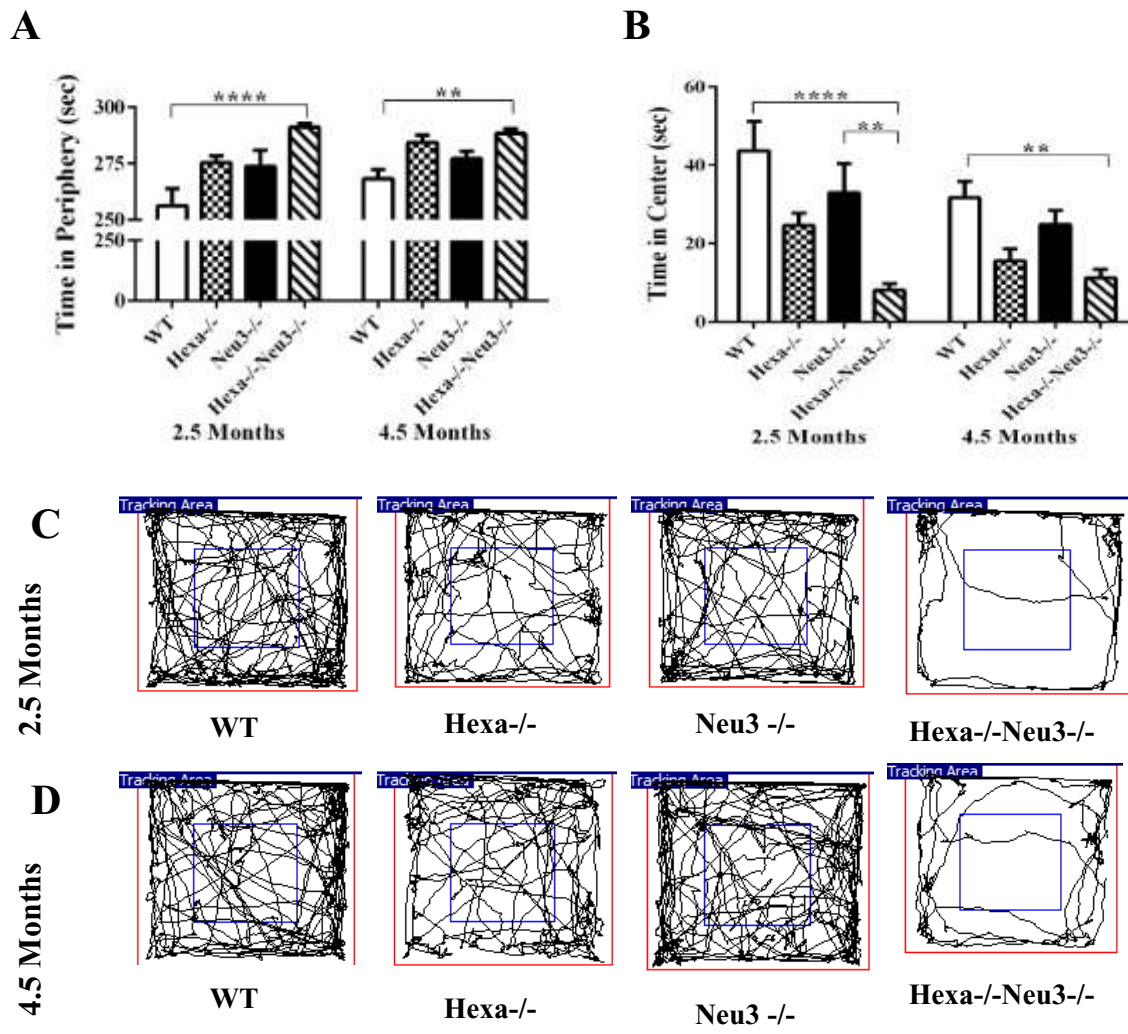


Figure 3.32. Open field test of 2.5- and 4.5-month-old mice. Anxiety was tested for Hexa^{-/-}Neu3^{-/-} mice compared with age-matched WT and single knockouts littermates. Time spent in the periphery (A) and the center (B) of the open field arena in five min were analyzed. The data were presented as the mean \pm SEM. Schematic drawings of the zones and representative traces of 2.5-(C) and 4.5-(D) month-old mouse movement during the test. Two-way ANOVA was used for statistical analysis. (* $p < 0.05$, ** $p < 0.025$, *** $p < 0.01$ and **** $p < 0.001$)

CHAPTER 4

DISCUSSION

Tay-Sachs disease, a fatal neurodegenerative disorder, is resulted from are resulted from impaired degradation of GM2 ganglioside and related substances. Mutations in the HEXA gene lead to the absence of the lysosomal enzyme β -Hexosaminidase A enzyme. Hexa^{-/-} mouse was created with complete absence in the activity of β -Hexosaminidase. However, unlike Tay-Sachs disease patients, there was limited ganglioside storage in certain regions of the nervous system in the Hexa^{-/-} mice (Yamanaka et al. 1994; Cohen-Tannoudji et al. 1995; Phaneuf et al. 1996). It was thought that in these mice there can be a bypass mechanism where accumulated GM2 ganglioside is hydrolyzed using sialidase(s). Sialidase(s) remove sialic acid from GM2 to form the glycolipid GA2 which is further processed by β -Hexosaminidase B to produce LacCer (Phaneuf et al. 1996). To determine if the sialidase NEU3 contributes to GM2 ganglioside degradation, the double deficient mouse model Hexa^{-/-}Neu3^{-/-} was generated first time by crossing Hexa^{-/-} and Neu3^{-/-} mice.

Similar to Tay-Sachs patients, Hexa^{-/-}Neu3^{-/-} mice have growth impairment (Figure 3.2). They are smaller than their littermates throughout their lifespan. This feature is not present in the Hexa^{-/-} mice (Yamanaka et al. 1994; Cohen-Tannoudji et al. 1995; Phaneuf et al. 1996). Furthermore, radiographs revealed abnormalities in the skeletal bones of the Hexa^{-/-}Neu3^{-/-} mice (Figure 3.2 F). Tay-Sachs patients are normal at birth, but the progressive accumulation of GM2 on the neurons leads to muscle weakness, skeletal deformations, ataxia, speech, mental disorders and it results in death maximum 4 years of age (Solovyeva et al. 2018). Similarly, Hexa^{-/-}Neu3^{-/-} mice have a high incidence of sudden death (Figure 3.3) and they live a maximum of 5 months. Therefore, to see the progressive effects of GM2 accumulation we have planned to do our experiments at 2.5- and 4.5-month-old mice.

Hexa^{-/-}Neu3^{-/-} mice were analyzed to see the contribution of sialidase NEU3 to metabolic bypass on the Tay-Sachs mouse model (Hexa^{-/-}). To understand the biological role of sialidase NEU3 on glycolipid metabolism thin-layer chromatography analysis was done on the brain (Figure 3.4 A), testes (Figure 3.5 A), liver (Figure 3.6 A) and kidney (Figure 3.7 A) of the 2.5- and 4.5-month-old Hexa^{-/-}Neu3^{-/-} mice with its age-matched counterparts. It was understood that glycolipid metabolism was effected in Hexa^{-/-}Neu3^{-/-} mice compared to its age-matched counterparts. GM2 and related glycolipids such as GA2 were progressively accumulated in Hexa^{-/-}Neu3^{-/-} mice brain, liver, kidney, and testes.

According to mass spectrometry analysis of LacCer, GM3, GM2, GM1, GA2, GA1 gangliosides, there was a significant increase in the LacCer, GM3, GM2, GA2 level in 4.5-month-old Hexa^{-/-}Neu3^{-/-} mice brain compared to age-matched counterparts (Figure 3.8). GM2 ganglioside level increased 11.86 fold in Hexa^{-/-} mice and 49.40 fold in the Hexa^{-/-}Neu3^{-/-} mice compared to WT mice. GA2 ganglioside level increased 9.59 fold in Hexa^{-/-} mice and 36.61 fold in the Hexa^{-/-}Neu3^{-/-} mice compared to WT mice. The minor accumulation of the GA2 level could result from the activity of other functional sialidases (s) (Neu4 or Neu1) on the GM2 ganglioside. It is also important that lactosylceramide and GM3 were also accumulated in the brains of 4.5-month-old Hexa^{-/-}Neu3^{-/-} mice. This could result from a lack of NEU3, which has a role in GM3 degradation (Valaperta et al. 2006). Thin-layer chromatography and mass spectrometry analysis revealed that sialidase NEU3 is functional on the metabolic bypass of GM2 ganglioside.

The location of enhanced GM2 and lysosomal accumulation was detected in the hippocampus (Figure 3.9), cortex (Figure 3.10), thalamus (Figure 3.11), cerebellum (Figure 3.12), and pons (Figure 3.13) by anti-GM2 and anti-lamp1 staining. It was shown that GM2 was accumulated on lysosomes. There was an increased GM2 amount in the hippocampus, cortex, thalamus, cerebellum, and pons of Hexa^{-/-} and Hexa^{-/-}Neu3^{-/-} mice. The most severe phenotype was observed in the Hexa^{-/-}Neu3^{-/-} mice brain. However, there was no GM2 accumulation on the brain of WT and Neu3^{-/-} mice.

The inclusions of many small vesicles and complex lamellar structures observed in the kidney and testis samples could be the cause of urinary retention and infertility in Hexa^{-/-}Neu3^{-/-} mice (Figure 3.15 E, F).

Enzyme activity of Neuraminidase 1, β -Hexosaminidase B, β -Galactosidase, β -Glucosidase, and α -L-Iduronidase was analyzed in the mouse brain (Figure 3.17). It was observed that the activity of all of the enzymes increased compared to its age-matched counterparts. These could result from the higher accumulation of glycolipids such as LacCer, GM3, GM2, and GA2 in the brain of Hexa^{-/-}Neu3^{-/-} mouse (Figure 3.8). To reduce accumulated glycolipids (LacCer, GM3, GM2, GA2), the enzymatic activity of Neuraminidase 1, β -Hexosaminidase B, β -Galactosidase, β -Glucosidase which have a function on the degradation of gangliosides could increase (Figure 3.17 A).

Hematoxylin–Eosin staining of Hexa^{-/-}Neu3^{-/-} mice brain revealed the presence of remarkable vacuolization in the cortex (Figure 3.18) and Purkinje layer distortion in the cerebellum (Figure 3.19) due to the GM2 accumulation.

Lysosomal storage disorders cause activation of neuroinflammatory responses in the CNS (Bosch and Kielian 2015). Studies on GM1 and GM2 gangliosidosis patients and animal models revealed that ganglioside accumulation results with neuroinflammation (Wada et al. 2000; Jeyakumar et al. 2003; Vitner et al. 2010). The response of astrocytes to injury and inflammation is called astrogliosis (Rasband 2016). In this study, GFAP staining revealed the existence of strong astrogliosis in the hippocampus, cortex, and cerebellum of 2.5- and 4.5- month-old Hexa^{-/-}Neu3^{-/-} mice similar to Tay-Sachs and Sandhoff patient (Figure 3.23 and 3.24, respectively).

Activation of astrocytes produces various pro-inflammatory mediators, chemokines, and cytokines which affect the neurons and oligodendrocytes in the environments (Peferoen et al. 2014). Here, we showed that 4.5-month-old Hexa^{-/-}Neu3^{-/-} mice exhibited a significant loss in neuronal density (Figure 3.22) and oligodendrocytes (Figure 3.26). These results are correlated with TUNEL assay results (Figure 3.20). However, there was no significant change in the number of neuron and oligodendrocyte in the 2.5-month-old mice (Figure 3.21 and 3.23).

According to the gene expression profile studies in the cerebral cortex of normal and GM2 gangliosidosis (Tay-Sachs and Sandhoff) patients, the myelin basic protein gene, expressed by oligodendrocytes was also significantly depressed (Myerowitz et al. 2002). Sialiated gangliosides, especially GD1a and GT1b, are present on the axonal membrane and interact with the MAG on the periaxonal surface of the myelin membrane to promoting myelin sheath stability (Jackman et al. 2009). GM2 is also sialic acid-

containing ganglioside so the accumulation of GM2 could lead to instability of myelin sheath.

Motor coordination and balance were tested on Hexa^{-/-}-Neu3^{-/-} mice with its age-matched counterparts by the Rotarod test (Figure 3.27) and footprint analysis (Figure 3.28). It was realized that the motor coordination and balance system defected in Hexa^{-/-}-Neu3^{-/-} mice. Motor coordination and balance were decreasing while mice were aging. This could result from the affected thalamus and cerebellum. Cerebellum has function on motor control

(Lee et al. 2018). Thalamus has a function in relaying sensory and motor signals from the cerebellum to the cerebral cortex (Medsker et al. 2015).

Hexa^{-/-}-Neu3^{-/-} mice displayed deficits in both spatial and cognitive learning and memory. It was analyzed by a passive avoidance test (Figure 3.30) and Morris water maze (Figure 3.31) and. This might be related to abnormal GM2 accumulation in the CA1, CA2 and CA3 hippocampal region (Figure 3.9) and cortex (Figure 3.10), presence of astrogliosis (Figure 3.23 and 3.24) and loss in significant loss in neuronal density (Figure 3.22) and oligodendrocytes (Figure 3.26). CA1 and CA3 regions make contributions to spatial or temporal processing of memory (Eichenbaum 2017). Purkinje cells are especially responsible for spatial navigation (Lee et al. 2018). There was Purkinje cell depletion in the cerebellum of Hexa^{-/-}-Neu3^{-/-} mice (Figure 3.19). Oligodendrocytes are necessary for myelination and optimal signal transduction in the CNS (Peferoen et al. 2014; Rasband 2016). Consequently, the signal transduction system and memory were seriously affected in the Hexa^{-/-}-Neu3^{-/-} mice.

A passive avoidance test was used to test fear-aggravated learning and memory. It was observed that both 2.5- and 4.5-month-old Hexa^{-/-}, Neu3^{-/-} and Hexa^{-/-}-Neu3^{-/-} mice memory was stimulated compared to WT mice. However, the most affected one was 4.5-month-old Hexa^{-/-}-Neu3^{-/-} mice (Figure 3.30 B). Purkinje cells (PCs) are the only output neurons of the cerebellar cortex and play pivotal roles in coordination, control, and learning of movements (Lee et al. 2018). The results obtained from hematoxylin and eosin staining support the result of behavioral analysis (Figure 3.19).

According to the forelimbs grip strength measurements, there were little and insignificant differences in the strength of the 2.5-month-old mice WT, Hexa^{-/-}, Neu3^{-/-} and Hexa^{-/-}-Neu3^{-/-} mice (Figure 3.29 A). However, the swimming speed of 2.5-month-old Hexa^{-/-}-Neu3^{-/-} mice was lower than the age-matched control group. For that reason,

the decrease in the swimming speed should be related to GM2 accumulation on the cerebellum and pons of Hexa^{-/-}Neu3^{-/-} mice.

The swimming speed was lower in both 2.5- and 4.5-month-old Hexa^{-/-}Neu3^{-/-} mice compared to age-matched control groups (Figure 3.31 E and F), whereas they move equal amounts of distance to find the target platform (Figure 3.31 G and H). For that reason, Hexa^{-/-}Neu3^{-/-} mice couldn't be able to learn the location of the hidden platform related to the impairment in the memory (Figure 3.31 B and D).

The presence of anxiety-related behaviors was determined by the open field test. There was an age-independent significant difference between the genotype. The main significant effect was detected between WT and Hexa^{-/-}Neu3^{-/-} mice. Both 2.5- and 4.5-month-old Hexa^{-/-}Neu3^{-/-} mice showed more anxiety-related behaviors compared to the other genotypes according to the walking patterns and the amount of time spent in the center and the periphery of the open field (Figure 3.32).

All in all, similar to Tay-Sachs patients, the Hexa^{-/-}Neu3^{-/-} mice have growth impairment, progressive neurodegeneration, and neurobehavioral abnormalities. A high incidence of sudden death was also common among the Hexa^{-/-}Neu3^{-/-} mice. In this study, we verified that the combined disruption of the genes encoding Hexa and Neu3 blocked the degradation of gangliosides and resulted in abnormal accumulation of GM2. These results are consistent with the existence of a metabolic bypass pathway in mice as was predicted previously (Phaneuf et al. 1996).

CHAPTER 5

CONCLUSION

Tay-Sachs disease is a severe lysosomal storage disorder. Mutations in the HEXA gene lead to a deficiency in the lysosomal enzyme β -Hexosaminidase A enzyme which converts GM2 to GM3 ganglioside. The progressive GM2 ganglioside accumulation is observed predominantly in the brain of patients. They appear normal in their inborn time, but the accumulation of GM2 in the neurons causes unable to sit alone, eye movement abnormalities, dysphagia, spasms, hypomyelination, and death a maximum of 4 years of age. Hexa^{-/-} mice were created. However, they have a normal lifespan with no obvious neurological deficiency. It was hypothesized that there might be bypass mechanism where stored GM2 ganglioside is degraded to the glycolipid GA2 using sialidase(s), which is further processed by functional β -Hexosaminidase B. In this study, the double deficient mouse model Hexa^{-/-}Neu3^{-/-} was generated the first time to explore the contribution of sialidase NEU3 to metabolic bypass mechanism in the ganglioside degradation pathway. The Hexa^{-/-}Neu3^{-/-} mice were healthy at birth. However, progressive GM2 accumulation resulted in a progressive loss in the weight and they lived a maximum of 5 months of age. In contrast to the mild disease phenotype of the Hexa^{-/-} mouse model (Yamanaka et al. 1994; Cohen-Tannoudji et al. 1995; Phaneuf et al. 1996), the Hexa^{-/-}Neu3^{-/-} mice demonstrated a lethal early-onset phenotype similar to Tay-Sachs patients.

Thin-layer chromatography and mass spectrometric analysis demonstrated that there was a huge age depended on GM2 accumulation in the brain. The undegraded GM2 on the lysosomes was detected widespread brain regions including the hippocampus, cortex, thalamus, cerebellum, and pons. The progressive GM2 accumulation was also verified on testes, liver, and kidney of Hexa^{-/-}Neu3^{-/-} mice. These results were supported by the presence of membranous cytoplasmic bodies in the lysosome of the Purkinje cells, granular cell, cerebral neuron, kidney, and testis similar to those reported in human Tay-Sachs patients

The Hexa^{-/-}Neu3^{-/-} mice exhibited progressive neurodegeneration. GM2 accumulation resulted in cytoplasmic vacuolization in the neuronal cell, Purkinje cell depletion in the cerebellum and axonal degenerations. Neuroinflammation was also triggered by a signaling cascade that activates astrocytes, which cause to the age-dependent loss in oligodendrocytes and neurons in Hexa^{-/-}Neu3^{-/-} mice.

Radiographs revealed the skeletal bone abnormalities were present in Hexa^{-/-}Neu3^{-/-} mice. Growth impairment, slow movement, tremors, anxiety and age-dependent weakening in memory and neuromuscular strength were the detectable neurological abnormalities observed in these mice.

Hexa^{-/-}Neu3^{-/-} mice showed enormous GM2 accumulation, clinical (Table 5.1), pathological, and biochemical abnormalities similar to Tay-Sachs patients.

Table 5.1. Clinical symptoms in Tay-Sachs patients, Hexa^{-/-} mouse Hexa^{-/-}Neu3^{-/-} mouse. (Source: Solovyeva et al. 2018; Yamanaka et al. 1994)

Organism	Tay-Sachs patients	Hexa^{-/-} mouse	Hexa^{-/-}Neu3^{-/-} mouse
Symptoms	<ul style="list-style-type: none"> • Healthy at birth • Motor weakness • Epileptic crisis • Slow body growth • Muscle weakness • Delayed mental and social skills • Feeding difficulties • Mental and motor deterioration • A fatal outcome by age 2-4 years 	<ul style="list-style-type: none"> • Healthy • No apparent motor or behavioral disorders 	<ul style="list-style-type: none"> • Healthy at birth • Progressive loss in the weight • Feeding difficulties • Skeletal bone abnormalities • Growth impairment • Slow movement • Tremors • Anxiety • Lived maximum of 5 months of age

Tay-Sachs is a rare childhood disease and a limited number of brain autopsy samples are available. Therefore, the onset and age-dependent morphological changes in the central nervous system are mainly unknown. The similarity of the Hexa^{-/-}Neu3^{-/-}

mouse model to Tay-Sachs patients provides an enormous possibility to explore the pathogenesis and the progressive events resulted from lysosomal dysfunction and neurodegeneration. The evaluation of molecular therapeutic effects on the central nervous system would be easily manageable. Various therapeutic options including substrate deprivation and gene therapy could be investigated with this model.

All of these results showed us, deficiency of sialidase Neu3 in mouse blocks the biological bypass in the Hexa^{-/-} mouse. Therefore, sialidase Neu3 would have the therapeutic potential for Tay-Sachs patients. Therefore, overexpression of human sialidase Neu3 in the Tay-Sachs patient's fibroblast or neuroglia cells may restore the disease phenotype (GM2 accumulation). The therapeutic potential of human sialidase Neu3 would be investigated in the Hexa^{-/-}Neu3^{-/-} mice by generating transgenic mice which is a double knockout for both Hexa and Neu3 gene and overexpress human sialidase Neu3.

Different therapeutic options could be tested by targeting sialidase Neu3. For example, specific drugs could be designed to increase the level of sialidase Neu3 in Tay-Sachs patients to cure the disease phenotype. Then, the Crispr-Cas9 gene-editing approach could be used to target the promoter region of hNeu3 and overexpress it in the patient. Finally, specific drugs could be designed to increase the functionality of human sialidase Neu3 towards to GM2.

All in all, Hexa^{-/-}Neu3^{-/-} mice were generated the first time to explore the contribution of sialidase NEU3 to the metabolic bypass mechanism in the ganglioside degradation pathway. Our results indicated that Hexa^{-/-}Neu3^{-/-} mice could be a suitable model for early-onset Tay-Sachs disease.

REFERENCES

- Baudry M, Yao Y, Simmons D, Liu J, Bi X. 2003. Postnatal development of inflammation in a murine model of Niemann–Pick type C disease: immunohistochemical observations of microglia and astroglia. *Exp Neurol*. 184(2):887–903.
- Bosch ME, Kielian T. 2015. Neuroinflammatory paradigms in lysosomal storage diseases. *Front Neurosci*. 9(OCT):1–11.
- Calhan OY, Seyrantepe V. 2017. Mice with Catalytically Inactive Cathepsin A Display Neurobehavioral Alterations. *Behav Neurol*. 2017(January):1–11.
- Cohen-Tannoudji M, Marchand P, Akli S, Sheardown SA, Puech JP, Kress C, Gressens P, Nassogne MC, Beccari T, Muggleton-Harris AL, et al. 1995. Disruption of murine Hexa gene leads to enzymatic deficiency and to neuronal lysosomal storage, similar to that observed in Tay-Sachs disease. *Mamm Genome*. 6(12):844–849.
- D’Azzo A, Tessitore A, Sano R. 2006. Gangliosides as apoptotic signals in ER stress response. *Cell Death Differ*. 13(3):404–14.
- D’Hooge R, Lüllmann-Rauch R, Beckers T, Balschun D, Schwake M, Reiss K, Figura K von, Saftig P. 2005. Neurocognitive and Psychotiform Behavioral Alterations and Enhanced Hippocampal Long-Term Potentiation in Transgenic Mice Displaying Neuropathological Features of Human α -Mannosidosis. *J Neurosci*. 25(28):6539–6549.
- Eichenbaum H. 2017. On the Integration of Space, Time, and Memory. *Neuron*. 95(5):1007–1018.
- Fanzani A, Colombo F, Giuliani R, Preti A, Marchesini S. 2004. Cytosolic sialidase Neu2 upregulation during PC12 cells differentiation. *FEBS Lett*. 566(1–3):178–82.
- Farfel-Becker T, Vitner EB, Pressey SNR, Eilam R, Cooper JD, Futerman AH. 2011. Spatial and temporal correlation between neuron loss and neuroinflammation in a mouse model of neuronopathic Gaucher disease. *Hum Mol Genet*. 20(7):1375–1386.

Ferreira CR, Gahl WA. 2017. Lysosomal storage diseases. *Transl Sci Rare Dis.* 2(1–2):1–71.

Foley JW, Bercury SD, Finn P, Cheng SH, Scheule RK, Ziegler RJ. 2010. Evaluation of systemic follistatin as an adjuvant to stimulate muscle repair and improve motor function in Pompe mice. *Mol Ther.* 18(9):1584–1591.

Fu H, Cataldi MP, Ware TA, Zaraspe K, Meadows AS, Murrey DA, McCarty DM. 2016. Functional correction of neurological and somatic disorders at later stages of disease in MPS IIIA mice by systemic scAAV9-hSGSH gene delivery. *Mol Ther - Methods Clin Dev.* 3(October 2015):16036.

Gómez-Grau M, Albaigès J, Casas J, Auladell C, Dierssen M, Vilageliu L, Grinberg D. 2017. New murine Niemann-Pick type C models bearing a pseudoexon-generating mutation recapitulate the main neurobehavioural and molecular features of the disease. *Sci Rep.* 7(1):41931.

Gulinello M, Chen F, Dobrenis K. 2008. Early deficits in motor coordination and cognitive dysfunction in a mouse model of the neurodegenerative lysosomal storage disorder, Sandhoff disease. *Behav Brain Res.* 193(2):315–319.

Hasegawa T, Yamaguchi K, Wada T, Takeda A, Itoyama Y, Miyagi T. 2000. Molecular cloning of mouse ganglioside sialidase and its increased expression in Neuro2a cell differentiation. *J Biol Chem.* 275(11):8007–8015.

Hayase T, Shimizu J, Goto T, Nozaki Y, Mori M, Takahashi N, Namba E, Yamagata T, Momoi MY. 2010. Unilaterally and rapidly progressing white matter lesion and elevated cytokines in a patient with Tay – Sachs disease. *Brain Dev.* 32(3):244–247.

Heldermon CD, Ohlemiller KK, Herzog ED, Vogler C, Qin E, Wozniak DF, Tan Y, Orrock JL, Sands MS. 2010. Therapeutic Efficacy of Bone Marrow Transplant, Intracranial AAV-mediated Gene Therapy, or Both in the Mouse Model of MPS IIIB. *Mol Ther.* 18(5):873–880.

Hofmann L, Karl F, Sommer C, Üçeyler N. 2017. Affective and cognitive behavior in the alpha-galactosidase A deficient mouse model of Fabry disease. *PLoS One.* 12(6):1–14.

Huang J, Trasler JM, Igdoura S, Michaud J, Hanai N, Gravel RA. 1997. Apoptotic cell death in mouse models of G M2 gangliosidosis and observations on human Tay – Sachs

and Sandhoff diseases. *Hum Mol Genet.* 6(11):1879–1885.

Huynh KK, Eskelinen E, Scott CC, Malevanets A, Saftig P, Grinstein S. 2007. LAMP proteins are required for fusion of lysosomes with phagosomes. *EMBO J.* 26(2):313–324.

Jackman N, Ishii A, Bansal R. 2009. Myelin biogenesis and oligodendrocyte development: parsing out the role of glycosphingolipids. *Physiol.*(860):290–297.

Jeyakumar M, Thomas R, Elliot-Smith E, Smitf DA, van der Spoel AC, D’Azzo A, Perry VH, Butters TD, Dwek RA, Platt FM. 2003. Central nervous system inflammation is a hallmark of pathogenesis in mouse models of GM1 and GM2 gangliosidosis. *Brain.* 126(4):974–987.

Kollmann K, Uusi-Rauva K, Scifo E, Tyynelä J, Jalanko A, Braulke T. 2013. Cell biology and function of neuronal ceroid lipofuscinosis-related proteins. *Biochim Biophys Acta - Mol Basis Dis.* 1832(11):1866–1881.

Kolter T. 2012. *Ganglioside Biochemistry.* ISRN Biochem. 2012:1–36.

Kreutz F, Petry S, Camassola M, Schein V, Guma FCR, Beyer N, Maria V, Trindade T. 2013. Alterations of membrane lipids and in gene expression of ganglioside metabolism in different brain structures in a mouse model of mucopolysaccharidosis type I (MPS I). *Gene.* 527(1):109–114.

Lawson C, Martin D. 2016. Animal models of GM2 gangliosidosis: utility and limitations. *Appl Clin Genet.* Volume 9:111–120.

Lee J-M, Kim C, Park J-M, Song M, Kim Y-J. 2018. Effect of treadmill exercise on spatial navigation impairment associated with cerebellar Purkinje cell loss following chronic cerebral hypoperfusion. *Mol Med Rep.* 17:8121–8128.

Lee S, Hwang E, Lee D, Choi JH. 2017. Pulse-train Stimulation of Primary Somatosensory Cortex Blocks Pain Perception in Tail Clip Test. *Exp Neurobiol.* 26(2):90–96.

Li S-C, Li Y-T, Moriya S, Miyagi T. 2001. Degradation of G(M1) and G(M2) by mammalian sialidases. *Biochem J.* 360:233–237. doi:10.1042/0264-6021:3600233.
Medsker B, Forno E, Simhan H, Juan C, Sciences R. 2015. Thalamic structures and

associated cognitive functions: Relations with age and aging Rosemary. *Neurosci Biobehav Rev.* 54:29–37.

Monti E, Bonten E, D’Azzo A, Bresciani R, Venerando B, Borsani G, Schauer R, Tettamanti G. 2010. Sialidases in vertebrates: a family of enzymes tailored for several cell functions. *Adv Carbohydr Chem Biochem.* 64(Volume 64):403–79.

Monti E, Preti A, Venerando B, Borsani G. 2002. Recent development in mammalian sialidase molecular biology. *Neurochem Res.* 27(7–8):649–63.

Morales I, Guzmán-Martínez L, Cerda-Troncoso C, Farías GA, Maccioni RB. 2014. Neuroinflammation in the pathogenesis of Alzheimer’s disease. A rational framework for the search of novel therapeutic approaches. *Front Cell Neurosci.* 8(1 APR).

Myerowitz R, Lawson D, Mizukami H, Mi Y, Tiff CJ, Proia RL. 2002. Molecular pathophysiology in Tay-Sachs and Sandhoff diseases as revealed by gene expression profiling. *Hum Mol Genet.* 11(11):1343–1351.

Nampoothiri SS, Potluri T, Subramanian H, Krishnamurthy RG. 2017. Rodent Gymnastics: Neurobehavioral Assays in Ischemic Stroke. *Mol Neurobiol.* 54(9):6750–6761.

Palmano K, Rowan A, Guillermo R, Guan J, McJarrow P. 2015. The Role of Gangliosides in Neurodevelopment. *Nutrients.* 7(5):3891–3913.

Papini N, Anastasia L, Tringali C, Croci G, Bresciani R, Yamaguchi K, Miyagi T, Preti A, Prinetti A, Prioni S, et al. 2004. The Plasma Membrane-associated Sialidase MmNEU3 Modifies the Ganglioside Pattern of Adjacent Cells Supporting Its Involvement in Cell-to-Cell Interactions. *J Biol Chem.* 279(17):16989–16995.

Peferoen L, Kipp M, van der Valk P, van Noort JM, Amor S. 2014. Oligodendrocyte-microglia cross-talk in the central nervous system. *Immunology.* 141(3):302–313.
Phaneuf D, Wakamatsu N, Huang J, Borowski A, Peterson AC, Fortunato SR, Ritter G, Igdoura SA, Morales CR, Benoit G, et al. 1996. Dramatically different phenotypes in mouse models of human Tay-Sachs and Sandhoff diseases. *Hum Mol Genet.* 5(1):1–14.

Posse de Chaves E, Sipione S. 2010. Sphingolipids and gangliosides of the nervous system in membrane function and dysfunction. *FEBS Lett.* 584(9):1748–1759.

Rasband MN. 2016. Glial Contributions to Neural Function and Disease. *Mol Cell Proteomics*. 15(2):355–361.

Reichel CA, Rehberg M, Lerchenberger M, Berberich N, Bihari P, Khandoga AG, Zahler S, Krombach F. 2009. Ccl2 and Ccl3 mediate neutrophil recruitment via induction of protein synthesis and generation of lipid mediators. *Arterioscler Thromb Vasc Biol*. 29(11):1787–1793.

Ridet JL, Malhotra SK, Privat a, Gage FH. 1997. Reactive astrocytes: cellular and molecular cues to biological function [published erratum appears in *Trends Neurosci* 1998 Feb;21(2):80]. *Trends Neurosci*. 20(1988):570–577.

Rubin RD, Watson PD, Duff MC, Cohen NJ. 2014. The role of the hippocampus in flexible cognition and social behavior. *Front Hum Neurosci*. 8(September):1–15.

Sandhoff K. 2016. Neuronal sphingolipidoses: Membrane lipids and sphingolipid activator proteins regulate lysosomal sphingolipid catabolism. *Biochimie*. 130:146–151.

Sandhoff K, Harzer K. 2013. Gangliosides and Gangliosidoses: Principles of Molecular and Metabolic Pathogenesis. *J Neurosci*. 33(25):10195–10208.

Sandhoff K, Kolter T. 1998. Processing of sphingolipid activator proteins and topology of lysosomal digestion. *Acta Biochim Pol*. 45(2):373–384.

Sandhoff R, Hepbildikler ST, Jennemann R, Geyer R, Gieselmann V, Proia RL, Wiegandt H, Gröne H-J. 2002. Kidney Sulfatides in Mouse Models of Inherited Glycosphingolipid Disorders. *J Biol Chem*. 277(23):20386–20398.

Sango K, Yamanaka S, Hoffmann A, Okuda Y, Grinberg A, Westphal H, McDonald MP, Crawley JN, Sandhoff K, Suzuki K, et al. 1995. Mouse models of Tay–Sachs and Sandhoff diseases differ in neurologic phenotype and ganglioside metabolism. *Nat Genet*. 11(2):170–176.

Schlegel V, Thieme M, Holzmann C, Witt M, Grittner U, Rolfs A, Wree A. 2016. Pharmacologic treatment assigned for Niemann Pick Type C1 disease partly changes behavioral traits in wild-type mice. *Int J Mol Sci*. 17(11):1–17.

Seibenhener ML, Wooten MC. 2015. Use of the Open Field Maze to Measure Locomotor and Anxiety-like Behavior in Mice. *J Vis Exp*.(96):1–6.

Seyrantepe V, Canuel M, Carpentier S, Landry K, Durand S, Liang F, Zeng J, Caqueret A, Gravel RA, Marchesini S, et al. 2008. Mice deficient in Neu4 sialidase exhibit abnormal ganglioside catabolism and lysosomal storage. *Hum Mol Genet.* 17(11):1556–1568.

Seyrantepe V, Iannello A, Liang F, Kanshin E, Jayanth P, Samarani S, Szewczuk MR, Ahmad A, Pshezhetsky A V. 2010. Regulation of phagocytosis in macrophages by neuraminidase 1. *J Biol Chem.* 285(1):206–215.

Seyrantepe V, Landry K, Trudel S, Hassan JA, Morales CR, Pshezhetsky A V. 2004. Neu4, a novel human lysosomal lumen sialidase, confers normal phenotype to sialidosis and galactosialidosis cells. *J Biol Chem.* 279(35):37021–37029.

Seyrantepe V, Lema P, Caqueret A, Dridi L, Hadj SB, Boucher F, Levade T, Carmant L, Gravel RA, Hamel E, et al. 2010. Mice Doubly-Deficient in Lysosomal Hexosaminidase A and Neuraminidase 4 Show Epileptic Crises and Rapid Neuronal Loss. *PLoS Genet.* 6(9): e1001118.

Shiotsuki H, Yoshimi K, Shimo Y, Funayama M, Takamatsu Y, Ikeda K, Takahashi R, Kitazawa S, Hattori N. 2010. A rotarod test for evaluation of motor skill learning. *J Neurosci Methods.* 189(2):180–185.

Sidman RL, Taksir T, Fidler J, Zhao M, Dodge JC, Passini MA, Raben N, Thurberg BL, Cheng SH, Shihabuddin LS. 2008. Temporal Neuropathologic and Behavioral Phenotype of 6 neo /6 neo Pompe Disease Mice. *J Neuropathol Exp Neurol.* 67(8):803–818.

Solovyeva V V, Shaimardanova AA, Chulpanova DS, Kitaeva K V, Chakrabarti L, Rizvanov AA. 2018. New Approaches to Tay-Sachs Disease Therapy. *Front Physiol.* 9(November):1–11.

Sun A. 2018. Lysosomal storage disease overview. *Ann Transl Med.* 6(24):476.-476.

Tamura S, Tamura Y, Uchida K, Nibe K, Nakaichi M, Hossain MA, Chang HS, Rahman MM, Yabuki A, Yamato O. 2010. GM2 Gangliosidosis variant 0 (Sandhoff-like disease) in a family of toy poodles. *J Vet Intern Med.* 24(5):1013–1019.

Tardy C, Andrieu-abadie N, Salvayre R, Levade T. 2004. Lysosomal Storage Diseases :

Is Impaired Apoptosis a Pathogenic Mechanism ? *Neurochemical research*. 29(5):871–880.

Timur ZK, Akyildiz Demir S, Marsching C, Sandhoff R, Seyrantepe V. 2015. Neuraminidase-1 contributes significantly to the degradation of neuronal B-series gangliosides but not to the bypass of the catabolic block in Tay–Sachs mouse models. *Mol Genet Metab Reports*. 4:72–82.

Utz JRJ, Crutcher T, Schneider J, Sorgen P, Whitley CB. 2015. Biomarkers of central nervous system inflammation in infantile and juvenile gangliosidoses. *Mol Genet Metab*. 114(2):274–280.

Valaperta R, Chigorno V, Basso L, Prinetti A, Bresciani R, Preti A, Miyagi T, Sonnino S. 2006. Plasma membrane production of ceramide from ganglioside GM3 in human fibroblasts. *FASEB J*. 20(8):1227–1229.

Vermehren-Schmaedick A, Jenkins VK, Knopp SJ, Balkowiec A, Bissonnette JM. 2012. Acute intermittent hypoxia-induced expression of brain-derived neurotrophic factor is disrupted in the brainstem of methyl-CpG-binding protein 2 null mice. *Neuroscience*. 206:1–6.

Vitner EB, Platt FM, Futerman AH. 2010. Common and uncommon pathogenic cascades in lysosomal storage diseases. *J Biol Chem*. 285(27):20423–7.

Wada R, Tiffit CJ, Proia RL. 2000. Microglial activation precedes acute neurodegeneration in Sandhoff disease and is suppressed by bone marrow transplantation. *PNAS*. 97(20):10954–10959.

Wei H, Kim S-J, Zhang Z, Tsai P-C, Wisniewski KE, Mukherjee AB. 2008. ER and oxidative stresses are common mediators of apoptosis in both neurodegenerative and non-neurodegenerative lysosomal storage disorders and are alleviated by chemical chaperones. *Hum Mol Genet*. 17(4):469–77.

Wible C. 2013. Hippocampal Physiology, Structure and Function and the Neuroscience of Schizophrenia: A Unified Account of Declarative Memory Deficits, Working Memory Deficits and Schizophrenic Symptoms. *Behav Sci (Basel)*. 3(2):298–315.

Wilkinson FL, Holley RJ, Langford-Smith KJ, Badrinath S, Liao A, Langford-Smith A, Cooper JD, Jones SA, Wraith JE, Wynn RF, et al. 2012. Neuropathology in mouse models of mucopolysaccharidosis type I, IIIA and IIIB. *PLoS One*. 7(4): e35787.

Xu Y, Barnes S, Sun Y, Grabowski GA. 2010. Multi-system disorders of

glycosphingolipid and ganglioside metabolism. *J Lipid Res.* 51(7):1643–1675.

Yamaguchi K, Shiozaki K, Moriya S, Koseki K, Wada T, Tateno H, Sato I, Asano M, Iwakura Y, Miyagi T. 2012. Reduced susceptibility to colitis-associated colon carcinogenesis in mice lacking plasma membrane-associated sialidase. *PLoS One.* 7(7): e41132.

Yamanaka S, Johnson MD, Grinberg A, Westphal H, Crawley JN, Taniike M, Suzuki K, Proia RL. 1994. Targeted disruption of the Hexa gene results in mice with biochemical and pathologic features of Tay-Sachs disease. *Proc Natl Acad Sci U S A.* 91:9975–9979.

Yamawaki N, Radulovic J, Shepherd GMG. 2016. A Corticocortical Circuit Directly Links Retrosplenial Cortex to M2 in the Mouse. *J Neurosci.* 36(36):9365–9374.

Yu RK, Ledeen RW. 1972. Gangliosides of human, bovine and rabbit plasma. *J Lipid Res.* 13:680–686.

Zanchetti G, Colombi P, Manzoni M, Anastasia L, Caimi L, Borsani G, Venerando B, Tettamanti G, Preti A, Monti E, et al. 2007. Sialidase NEU3 is a peripheral membrane protein localized on the cell surface and in endosomal structures. *Biochem J.* 408(2):211–219.

Zhang J-M, An J. 2007. Cytokines, Inflammation, and Pain. *Int Anesthesiol Clin.* 45(2):27–37.

VITA
SEÇİL AKYILDIZ DEMİR

Date and Place of Birth: 1988 İzmir

E-mail: secilakyildiz@gmail.com / secilakyildiz@iyte.edu.tr

Education

Ph.D. Molecular Biology and Genetics, 2014-2020, Izmir Institute of Technology, Molecular Biology and Genetics Department, Izmir, Turkey

MSc. Molecular Biology and Genetics, 20011-2014, Izmir Institute of Technology, Molecular Biology and Genetics Department, Izmir, Turkey

BSc. Molecular Biology and Genetics, 2006-2011, Izmir Institute of Technology, Molecular Biology and Genetics Department, Izmir, Turkey

Teaching and Professional Experience

Research assistant, 2012-2019, Izmir Institute of Technology, Molecular Biology and Genetics Department, Izmir, Turkey

Publications

Secil Akyildiz Demir, Volkan Seyrantepe, “Identification of cytoplasmic sialidase Neu2-associated proteins by LC-MS/MS”, Turkish Journal of Biochemistry, 2018 June 19

Melis Kose, Secil Akyildiz Demir, Gulcin Akinci, Cenk Eraslan, Unsal Yilmaz, Serdar Ceylaner, Eser Sozmen Yildirim, Volkan Seyrantepe “The Second Case of Saposin A Deficiency and Altered Autophagy”, JIMD Rep., 2018.

Volkan Seyrantepe, Secil Akyildiz Demir, Zehra Kevser Timur, Johanna Von Gerichten, Christian Marsching, Esra Erdemli, Emin Oztas, Kohta Takahashi, Kazunori Yamaguchi, Nurselin Ates, Buket Dönmez Demir, Turgay Dalkara, Katrin Erich, Carsten Hopf, Roger Sandhoff, Taeko Miyagi, “Murine Sialidase Neu3 facilitates GM2 degradation and bypass in mouse model of Tay-Sachs disease”, Experimental Neurology. 2017

Zehra Kevser Timur, Secil Akyildiz Demir, Volkan Seyrantepe, “Lysosomal Cathepsin A Plays a Significant Role in the Processing of Endogenous Bioactive Peptides”, Front Mol Biosci. 2016

Nisa Gul Amuk, Gökmen Kurt, Yusuf Baran, Volkan Seyrantepe, Melis Kartal Yandim, Aysun Adan, Secil Akyildiz Demir, Yagmur Kiraz, Mehmet Fatih Sonmez, “Effects of cell-mediated osteoprotegerin gene transfer and mesenchymal stem cell applications on orthodontically induced root resorption of rat teeth”. Eur J Orthod. 2016

Zehra Kevser Timur, Seçil Akyildiz Demir, Christian Marsching, Roger Sandhoff, Volkan Seyrantepe, “Neuraminidase-1 contributes significantly to the degradation of neuronal B-series gangliosides but not to the bypass of the catabolic block in Tay–Sachs mouse models”, Molecular Genetics and Metabolism Reports 2015